UC San Diego

UC San Diego Electronic Theses and Dissertations

Title

Domain organization and conformational dynamics of a p90RSK2:ERK2 complex

Permalink

https://escholarship.org/uc/item/36v3j650

Author

Nguyen, Hoang Phuong My

Publication Date

2025

Peer reviewed|Thesis/dissertation

eScholarship.org Powered by the California Digital Library
University of California

UNIVERSITY OF CALIFORNIA SAN DIEGO

Domain organization and conformational dynamics of a p90RSK2:ERK2 complex

A Dissertation submitted in partial satisfaction of the requirements
for the degree Doctor of Philosophy

in

Chemistry

by

Hoang Phuong My Nguyen

Committee in charge:

Professor Susan Taylor, Chair
Professor Mark Anthony Herzik Jr, Co-Chair
Professor Michael Gilson
Professor Thomas Hermann
Professor Judy Kim
Professor Elizabeth Komives

2025

Copyright

Hoang Phuong My Nguyen, 2025

All rights reserved.

The Dissertation of Hoang Phuong My Nguyen is approved, and it is acceptable in quality and form for publication on microfilm and electronically.

University of California San Diego

2025

DEDICATION

To my parents, who taught me the value of hard work and education.
To my mentors, who inspired in me a love for science.
To my friends, who stood by me through the ups and downs.
And to myself, for never giving up.

TABLE OF CONTENTS

DISSERTATION APPROVAL PAGE ii

DEDICATION v

TABLE OF CONTENTS vi

LIST OF FIGURES viii

LIST OF ABBREVIATIONS x

ACKNOWLEDGEMENTS xiv

VITA xviii

PUBLICATIONS xviii

FIELD OF STUDY xviii

HONORS AND AWARDS xix

ABSTRACT OF THE DISSERTATION xx

Chapter I Introduction 1

A. Core motifs and conserved structural elements of protein kinases. 2

B. RSK biology and important motif and activation mechanism 7

C. Introduction to Cryo-Electron Microscopy 18

D. Introduction to Hydrogen-Deuterium Exchange Mass Spectrometry (HDX-MS) 21

E. Introduction to AlphaFold: Deep Learning for Protein Structure Prediction 25

F. Nitrogenase biology 29

Chapter II Manual Blot-and-Plunge Freezing of Biological Specimens for Single-Particle Cryogenic Electron Microscopy 33

A. Introduction 34

B. Methods 36

C. Results 49

D. Discussion 51

E. References 54

Chapter III Domain organization and conformational dynamics of a p90RSK2:ERK2 complex 58

A. Introduction 59

B. Method 65

C Results 73

D. Discussion 92

Chapter IV Key Motifs in the C-terminal Tail Contribute to ATP Binding of AGC Kinases 95

A. Introduction 96

B. Methods 103

C. Results and Discussion 104

Chapter V Future directions 116

A Introduction 117

B. Preliminary results 119

References 124

LIST OF FIGURES

Figure 1.1	Protein kinase fold and conserved motifs	6
Figure 1.2	The MAPK pathway and domain organization of p90RSK	10
Figure 1.3	The C-tail adopts multiple conformations in AGC kinases	12
Figure 1.4	CaMK Regulation	14
Figure 1.5	RSK Activation Mechanism Involves Members of Three Different Kinase Families.	19
Figure 1.6	Overview of Cryo-Electron Microscopy (cryo-EM) and Its Role in Structural Biology	22
Figure 1.7	Overview of HDX-MS	27
Figure 1.8	Overview of AlphaFold and Its Role in Protein Structure Prediction	31
Figure 1. 9	From the Nitrogen Cycle to the Structural Features of Nitrogenase and Its Catalytic Cycle	35
Figure 2.1	Specimen plunging room and required equipment	52
Figure 2.2	Prepared liquid ethane	53
Figure 2.3	Representative apoferritin images obtained using the manual blot-and-plunge technique	54
Figure 2.4	Representative atlas of a sub-optimal cryoEM grid	55
Figure 3.1	p90RSK domain organization and consensus activation mechanism of RSK2 by ERK2 and PDK1	65
Figure 3.2	Crosslinked RSK2:ERK2:ORF45 complex formation	72
Figure 3.3	Single-particle cryo-EM image processing workflow for the crosslinked RSK2:ERK2:ORF45 complex	76
Figure 3.4	Cryo-EM structure of the RSK2:ERK2:ORF45 complex	79
Figure 3.5	Trimer fit and statistical analysis	80
Figure 3.6	Dimer structure is CTK:ERK2	81
Figure 3.7	Monomer structure of ERK2	82
Figure 3.8	Rigid body motion of CTK:ERK2	85
Figure 3.9	Multiple sequence alignment of human RSK1 and RSK2	86
Figure 3.10	CTK C-lobe αF helix flexibility	87
Figure 3.11	NTK is the most mobile domain	89
Figure 3.12	Region of the interkinase linker (purple, red) are ordered in the RSK:ERK complex	91
Figure 3.13	Linker becomes partially ordered in the RSK:ERK trimer	92
Figure 3.14	Zoom in view of interkinase linker interaction with NTK, CTK, and ERK	95
Figure 3.15	The N-lobe of NTK is malleable	96
Figure 4.1	Conserved C-tail and activation loop in AGC kinases	101
Figure 4.2	Schematic representation of p90RSK (A), PKC (B), Akt (C), and PKA (D) domain structure	104
Figure 4.3	The TIM motif adopts a sequence conserve and unique fold	106
Figure 4.4	Sequence alignment of the glycine-rich loop (A) and the active site tether (B) of PKCs, AKTs, PKAα, and p90RSKs.	111
Figure 4.5	ATP binding pocket of the PKA catalytic subunit	112

Figure 4.6	Model of p90RSK2 (A) and p90RSK2:ERK2 complex (B) in the apo state	114
Figure 4.7	Structure of AKT1 in the AMP-PNP Bound Form (A) and Structure of the Catalytic Domain of Human PKCα in Complex with NVP-CJL037 (B).	114
Figure 4.8	Structure of PKCα with the inhibitor (A) and structure of PKCι kinase domain in ATP bound form	115
Figure 4.9	Structure of the RIIβ Holoenzyme with Both Products Captured in the Crystal Lattice (A)	117
Figure 4.10	Structure of PKCβII	118
Figure 5.1	Fab generation against RSK2 and experimental workflow	122
Figure 5.2	Characterization of nine Fab candidates with high affinity and specificity for RSK2.	125
Figure 5.3	Complex formation of Fab1, Fab5, and Fab9 with RSK2	127

LIST OF ABBREVIATIONS

2D	Two-dimensional
3D	Three-dimensional
Å	Angstrom
AF	AlphaFold
AL	Activation loop
ANOVA	One-way analysis of variance
AST	Active site tether
cAMP	Cyclic adenosine monophosphate
CaMK	Calcium/calmodulin-dependent protein kinase
CASP14	Critical Assessment of protein Structure Prediction
Chk2	Checkpoint kinase 2
CLT	C-lobe tether
CryoEM	Cryogenic electron microscopy
Cryo-ET	Cryo-electron tomography
CTK	C-terminal kinase of p90 ribosomal s6 kinase
CtL	C-terminal Linker
CLS	Coffin-Lowry Syndrome
C-tail	C-terminal tail
Da	Dalton
DAG	Diacyl glycerol
DAPK3	Death-associated protein kinase 3
EDTA	Ethylenediaminetetraacetic Acid

ERK	Extracellular regulated kinase
EPKs	Eukaryotic protein kinases
EGF	Epidermal growth factor
Fe	Iron
FeMoco	FeMo-cofactor
FeP	Iron protein
FL	Full-length
FPLC	Fast Protein Liquid Chromatography
G-loop	Glycine-rich loop
HC	Heavy chain
HDXMS	Hydrogen deuterium exchange mass spectrometry
HM	Hydrophobic motif
HOG	Histogram of Ordered Gradients
HSD	Tukey's Honestly Significant Difference
Hsp90b	Heat shock protein 90b
IDRs	Intrinsically disordered regions
K_d	Dissociation equilibrium constant
KSHV	Kaposi's sarcoma-associated herpesvirus
KSR2	Kinase suppressor of Ras 2
LC	Light chain
LC-MS	Liquid chromatography coupled to mass spectrometry
LN_2	Liquid nitrogen
MAPK	Ras-mitogen-activated protein kinase

MAPKAPK	MAPK-activated protein kinase
MEK1	Mitogen-activated protein kinase kinase 1
Mo	Molybdenum
MoFeP	Molybdenum-iron protein
MSAs	Multiple sequence alignments
NLT	N-lobe tether
NMR	Nuclear magnetic resonance
NTK	N-terminal kinase of p90 ribosomal s6 kinase
N_2	Dinitrogen
NH_3	Ammonia
NtL	N-terminal Linker
ORF45	Open reading frame protein 45 of Kaposi sarcoma herpesvirus
pLDDT	Predicted Local Distance Difference Test
PAK1	p21-activated kinase 1
PDB	Protein Data Bank
PDK1	Phosphoinositide-dependent kinase 1
PIF	PDK1-interacting fragment
PKA	Protein Kinase A
PS	Pseudosubstrate
R	Regulatory
R_2C_2	Holoenzyme complex
revD	reverse D-motif
RH	Relative humidity

RSK	p90 Ribosomal S6 Kinase
S200	Size exclusion chromatography
SAXS	Small angle x-ray scattering
SLiMs	Short linear motifs
SLK	Ste20-like kinase
STK10	Ser/Thr kinase 10
TIM	Tor interaction motif
TM	Turn motif
TNBC	Triple-negative breast cancer
V	Vanadium

ACKNOWLEDGEMENTS

It took a village for this PhD to be born, and there are many people I want to thank - some of whom I may unintentionally forget, due to my aging brain.

First and foremost, I would like to thank my parents for bringing me into this world, for teaching me how to live a meaningful life, and for showing me how to care deeply about the people and community around me. Their resilience and hard work have been a constant source of motivation, especially during the toughest times. They made the life-altering decision to move to the U.S., leaving behind their home, friends, and family so that my brother and I could have a better life in a country full of opportunities. They instilled in us a deep love - for math, and for learning - and a sense of hope for a brighter future. Whenever I felt tired or wanted to give up, I thought of them working minimum-wage jobs, rarely taking a day off. That thought gave me the strength to keep going. I want to live a life that makes them proud.

Next, I would like to thank my advisor, Professor Susan Taylor. She generously welcomed me into her lab in my fifth year, at a time of transition in my PhD journey. I'm not sure whether she fully knew the circumstances I was coming from, but I'm incredibly grateful that she believed in me, offered me a meaningful project, and worked with me patiently as I found my footing again. One of the things I truly appreciated about working with her is her boundless energy and enthusiasm - every discovery, no matter how big or small, was met with genuine excitement. I continue to be inspired by her sharpness and passion for science, and I can only hope to maintain that same curiosity and drive throughout my own career.

Next, I would like to thank my co-advisor, Professor Mark Herzik. Although we sometimes had different perspectives and working styles, I truly appreciate the mentorship I received from him. From helping set up the lab to mentoring undergraduates and writing manuscript and applying

for grants and fellowships, I gained valuable experience under his guidance. I've always admired his works - it's clear that he puts a lot of thought and effort into crafting everything, from talks, to manuscripts to grants. I also appreciated the way he explained complex concepts, which often helped things click for me. Thank you for your patience as I was learning cryo-EM.

Next, I would like to thank Mar Matyszewski for being a steady and supportive presence throughout my PhD journey when I am on the scope. I'm especially grateful for your patience and guidance during times when I didn't know where to turn for help with data analysis or when things unexpectedly went wrong at the microscope - which, as we know, can happen at any moment. Thank you for not only being patient with me, but with everyone who uses the facility. Your willingness to remain neutral and professional during challenging situations did not go unnoticed, and I truly appreciated having your calm support during those times.

Finally, I would like to thank my undergraduate advisors, Dr. Wade Van Horn and Dr. Jacob Hilton, for inspiring me to pursue research. Their knowledge and passion deeply intrigued me. I'm especially grateful Dr. Wade Van Horn who chose to give me a chance, selecting me from a pool of undergraduates even though I had no prior research experience and was already a junior - considered by some to be a late start for entering a research lab. Thank you to Dr. Dustin Luu for your support, especially during moments when imposter syndrome crept in. Your encouragement meant a lot. To my current and former lab members - thank you all. Special thanks to Dr. Evan Kobori for handing me a project with lot of preliminary data, which allowed me to complete my PhD on a reasonable timeline. I also appreciated your calm demeanor during my moments of panic - whether it was about graduation, a complex crashing, or lack of high-resolution data. Thank you to Rodeon Malinovski, Nathan Vu, and Gerald Tan for making the lab an enjoyable place to work. Many thanks to Dr. Jessica Bruystens for your support and for helping me prepare for my practice

talks. And to Dr. Jian Wu, thank you for the beautiful models and figures you created, for teaching me how to make publication-quality figures, and for guiding me through the analysis of published crystal structures. I learned a lot from you. To the rest of the lab members - whether or not our projects overlapped - thank you for being such a fun and supportive group: Dr. Nisha Jonniya, Dr. Pallavi Sharma, Anagha Kalle, Angel Payan, and Frank Ma. Thanks to my mentees and labmates, who supported me with protein prep and day-to-day lab work: Dr. Kendrick Nguyen, Rodeon Malinovski, Nael Mousa, Esther Nguyen, and Sean Shukman.

Next, I would like to thank my comfort zone: Dr. Lisa Liang and soon-to-be Dr. An Hsieh, for being a constant source of mental support from the very beginning of this PhD journey. We started as friends, bonding over shared experiences - family dynamics, being first-generation PhD students - and grew through the many ups and downs that come with this path. Thank you for making life outside the lab feel less lonely. From our first rave and art festival, to traveling together and creating countless memories, your presence made a difference. I hope that as we graduate and move forward on our individual paths, we continue to maintain this friendship and always have each other's backs. Thank you for being there - patting me on the back, crying with me through the hardest times, and giving me advice on what to do and who to talk to. I deeply appreciate both of you.

Last but not least, I'm also grateful to the many friends I made during my time at UC San Diego - whether through campus mentorship programs, the Chemistry International Friendship group, or other programs I was fortunate to be part of. A few I'd like to mention include Charlene Her (Yeo Lab), Yajie Gu (Corbett Lab), Eshani Hettiarachchi (Grassian Lab), Lisa Liang (Miller Lab), An Hsieh (Mishanina Lab), Debolina Sarkar (Muller Lab), and Safal Shrestha (Obara Lab). Thank you for the random science conversations - some of them sparked new ideas for my own

project. Thank you to the Andres Leschziner Lab for providing computational resources, and to the many labs on campus that generously let me use their instruments while ours was still being set up.

To all the names I may have forgotten or are too many to list - please know that I truly appreciate every one of you.

Chapter II, in full, is a reprint of the material as it appears in Jove, 2022. **HOANG P. M. NGUYEN**, Kelly L. McGuire, Brian D. Cook, Mark A. Herzik, Jr. *Manual Blot-and-Plunge Freezing of Biological Specimens for Single-Particle Cryogenic Electron Microscopy.* The dissertation author was the primary researcher and author of this paper.

Chapter III, in full, is currently being prepared for submission for publication of the material. **HOANG P. M. NGUYEN**, Evan Kazuo Kobori, Jian Wu, Roland Dunbrack, Mariusz Matyszewski, Rodeon Malinovski, Katherine Chen, Mark Anthony Herzik, Susan Taylor. *Domain organization and conformational dynamics of a p90RSK2:ERK2 complex.* The dissertation author was the primary researcher and author of this paper.

Chapter IV, in part, is currently being prepared for submission for publication of the material. **HOANG P. M. NGUYEN**, Jian Wu, Alexandra Newton, Susan Taylor. *Key Motifs in the C-terminal Tail Contribute to ATP Binding of AGC Kinases.* The dissertation author was the primary researcher and author of this material

Chapter V contains unpublished material coauthored with Jian Wu, Susan Taylor. The dissertation author was the primary author of this chapter.

VITA

2018 Bachelor of Science in Biochemistry, Arizona State university

2020 Master of Science in Chemistry, University of California San Diego

2025 Doctor of Philosophy in Chemistry, University of California San Diego

PUBLICATIONS

H. P. M. Nguyen*, K. L. McGuire*, B. D. Cook*, and M. A. Herzik, Jr. Manual Blot-and-Plunge Freezing of Biological Specimens for Single-Particle Cryogenic-Electron Microscopy. *JoVE*. 2021. doi: 10.3791/62765

H. L. Rutledge, B. D. Cook, **H. P. M. Nguyen**, M. A. Herzik, Jr, F. A. Tezcan. CryoEM structures of the nitrogenase complex during catalytic turnover. *Science.* 2022. doi: 10.1126/science.abq7641

E. Kobori*, **H. P. M. Nguyen***, J. Wu, K. Chen, R. Malinovski, S. Taylor. Structural Insights and biophysical characterization of p90RSK2:ERK2 complex. *Biochemical Journal.* This manuscript is in review.

H. P. M. Nguyen, E. K. Kobori, J. Wu, R. Dunbrack, M. Matyszewski, R. Malinovski, K. Chen, M. A. Herzik, S. Taylor. Domain organization and conformational dynamics of a p90RSK2:ERK2 complex. This manuscript is in preparation.

H. P. M. Nguyen, J. Wu, A. Newton, S. Taylor. Key Motifs in the C-terminal Tail Contribute to ATP Binding of AGC Kinases. This manuscript is in preparation.

FIELD OF STUDY

Major Field: Biochemistry and biophysics
Studies in Structural Biology
Professor Susan Taylor

HONORS AND AWARDS

2024	Department of Chemistry and Biochemistry Travel Grant
2024	Graduate Professional Student Association Travel Grant
2023-2024	Fletcher Jones Dissertation Year Fellowship Program
2020	National Science Foundation Graduate Research Fellowship Program Honorable Mention
2019-2021	Molecular Biophysics Training Grant, trainee

ABSTRACT OF THE DISSERTATION

Domain Organization and Conformational Dynamics of a p90RSK2:ERK2 complex

by

Hoang Phuong My Nguyen

Doctor of Philosophy in Chemistry

University of California San Diego, 2025

Professor Susan Taylor, Chair
Professor Mark Herzik, Co-Chair

The human body contains over 500 kinases, all of which adopt a similar fold and share conserved motifs in the kinase core. Since the first crystal structure of protein kinase A (PKA) was solved more than three decades ago, extensive studies across various time and length scales have uncovered the mechanisms and medical relevance of the kinase core in diverse biological contexts. However, the future of kinase signaling research lies in understanding the structure and mechanism of full-length kinase complexes. These complexes often involve cross-talk between different

kinase families and include intrinsically disordered regions (IDRs) that are critical for regulation. In this work, we investigate the p90RSK2:ERK2 complex, a valuable model for exploring these aspects. p90RSK2 lies downstream of the Ras/MAPK pathway and plays important roles in cancer, neurodegeneration, and cardiac disease. It features a rare tandem kinase architecture: the N-terminal kinase domain (NTK) belongs to the AGC kinase family, while the C-terminal kinase domain (CTK) belongs to the CaMK family. Activated by ERK2, p90RSK2 forms a stable complex in vitro, representing a unique opportunity to study the cross-talk between three different kinase families. Additionally, we examine the viral protein ORF45, a non-catalytic modulator that disrupts this signaling pathway in cells and stabilizes the p90RSK2:ERK2 complex in vitro. We apply a combination of experimental and computational techniques to study the structure and conformational dynamics of this complex. One chapter outlines a manual method for plunge-freezing biological samples. Subsequent chapters employ cryo-electron microscopy (cryo-EM) and AlphaFold modeling to elucidate domain organization and dynamic behavior. We also analyze published structures and sequence homology to investigate conserved C-tail motifs in AGC kinases, including p90RSK2, and propose a model for how the N-lobe senses the C-tail. Based on this, we suggest a potential interaction between mTORC2 and p90RSK2. Finally, we present promising preliminary data on Fab fragments developed in collaboration to stabilize p90RSK2. These tools offer a path forward for solving the first full-length structure of p90RSK2 and stabilizing the p90RSK2:ERK2 complex for future structural studies.

Chapter I

Introduction

A. Core motifs and conserved structural elements of protein kinases.

Protein kinases play a pivotal role in cellular regulation and are encoded by approximately 1.7% of the human genome (Manning, Whyte, Martinez, Hunter, & Sudarsanam, 2002) . These enzymes function by transferring the γ-phosphate group from ATP to specific substrate proteins, a process that often induces structural or functional changes in the target (Kornev & Taylor, 2015; Taylor, Ilouz, Zhang, & Kornev, 2012; Taylor & Kornev, 2011) . It is estimated that nearly one-third of all human proteins undergo phosphorylation, highlighting the extensive regulatory reach of kinases (Cohen, 2002) . When kinase activity is disrupted, it can lead to a variety of diseases such as cancer, diabetes, and neurological conditions. Due to their critical role in signaling pathways, kinases have become a major focus for pharmaceutical development, particularly for small molecule inhibitors. As of September 2024, 82 kinase inhibitors have been approved by the FDA and numerous others are in advanced clinical development (Roskoski, 2024). Despite their relatively modest catalytic efficiency, kinases act as finely tuned molecular switches, capable of rapidly responding to intracellular cues (Kornev & Taylor, 2015). Their ability to shift between inactive and active states allows for precise control, often mediated through phosphorylation events by upstream kinases - resulting in layered signaling cascades that are a hallmark of cellular regulation (Gógl, Kornev, Reményi, & Taylor, 2019) .

The discovery of phosphorylase kinase in the 1950s marked the identification of the first protein kinase (Krebs, 1998) . By the early 1980s, researchers had recognized protein kinases as one of the most expansive gene families, tracing their origin to a shared evolutionary ancestor (Barker & Dayhoff, 1982; Walsh, Perkins, & Krebs, 1968) . Although cAMP-dependent protein kinase (PKA) was the second kinase to be discovered, it was the first for which the three-

dimensional structure was resolved, establishing it as the foundational structural model for the kinase family (Knighton, Zheng, Eyck, Ashford, et al., 1991) .

Protein kinases share a characteristic bilobal structure, with the smaller N-terminal lobe being flexible and primarily involved in ATP binding (Fig. 1A). This lobe is composed of five β-strands and a conserved, movable αC-helix. A glycine-rich loop (G-loop) between the β1 and β2 strands assists in ATP binding by orienting the γ-phosphate for transfer (Fig. 1B). A conserved lysine residue (K72 in PKA) located in the β3 strand plays a crucial role by stabilizing ATP's α- and β-phosphates and forming a salt bridge with glutamate E91, drawing the αC helix toward the active site, and with the D184 from the DFG motif in the C-lobe coordinate ATP and 2 Mg^{2+} (Fig. 1C). This lysine is vital for catalytic activity, and its mutation often renders the kinase inactive (Akamine et al., 2003; Gibbs & Zoller, 1991; Taylor, Ilouz, et al., 2012) . The αC helix itself is highly dynamic, capable of shifting between 'in' and 'out' orientations depending on the kinase's activation state. In some inactive states, the helix may even become completely disordered (Taylor, Shaw, Kannan, & Kornev, 2015; Utepbergenov et al., 2012) .

The larger C-lobe, which is predominantly α-helical, contributes significantly to substrate recognition and mediates interactions with other proteins. Its structural core is formed by the αE, and αF helices, which are buried in a hydrophobic environment, whereas the αD, αH, and αI helix are amphipathic, anchored to the αF/αE core and more exposed to the solvent (Fig. 1A) (Steichen et al., 2012; Taylor & Kornev, 2011; Jie Yang et al., 2005) .

Downstream of αE lies the catalytic loop, which contains the conserved H/YRDXKXXN motif, including the catalytic aspartate responsible for transferring the γ-phosphate of ATP to substrate proteins. The active site resides in the cleft between the two lobes and houses the activation segment. This segment includes the DFG motif - critical for magnesium coordination -

the Activation Loop, which is commonly phosphorylated, and the APE motif, which interacts with the αF helix and the loop connecting αH and αI. Phosphorylation of the Activation Loop typically facilitates alignment of the catalytic HRD motif and the αC helix, as well as proper positioning of the DFG motif, all of which are essential for stabilizing the active conformation of the kinase (Fig. 1D). The P+1 loop which binds the P+1 residue in the peptide substrate. The P site in the activation loop (T197 in PKA) binds to a basic residue in αC helix (His87) when kinase in closed conformation (Hari, Merritt, & Maly, 2013; Kornev & Taylor, 2015; Möbitz, 2015; Modi & Dunbrack, 2021) .

Within the kinase structure, two distinct yet non-contiguous hydrophobic spines span both the N- and C-lobes - these are referred to as the regulatory (R) spine (L106, L95, F185, Y164) and the catalytic (C) spine (A70, V57, L173, I174, L172, M128, M231, L227). The R spine is composed of four hydrophobic residues: one from the β4 strand, another from the αC helix, a conserved histidine or tyrosine from the HRD motif, and a conserved phenylalanine from the DFG motif. This spine is anchored to the αF helix through an interaction with Asp220. Notably, the R spine assembles only in catalytically active kinases and serves as a key marker of enzymes capable of trans-phosphorylating external substrates. In contrast, the C spine is more structurally stable, formed by hydrophobic residues that extend from the αF helix to the N-lobe, with the ATP adenine moiety completing the spine (Fig. 1E) (Kornev, Haste, Taylor, & Eyck, 2006; Kornev, Taylor, & Eyck, 2008; Masterson et al., 2011) .

Since the resolution of the first PKA structure, a variety of studies on different conformational states and dynamic properties have helped elucidate the general kinase fold and its catalytic mechanism (Faezov & Dunbrack, 2023; Knighton, Zheng, Eyck, Ashford, et al., 1991; Kornev & Taylor, 2015; Modi & Dunbrack, 2019, 2021; Taylor et al., 2021; Zheng et al., 1993) .

Despite this progress, a major challenge in the field remains: characterizing full-length kinases in complex with substrates and/or inhibitors to fully understand the influence of regions that extend beyond the catalytic core.

These flanking regions often include intrinsically disordered regions (IDRs), which are rich in regulatory elements and short linear motifs (SLiMs) that can act as phospho-switches or binding modules. Such motifs help mediate kinase activation and control their interactions with other proteins. Many kinases are activated by phosphorylation through other kinases and often form complexes with both substrates and regulatory partners (Alexa et al., 2022; Lu et al., 2020, 2019; P. Zhang et al., 2012) . IDRs surrounding the kinase core are instrumental in coordinating complex signaling pathways, allowing kinases to serve as hubs in dynamic cellular networks (Garai et al., 2012; Gógl, Biri-Kovács, et al., 2019; Gógl, Kornev, et al., 2019; Newton, 2018) .

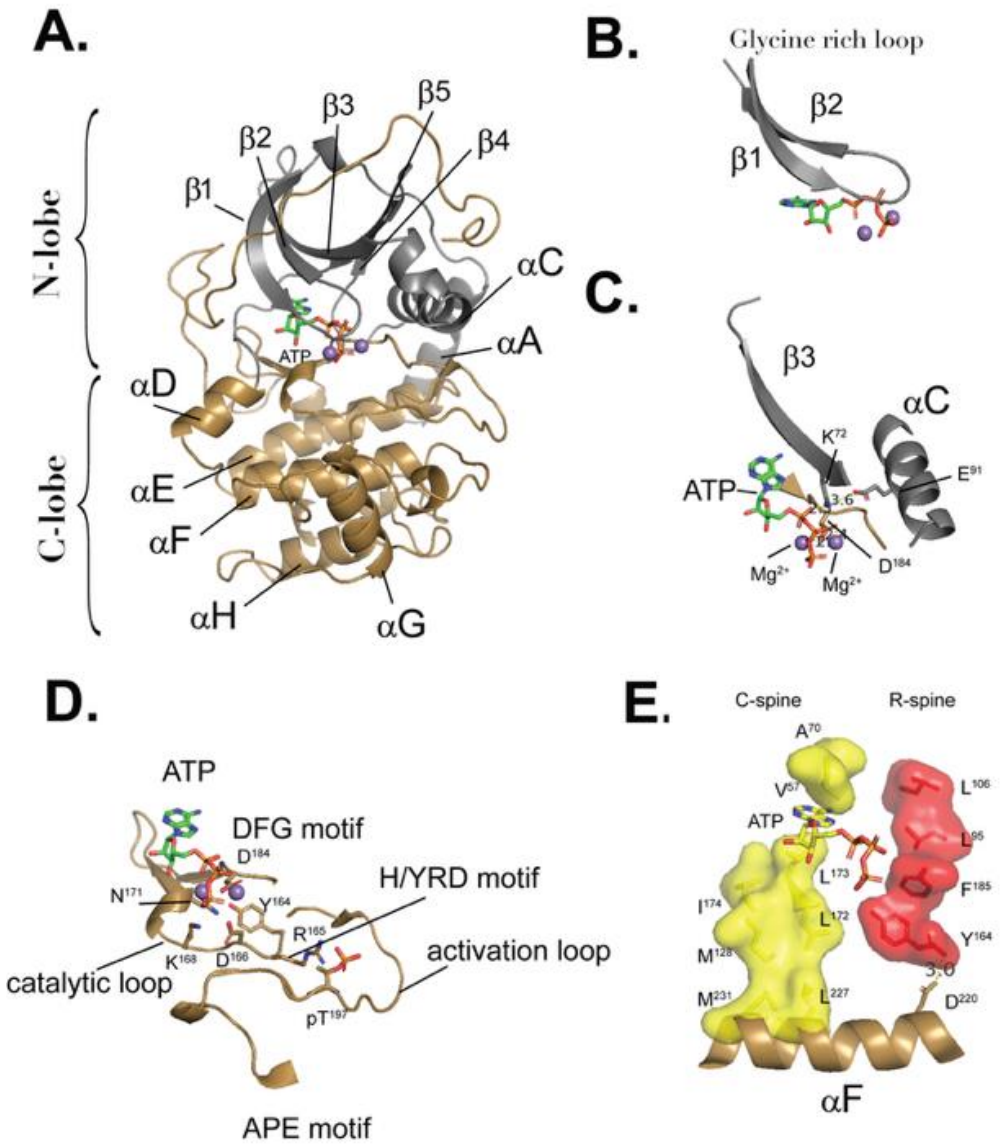


Figure 1.1: Protein kinase fold and conserved motifs. (A) The conserved fold of PKA, representative of all eukaryotic protein kinases (EPKs), consists of an N-lobe composed of five β-strands, the αC-helix—which undergoes dynamic "in" and "out" conformations—and the N-terminal αA-helix, which plays a role in localization. The C-lobe, rich in α-helices, is critical for protein–protein and protein–substrate interactions. **(B)** The glycine loop, formed by β1 and β2 strands, coordinates ATP and adopts either an open or closed conformation to accommodate various inhibitors or ATP analogs. **(C)** Key residues—K72 on the β3 strand, E91 on the αC-helix, and D184 from the DFG motif—coordinate ATP binding and interaction with two Mg^{2+} ions. **(D)** The catalytic loop and activation loop contain critical motifs (DFG, H/YRD, and APE) that play essential roles in both trans- and cis-phosphorylation. **(E)** The hydrophobic C-spine and regulatory R-spine are internal structural features of PKA. Anchored to the αF-helix via residues D220, M231, and L227, these spines are key determinants of the active or inactive conformational state of PKA.

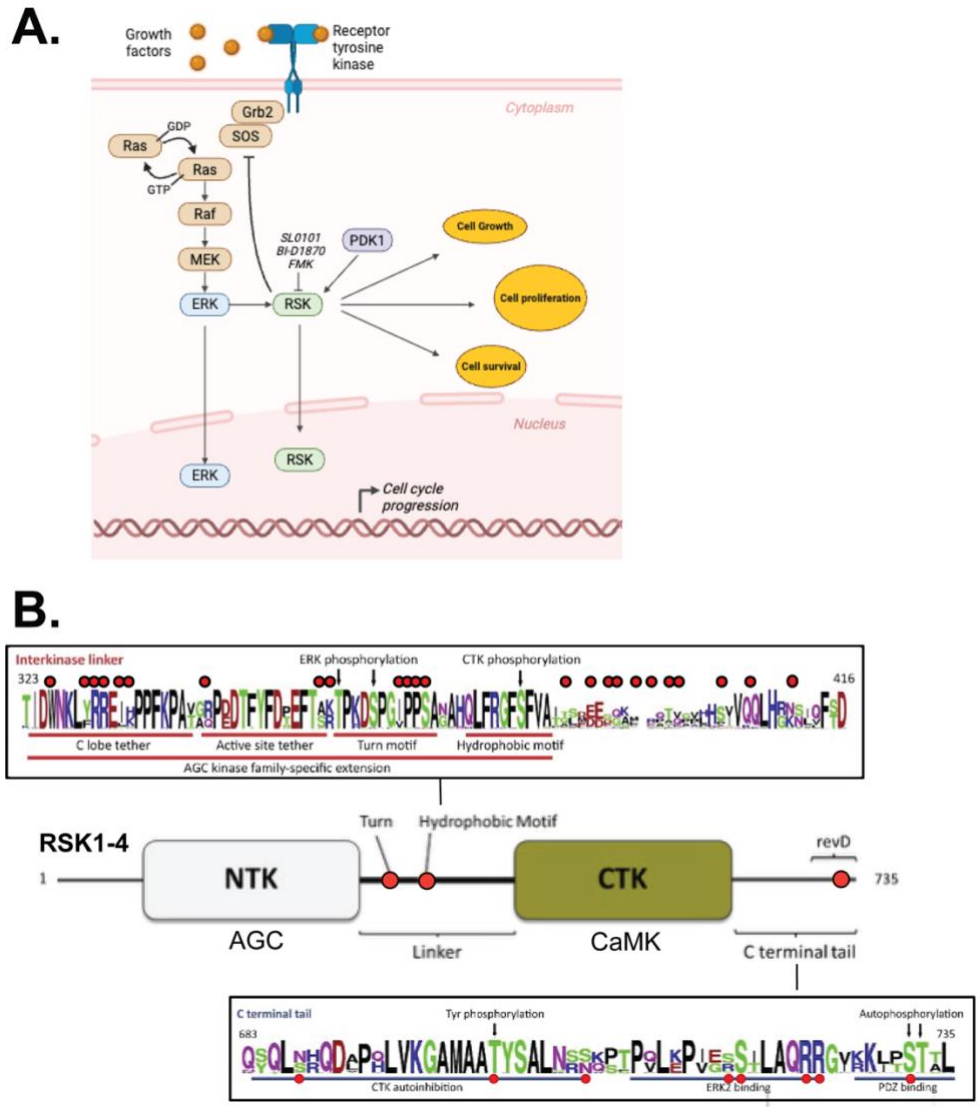
B. RSK biology and important motif and activation mechanism

Studying p90 Ribosomal S6 Kinase (RSK) offers valuable insight into how full-length kinases can form higher-order complexes and interact with intrinsically disordered regions (IDRs). RSK is a member of the MAPK-activated protein kinase (MAPKAPK) family and functions downstream of the Ras/MAPK signaling cascade (Fig. 2A). This pathway is among the most thoroughly investigated in cellular biology, largely due to the prevalence of activating mutations in key components such as KRAS and BRAF, which are frequently implicated in cancers like melanoma (Anjum & Blenis, 2008; Cargnello & Roux, 2011; ZHANG & LIU, 2002) .

Activation begins when extracellular ligands like epidermal growth factor (EGF) bind to their receptors (receptor tyrosine kinase), triggering Ras activation via GDP-GTP exchange. Ras then activates RAF, which in turn phosphorylates MEK. MEK subsequently activates ERK2 through phosphorylation, and ERK2 then activates RSK. Although RSK is initially localized in the cytoplasm, it undergoes dynamic relocation to the membrane by myristylation or ERK escorting and can later move into the nucleus or remain in the cytoplasm, where it phosphorylates a wide range of targets involved in protein synthesis, cell proliferation, cell cycle progression, and more (Fig. 2A) (Anjum & Blenis, 2008; Richards, Dreisbach, Murphy, & Blenis, 2001) . The RSK family comprises four isoforms (RSK1-4), which appear to have distinct biological roles based on their differential tissue expression and association with various disease phenotypes. While RSK1-3 are broadly expressed across tissues, RSK1 is especially abundant in the kidney, lung, and pancreas. RSK2 and RSK3 are also prominent in muscle and cardiac tissue. RSK4 is less widely expressed but has been detected in tissues such as the brain, heart, kidney, cerebellum, and muscle (Dümmler et al., 2005; Zhao, Bjørbæk, Weremowicz, Morton, & Moller, 1995) . Disruptions in RSK function have been linked to various diseases. Notably, mutations in the RSK2 gene are the

underlying cause of Coffin-Lowry Syndrome (CLS), a genetic neurological condition that typically manifests during childhood (Liu, Zhang, Smolen, Cleary, & Byrne, 2022; Trivier et al., 1996; Zeniou, Ding, Trivier, & Hanauer, 2002) . Individuals with CLS often exhibit cognitive impairments along with skeletal abnormalities, particularly affecting the fingers and hands. These RSK2 mutations are dispersed across the protein, with a concentration in the two kinase domains, and to a lesser extent, in regulatory regions such as the hydrophobic motif (HM) within the linker and the reverse D-motif (revD) in the C-terminal tail. Several of the mutated sites correspond to evolutionarily conserved residues essential for kinase function - such as those in the HRD catalytic motif, activation loops, and αC helices - indicating that many CLS-associated mutations likely impair RSK2 enzymatic activity. In addition to its role in CLS, RSK has also been implicated in cancer. Both genetic alterations and changes in expression levels of different RSK isoforms have been reported in various tumor types. Among these, RSK1 and RSK2 are particularly significant in the context of triple-negative breast cancer (TNBC), where they appear to contribute to cancer progression and survival. (Aronchik et al., 2014; Spirrison & Lannigan, 2024; E. B. Wright & Lannigan, 2023) .

Each isoform of RSK includes two functional kinase domains - a C-terminal kinase (CTK) and an N-terminal kinase (NTK) - both of which are separated and surrounded by long IDRs. The NTK is preceded by an N-terminal tail and connected to the CTK via a flexible linker, while the CTK is followed by a C-terminal tail (Fig. 2B) (Bj∅rbæk, Zhao, & Moller, 1995; Fisher & Blenis, 1996; Jones, Erikson, Blenis, Maller, & Erikson, 1988) .



<u>Figure 1.2:</u> The MAPK pathway and domain organization of p90RSK. (A) Schematic representation of the MAPK pathway, which is initiated by the binding of growth factors to their receptors, triggering a signaling cascade that activates a series of kinases, including Ras, Raf, MEK, ERK, and RSK. Once activated, RSK phosphorylates various substrates in the cytosol and nucleus, regulating a wide range of cellular processes. **(B)** Domain organization of RSK1–4 isoforms. RSK contains two kinase domains: the N-terminal kinase (NTK), which belongs to the AGC kinase family, and the C-terminal kinase (CTK), which is part of the CaMK family. The intrinsically disordered inter-kinase linker and the C-terminal tail are critical for RSK regulation and are hotspots for disease-associated mutations. Red dots indicate cancer-related mutations as documented in the COSMIC database.

The N-terminal kinase domain (NTK) of RSK belongs to the AGC family of kinases, a group that also includes PKA, PKC, PKG, and AKT. A defining characteristic of AGC kinases is a conserved regulatory region at the C-terminus - often referred to as the AGC tail - which plays a critical role in controlling kinase activity. This tail wraps around the catalytic domain, supporting a closed and active conformation of the kinase. When RSK adopts an inactive, open configuration, the tail disengages from the core domain. The AGC tail is organized into three main segments that establish distinct interactions with the kinase structure: the C-lobe tether (CLT), the active site tether (AST), and the N-lobe tether (NLT). The CLT, positioned at the N-terminal region of the tail, binds securely to the C-lobe and includes a conserved PXXP motif thought to mediate protein-protein interactions that stabilize this tethering. This motif illustrates the AGC tail's function as a regulatory element that can act across domains (Arencibia, Pastor-Flores, Bauer, Schulze, & Biondi, 2013; Kannan, Haste, Taylor, & Neuwald, 2007; Pearce, Komander, & Alessi, 2010; Taylor et al., 2022) . The AST is a more flexible segment that plays a direct role in facilitating ATP binding at the active site. It includes the conserved $FD(X)_{1-2}F/Y$ sequence - also known as the Ade motif - which is essential for effective ATP coordination in the active conformation. This region also serves as the binding site for PDK1, the kinase recognized as a master regulator within the AGC family (Biondi et al., 2000; Good et al., 1998; Mora, Komander, Aalten, & Alessi, 2004) . The NLT is located at the extreme C-terminus and engages the αC helix within the N-lobe of the kinase, contributing to its structural integrity. It contains both the turn motif (TM) and the hydrophobic motif (HM), which are key phosphorylation sites. The TM enhances thermal stability and, in some contexts, enzymatic function. The HM, typically with a FXXFS consensus sequence, occupies a hydrophobic groove known as the PDK1-interacting fragment (PIF) pocket - formed between the αC helix and β4 strand. Unlike many of its substrates, PDK1 lacks an intrinsic HM

and instead binds the phosphorylated HM of target kinases to align their activation loops for phosphorylation in trans (Fig. 3) (Kannan et al., 2007; Kazanietz & Lemmon, 2011; Taylor et al., 2022; Biondi et al., 2000)

A more recent discovery revealed the presence of a Tor interaction motif (TIM) within the AST of PKCβII, where it regulates HM phosphorylation. Similar TIM sequences have been identified in other AGC kinases, including RSK, although their exact roles in these contexts remain to be fully elucidated (Baffi et al., 2021; Baffi & Newton, 2022; Chou et al., 2020; Facchinetti et al., 2008; Ikenoue, Inoki, Yang, Zhou, & Guan, 2008) .

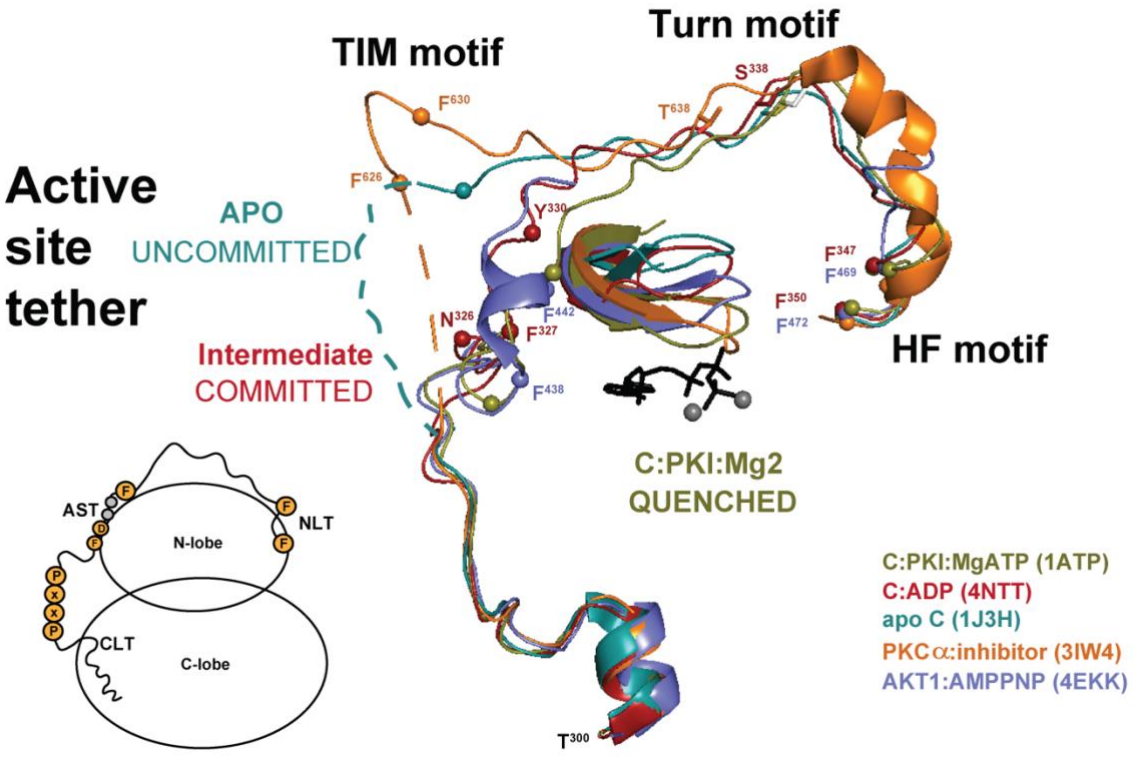


Figure 1.3: The C-tail adopts multiple conformations in AGC kinases. In the apo state (colored teel) (PDB: 1J3H), part of the C-tail is missing density and adopts an open (uncommitted) conformation. In the intermediate state (colored in red) (PDB: 4NTT), the C-tail adopts a committed conformation, positioned in a half-open, half-closed state. In the quenched state (colored deep olive) (PDB: 1ATP), the C-tail is closest to ATP, and the G-loop also clamp down on ATP to complete the ATP binding pocket. Additionally, the G-loop adopts either a closed or open conformation depending on the conformational state of the PKA catalytic subunit (PKA-c). T300 marks the beginning of the C-tail, while F327 and Y330 are part of the FDDY motif, N326 is part of the NFD motif, and F347 and F350 are part of the hydrophobic motif on the C-tail of PKA-c (colored red). The C-tail of PKCα in complex with an inhibitor adopts an open conformation (shown in orange), while the C-tail of AKT1 in complex with AMPPNP adopts a closed conformation (shown in purple). Important motifs are highlighted: F626 and F630 (PKCα), F438 and F442 (AKT1) are part of the TIM motif, T638 (PKCα), and S338 (PKA-c) are part of the turn motif, and F472 and F469 are part of the HF motif on AKT1. The inset representing the Ctail of AGC kinases with key regions including the C-lobe tether (CLT), the active site tether (AST), and the N-love tether (NLT).

The C-terminal kinase domain (CTK) of RSK belongs to the calcium/calmodulin-dependent protein kinase (CaMK) superfamily, which is a Ser/Thr kinase family activated by the binding of a versatile Ca^{2+}-signal transducer, calmodulin (CaM). A defining feature of this kinase family is a C-terminal autoinhibitory helix that occludes the active site, limiting access to ATP and substrates and thereby reducing basal kinase activity. Unlike many other kinase families, for a subset of members of this family, activation typically does not rely on phosphorylation of the activation loop. Instead, these kinases often exist in a closed conformation with a stable regulatory spine and correctly positioned αC helix. Activation occurs when the autoinhibitory helix is displaced, either by binding of calcium/calmodulin (CaM) or, in the case of CTK, through phosphorylation by an upstream kinase, resulting in catalytic activation (Fig. 4) (Malakhova et al., 2008; Rellos et al., 2010; Temmerman, Simon, & Wilmanns, 2013; Tokumitsu & Sakagami, 2022) .

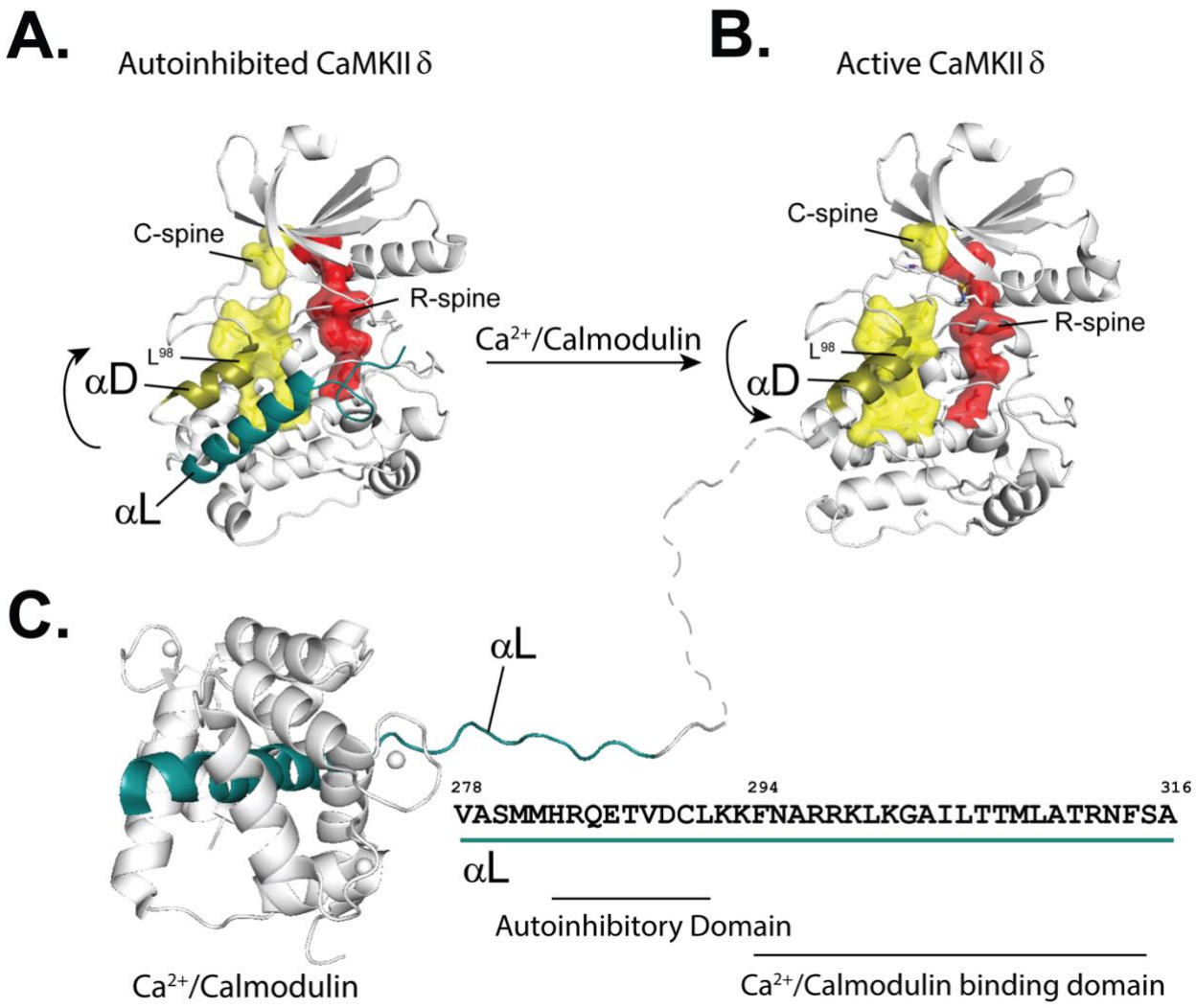


Figure 1.4: CaMK Regulation. (A) The crystal structure of autoinhibited CaMKII (PDB: 2VN9) shows an intact R-spine (red) and a nearly intact C-spine (yellow). The C-terminal autoinhibitory αL helix (deep teal) blocks access to the substrate and nucleotide. The αD helix (deep olive) shifts slightly upward, rotating L98 out of the C-spine. **(B)** Upon binding of Ca^{2+}/calmodulin to the αL helix, a large conformational change occurs. This causes the αD helix to shift downward, rotating L98 into position and completing the C-spine. The active site is then exposed for nucleotide and substrate binding, as observed in the crystal structure of active CaMKII bound to Ca^{2+}/calmodulin (PDB: 2WEL).**(C)** Ca^{2+}/Calmodulin binding to the αL helix. The sequence of the αL helix is shown, with the autoinhibitory domain and the Ca^{2+}/Calmodulin binding domain highlighted.

Both kinase domains of RSK are flanked by intrinsically disordered regions (IDRs) containing short linear motifs (SLiMs), which play roles in regulating activity and promoting assembly of protein complexes. The N-terminal tail varies significantly between RSK isoforms (Romeo, Zhang, & Roux, 2011). In AGC kinases, homologous N-terminal regions contribute to protein stability and localization; for instance, PKA's N-tail contains a myristoylation site for membrane targeting and a stable helix that supports the C-lobe of the catalytic domain (Taylor et al., 2022) . RSK2, similarly, becomes unstable when its N-terminal region is truncated, while RSK3 includes a predicted nuclear localization signal, suggesting isoform-specific functions for the N-terminal tails within the RSK family (Zhao et al., 1995) . Connecting the NTK and CTK is a linker region that includes elements of the AGC C-tail, along with conserved motifs such as the AST/Ade motif, turn motif, TIM, and hydrophobic motif (Fig. 2B). Beyond these motifs, the linker is poorly conserved and lacks bulky hydrophobic residues, characteristic of disordered sequences. Its functional role remains largely unexplored (Gógl et al., 2018; Romeo et al., 2011).

The C-terminal tail of RSK harbors an αL helix that functions as an autoinhibitory element, blocking access to the active site and occluding the P+1 loop necessary for substrate recognition (Malakhova et al., 2008) . Beyond this regulatory helix, the C-tail contains SLiMs critical for interaction with other proteins and complex formation. One key motif is a MAPK docking sequence, also known as the reverse D-motif (revD), which facilitates high-affinity binding to ERK2, RSK's upstream activator. Additionally, a type I PDZ domain-binding motif is present at the extreme C-terminus. Although the functional implications of this motif are not fully understood, some of RSK's known PDZ-interacting partners are also its substrates, suggesting that this region may help recruit a distinct subset of RSK-specific targets (Fig. 2) (Alexa et al., 2015, 2022; Gógl, Biri-Kovács, et al., 2019) .

The activation of RSK is a complex, stepwise process that involves the interplay of multiple intrinsically disordered regions (IDRs) and kinase domains from distinct kinase families (Fig. 5B). This cascade begins with stimulation by epidermal growth factor (EGF), which activates the MAPK signaling pathway. Once active, ERK2 binds to the reverse D-motif (revD) located in the C-terminal tail of RSK and phosphorylates the activation loop of the C-terminal kinase domain (CTK). This phosphorylation event triggers subsequent phosphorylation of the hydrophobic motif (HM) by the CTK itself. Once phosphorylated, the HM serves as a docking site for PDK1, allowing it to phosphorylate the activation loop of the N-terminal kinase domain (NTK). There is also evidence suggesting that ERK2 may phosphorylate the NTK's turn motif, although the sequence and timing of this event relative to other phosphorylation steps remains unresolved. Once the NTK is fully activated, it can phosphorylate downstream substrates that typically contain the RXRXXS/T consensus motif. Additionally, the NTK has the capacity to autophosphorylate its own C-terminal tail. This autophosphorylation reduces its affinity for ERK2, acting as a feedback mechanism to modulate RSK activity (Anjum & Blenis, 2008; Dalby, Morrice, Caudwell, Avruch, & Cohen, 1998; Jensen et al., 1999; Romeo et al., 2011; Roux, Richards, & Blenis, 2003) .

Our interest in RSK is driven by the complexity of its activation mechanism. The process involves the orchestrated activity of four kinase domains derived from three different kinase families: the NTK and PDK1 are part of the AGC family, the CTK belongs to the CaMK group, and ERK2 is a member of the CMGC family (Manning et al., 2002) (Fig. 5A). This multi-kinase assembly, along with essential IDRs, provides a unique model for studying kinase-kinase interactions, particularly because RSK forms a stable complex with its upstream activator ERK2 - a feature that is uncommon among kinase pairs.

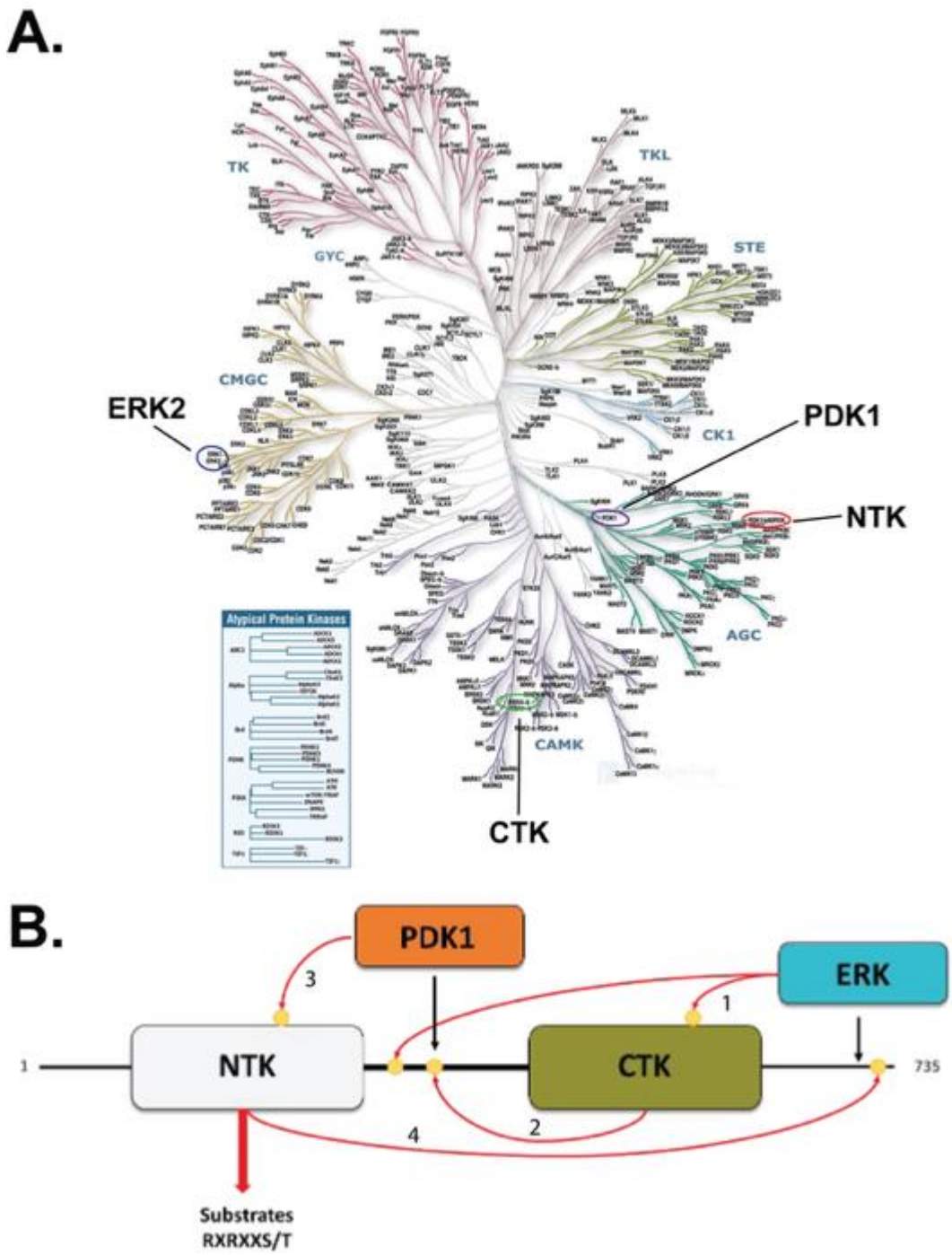


Figure 1.5: **RSK Activation Mechanism Involves Members of Three Different Kinase Families. (A)** The kinome tree of approximately 500 human kinases and their classification into different families. P90RSK (NTK) and PDK1 belong to the AGC kinase family. P90RSK (CTK) belongs to the CaMK family, and ERK2 is part of the CMGC kinase family. Figure adapted from (Manning et al., 2002) . **(B)** The multistep, sequential activation process of P90RSK. Red arrows indicate the direction of phosphorylation, and the numbers represent the sequence of events.

C. Introduction to Cryo-Electron Microscopy

Cryo-electron microscopy (cryo-EM) has emerged as a transformative technique in structural biology, enabling the visualization of macromolecular complexes at near-atomic resolution without the need for crystallization. This method has revolutionized our ability to capture the structural dynamics of biomolecules in their native or close-to-native states, contributing to a deeper understanding of molecular mechanisms underlying cellular function, disease, and regulation (Frank, 2017) .

At the core of cryo-EM is the rapid freezing of biological specimens in vitreous ice, which preserves their hydrated and structurally intact conformations (Depelteau, Koning, Yang, & Briegel, 2020; Jain, Sheehan, Crum, Carragher, & Potter, 2012; Nguyen, McGuire, Cook, & Jr, 2022; Razinkov et al., 2016; Voss, Harder, Olshin, Drabbels, & Lorenz, 2021) . Unlike traditional electron microscopy that often requires chemical fixation and heavy metal staining, cryo-EM avoids these harsh treatments, minimizing artifacts and maintaining biological relevance. Samples are imaged at cryogenic temperatures using a transmission electron microscope, where scattered electrons are recorded to produce two-dimensional (2D) projection images of individual particles embedded in a thin layer of ice.

The advent of direct electron detectors, coupled with advancements in image processing algorithms and increased computational power, has dramatically enhanced the resolution and throughput of cryo-EM. These improvements have given rise to the so-called “resolution revolution,” enabling the determination of structures of increasingly smaller and more dynamic macromolecules, many of which were previously intractable by X-ray crystallography or nuclear magnetic resonance (NMR) spectroscopy (Kühlbrandt, 2014) .

Single-particle cryo-EM, in particular, has gained prominence for its ability to reconstruct three-dimensional (3D) density maps from thousands to millions of 2D projections of individual particles. These maps can be used to model atomic structures, interpret conformational heterogeneity, and study transient intermediate states that are crucial for understanding biomolecular function. In parallel, techniques such as cryo-electron tomography (cryo-ET) and subtomogram averaging have enabled the visualization of larger cellular assemblies within their native cellular environments, providing spatial and contextual insights at molecular resolution (Nogales & Mahamid, 2024) .

Despite its many strengths, cryo-EM poses specific challenges. Sample preparation, including achieving an optimal distribution of particles and preventing preferred orientation, remains a bottleneck for many systems. Additionally, radiation damage, beam-induced motion, and issues related to particle alignment and heterogeneity require careful optimization during data collection and processing (Bai, McMullan, & Scheres, 2015; Chen, Noble, Kang, & Darst, 2019; Cheng, 2018; Han et al., 2020; Herzik, Wu, & Lander, 2019; Lyumkis, 2019; Nogales, 2016) .

Cryo-EM has become an indispensable tool for modern structural biology, complementing traditional techniques and expanding the range of systems accessible to atomic-level interrogation. As the field continues to evolve, ongoing innovations in instrumentation, computational approaches, and specimen preparation promise to further push the boundaries of what is achievable. In the context of this thesis, cryo-EM serves as a central method for elucidating the structure and mechanism of mitochondrial biogenesis (Tom70), nitrogenases and kinases, offering critical insights into its conformational dynamics and mechanisms.

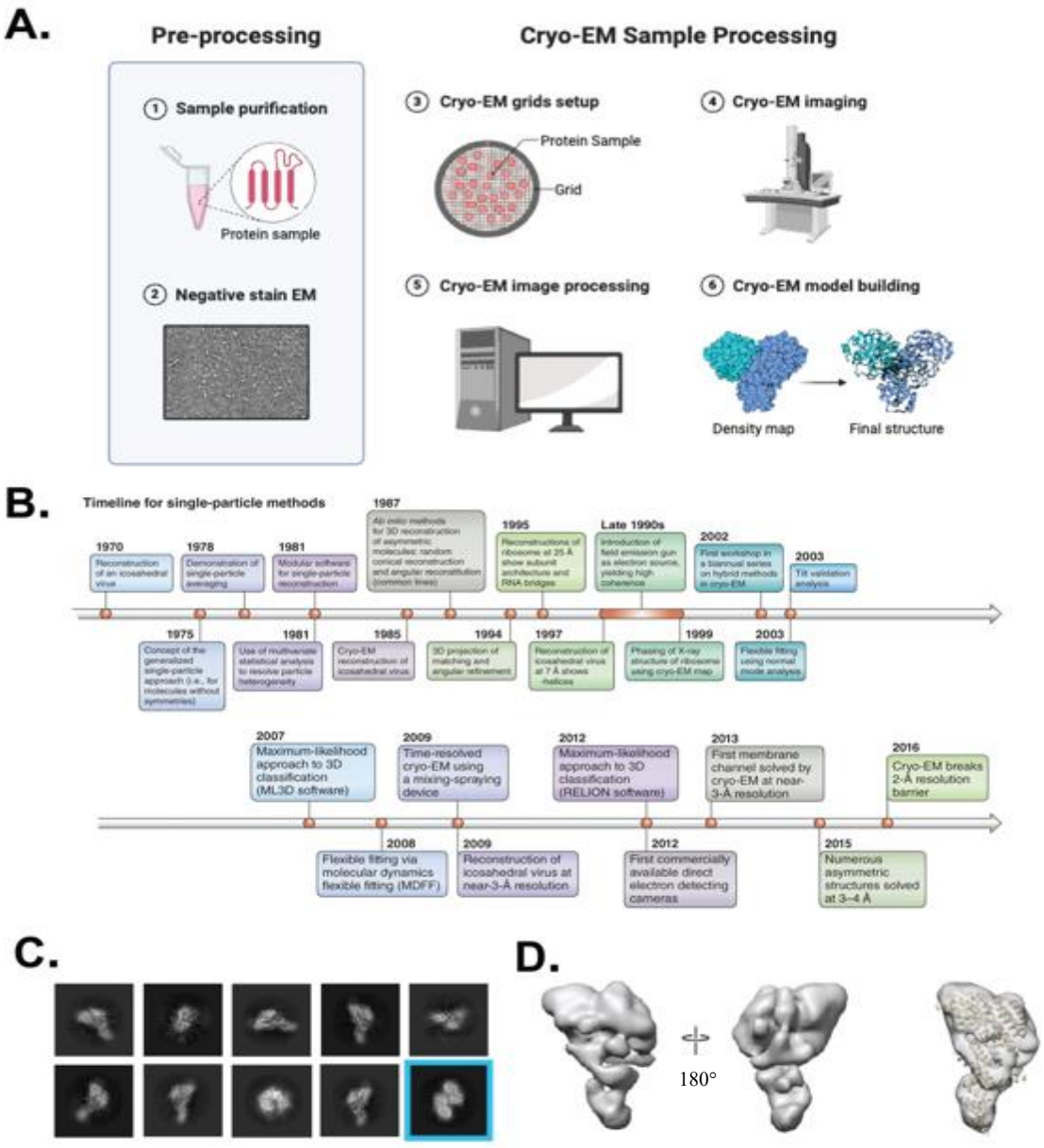


Figure 1.6: Overview of Cryo-Electron Microscopy (cryo-EM) and Its Role in Structural Biology. (A) Schematic workflow of cryo-EM, including the initial screening (pre-processing) steps that require purified samples and negative stain EM to assess overall particle size, shape, and behavior on grids. The cryo-EM process then involves grid preparation (plunge freezing), imaging, data processing, and model building. Figure adapted from Biorender. **(B)** Timeline of key developments in single-particle cryo-EM methods. Figure adapted from (Frank, 2017) . **(C, D)** Example of a challenging cryo-EM sample affected by preferred particle orientations. **(C)** Representative 2D class averages of Tom70 showing dominant orientations. **(D)** Resulting low-resolution reconstruction of Tom70 due to limited angular sampling.

D. Introduction to Hydrogen-Deuterium Exchange Mass Spectrometry (HDX-MS)

Hydrogen-deuterium exchange mass spectrometry (HDX-MS) is a powerful and sensitive biophysical technique used to investigate protein structure, dynamics, and interactions. By exploiting the natural exchange of backbone amide hydrogens with deuterium in D_2O, HDX-MS provides insights into protein conformational flexibility, solvent accessibility, and protein-ligand or protein-protein interactions, even in solution and under near-physiological conditions (Georgescauld, Wales, & Engen, 2019; Josephs et al., 2021; Kopcho, Chang, & Komives, 2019; Lumpkin, Baker, Leschziner, & Komives, 2020; Peacock & Komives, 2021; Weng et al., 2022) .

The principle of HDX lies in the replacement of labile hydrogens—primarily those involved in backbone amide bonds—with deuterium atoms when a protein is exposed to deuterated solvent. The rate of exchange at each amide hydrogen is influenced by local structural elements such as hydrogen bonding, secondary structure, and solvent accessibility. Regions that are highly structured or buried tend to exchange more slowly, whereas flexible, disordered, or solvent-exposed regions exchange rapidly (Vinciauskaite & Masson, 2023).

Following labeling, the reaction is quenched at low pH and temperature to minimize back-exchange, and the protein is proteolytically digested, typically with pepsin under acidic conditions. The resulting peptides are then analyzed by liquid chromatography coupled to mass spectrometry (LC-MS), allowing the determination of mass shifts corresponding to the extent of deuterium incorporation. By comparing the exchange patterns under different conditions—such as in the

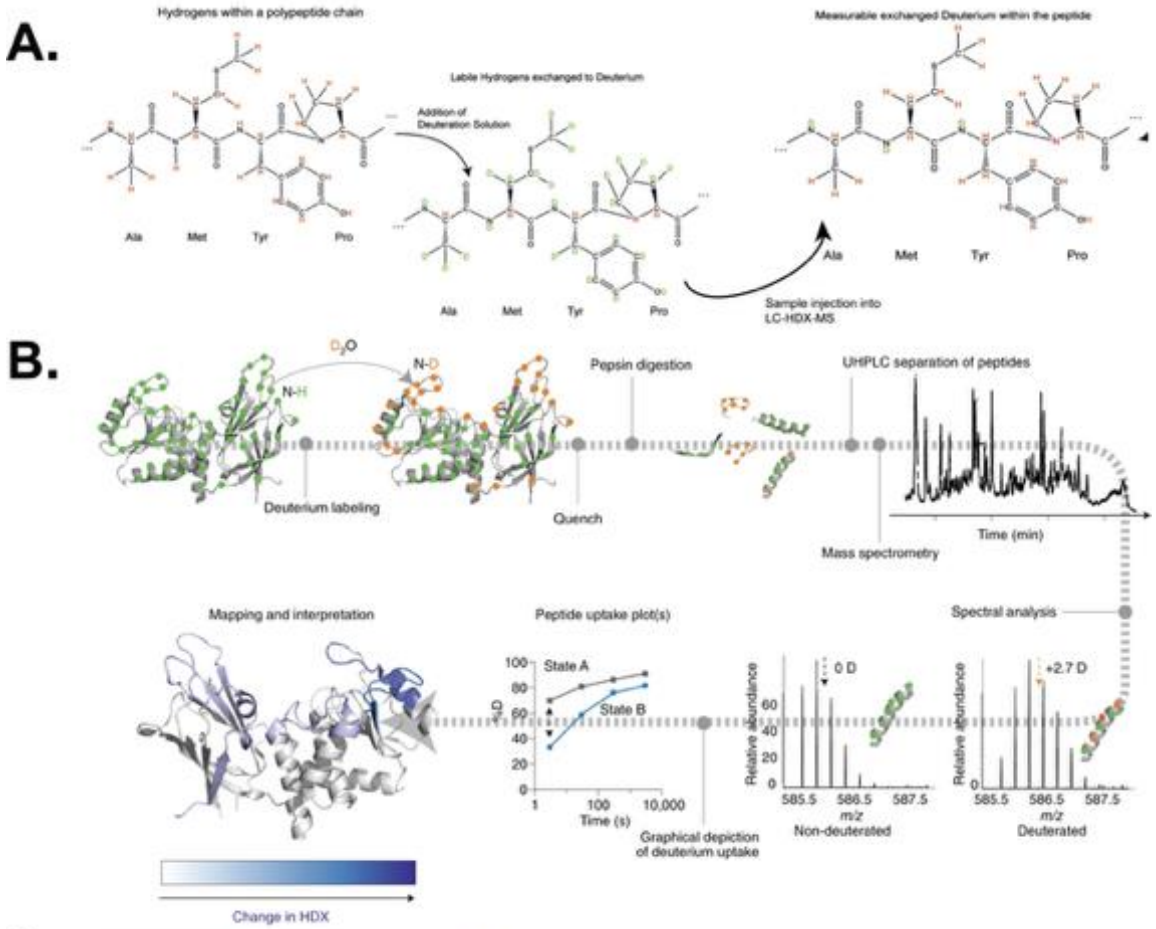
presence or absence of a ligand, cofactor, or binding partner—HDX-MS can reveal conformational changes and interaction interfaces with high spatial resolution, typically at the peptide level (Masson et al., 2019) .

HDX-MS has gained traction as a method of choice for studying dynamic aspects of proteins that are often invisible to static structural techniques such as X-ray crystallography or cryo-electron microscopy. It is particularly advantageous for analyzing large multi-protein complexes, intrinsically disordered regions, membrane proteins, and systems where high-resolution structural data is limited or difficult to obtain. Furthermore, HDX-MS is label-free, requires relatively small amounts of sample, and is compatible with a wide range of buffer conditions, making it a versatile tool in both academic and pharmaceutical research settings.

Despite its strengths, HDX-MS presents several challenges, including limited spatial resolution compared to atomic techniques, potential back-exchange during analysis, and the complexity of data interpretation in regions with overlapping peptides or extensive structural dynamics. However, continued advancements in mass spectrometry instrumentation, protease specificity, and data analysis software have significantly improved both the reliability and resolution of the technique (Lumpkin & Komives, 2019) .

In the context of this thesis, HDX-MS is employed to probe the conformational dynamics of chaperone proteins (Hsp90b), kinases, providing critical insights into domain flexibility, allosteric regulation, interaction surfaces, conformational change. These data complement static structural models and contribute to a more comprehensive understanding of the dynamic behavior of biological macromolecules.

Figure 1.7: Overview of HDX-MS. (A) Conceptual diagram of the HDX mechanism. Upon the addition of deuterium solvent, backbone amide hydrogens and many functional group hydrogens are exchanged for deuterium. However, due to backexchange, upon injection of the sample into the LC system, functional group deuterium exchanges back to hydrogen, while only the backbone amide deuterium remains intact. Figure adapted from (Vinciauskaite & Masson, 2023) **(B)** HDX-MS workflow: Proteins are incubated in a deuterated solution for a specified time, allowing deuterium incorporation into the protein backbone. The reaction is quenched with acidic pH and low temperature. Proteins are then digested by an acid-activated protease, pepsin. The resulting peptides are analyzed using a UHPLC system coupled with a mass spectrometer, where isotopic envelopes of peptides are analyzed and visualized. The levels of deuteration are determined by comparing the average mass (from the intensity-weighted centroid m/z value, marked by arrows) of the peptides. The example mass spectrum shows that the peptide has a deuterium level of 2.7D. Deuterium uptake is plotted across multiple time points, revealing folded, unfolded, bound, and unbound regions of the protein. These differences can then be mapped onto three-dimensional protein structures or models for structural and dynamic interpretation. Figure adapted from (Masson et al., 2019) **(C)** HDX-MS provides insight into the conformational flexibility of human Hsp90b. **(1)** Fractional deuterium uptake of Hsp90b in its apo state at the 2-minute time point, comparing the apo, ADP, and AMPPNP states, mapped onto E. coli Hsp90 (PDB: 2IOP). **(2-7)** Regions that became more protected in the ADP state, including the loop region (253-293) connecting the N-terminal domain (NTD) and middle domain (MD), as well as the ATP binding pocket.


A.
Hydrogens within a polypeptide chain
Ala
Met
Tyr
Pro
Labile Hydrogens exchanged to Deuterium
Addition of Deuteration Solution
Measurable exchanged Deuterium within the peptide
Sample injection into LC-HDX-MS
B.
D2O
N-H
N-D
Deuterium labeling
Quench
Pepsin digestion
UHPLC separation of peptides
Time (min)
Mass spectrometry
Mapping and interpretation
Peptide uptake plot(s)
State A
State B
%D
Time (s)
Graphical depiction of deuterium uptake
Spectral analysis
0 D
+2.7 D
Relative abundance
m/z
Non-deuterated
Deuterated
Change in HDX
C.
1
2
3
4
5
6
7
45°

E. Introduction to AlphaFold: Deep Learning for Protein Structure Prediction

Understanding the three-dimensional structure of proteins is essential for elucidating their biological function, mechanism of action, and interactions with other molecules. Traditionally, experimental techniques such as X-ray crystallography, nuclear magnetic resonance (NMR) spectroscopy, and cryo-electron microscopy (cryoEM) have been the gold standards for structure determination. However, these methods can be labor-intensive, time-consuming, and sometimes inapplicable to certain classes of proteins, particularly membrane proteins or intrinsically disordered regions. The long-standing challenge of accurately predicting protein structures from amino acid sequences—referred to as the "protein folding problem"—has driven decades of research at the intersection of biology, physics, and computer science (Dill, Ozkan, Shell, & Weikl, 2008) .

AlphaFold, a deep learning-based tool developed by DeepMind, represents a major breakthrough in computational structural biology. Released in 2021, AlphaFold2 demonstrated an unprecedented ability to predict protein structures with near-experimental accuracy, as validated in the Critical Assessment of protein Structure Prediction (CASP14) competition. By integrating evolutionary, physical, and geometric constraints within a sophisticated neural network framework, AlphaFold has fundamentally changed the landscape of protein modeling (Akdel et al., 2022; Alderson, Pritišanac, Moses, & Forman-Kay, 2022; Bryant, Pozzati, & Elofsson, 2022; Faezov & Dunbrack, 2023; Jumper et al., 2021; Mirdita et al., 2022a; Pak et al., 2021; Zhong et al., 2021) .

At its core, AlphaFold leverages multiple sequence alignments (MSAs), pairwise residue features, and structural templates to generate high-confidence structural models from primary sequences. The deep learning architecture iteratively refines these features through attention-based mechanisms and a structure module that outputs atomic coordinates. One of the most innovative aspects of AlphaFold is its use of a confidence metric—the predicted Local Distance Difference Test (pLDDT)—which allows users to assess the reliability of the predicted structure at a per-residue level (Jumper et al., 2021) .

The availability of AlphaFold models through publicly accessible databases, such as the AlphaFold Protein Structure Database, has had a transformative impact on the field. Researchers can now access structural models for nearly the entire human proteome and hundreds of other organisms, enabling new discoveries in drug design, enzyme engineering, and understanding disease mutations. Importantly, AlphaFold has also provided structural insights into previously uncharacterized or intractable proteins, as well as flexible or partially disordered regions that elude crystallization (Senior et al., 2020; Tunyasuvunakool et al., 2021; Varadi et al., 2021) .

Despite its remarkable accuracy, AlphaFold has limitations. It is optimized for monomeric protein predictions and may struggle with modeling multi-protein complexes, allosteric changes, or highly dynamic regions. While extensions like AlphaFold-Multimer address some of these challenges, they are still under active development. Moreover, predicted models may not capture conformational ensembles or the effects of post-translational modifications, cofactors, or ligands without additional context or refinement (Callaway, 2022; Evans et al., 2022) .

In this thesis, AlphaFold is employed as a complementary tool to experimental methods for identifying potential interaction interfaces, interpreting HDX-MS data, and understanding

conformational dynamics. Its use accelerates hypothesis generation and structural interpretation, especially in cases where high-resolution structures are unavailable or difficult to obtain. By integrating AlphaFold predictions with empirical data, we aim to construct a more complete and dynamic view of protein function and regulation.

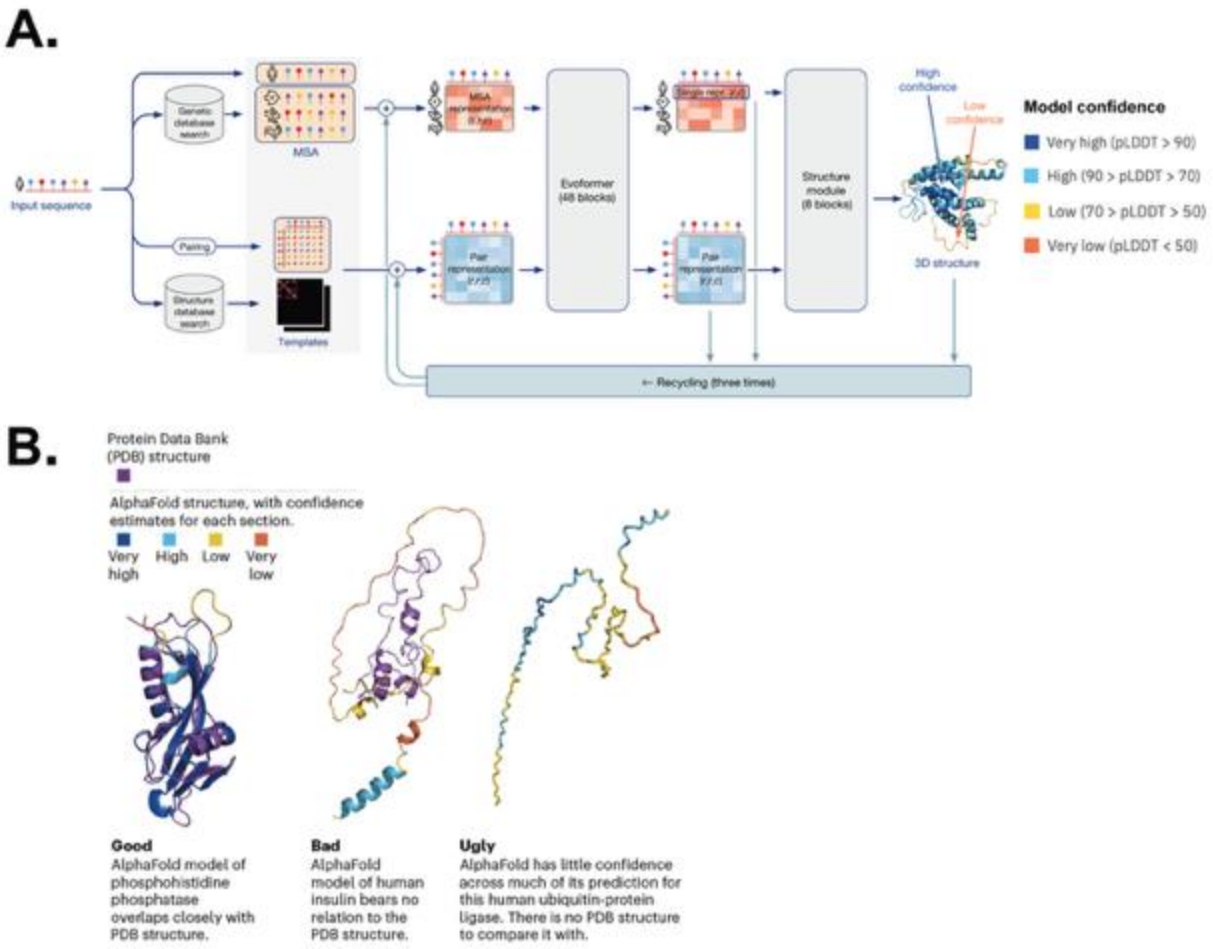


Figure 1.8: Overview of AlphaFold and Its Role in Protein Structure Prediction **(A)** Conceptual diagram of AlphaFold's deep learning process, where an amino acid sequence is used as input to predict a protein's 3D structure, utilizing multiple sequence alignments and existing protein structure databases (PDB) as constraints. The model is evaluated using a confidence score (pLDDT). Figure adapted with modifications from (Jumper et al., 2021) **(B)** Limitations of AlphaFold: While AlphaFold predicts well-folded structures with high accuracy, it is less confident in predicting intrinsically disordered regions or structures lacking existing structural data. Figure adapted from (Callaway, 2022)

F. Nitrogenase biology

Biological nitrogen fixation is a critical biochemical process that sustains the global nitrogen cycle by converting atmospheric dinitrogen (N_2) into bioavailable ammonia (NH_3) ("Understanding Global Change," 2025) . This transformation is catalyzed exclusively by a specialized group of enzymes known as **nitrogenases**, which are expressed by certain prokaryotic organisms including diazotrophic bacteria and archaea. Despite the chemical inertness of N_2, nitrogenase enzymes are able to overcome the considerable activation energy barrier associated with cleaving the triple bond of dinitrogen, under ambient temperature and pressure—conditions under which industrial processes such as the Haber-Bosch method require extreme energy input (Smil, 2001) .

Nitrogenase is a metalloenzyme complex composed of two main protein components: the iron protein (FeP) which is a homodiner, and the molybdenum-iron protein (MoFeP) which is a heterotetramer. Electron transfer from the Fe protein, coupled to ATP hydrolysis, drives the reduction of N_2 at a unique metal cofactor cluster within the MoFe protein called the FeMo-cofactor (FeMoco). The FeMoco is a highly intricate organometallic cluster composed of iron, molybdenum, sulfur, a central carbon atom, and homocitrate, and represents one of the most complex active sites in biology (Rees et al., 2005; Rutledge, Cook, Nguyen, HerzikJr., & Tezcan, 2022) .

Multiple isoforms of nitrogenase exist, classified by the metal content of their active site cofactors: molybdenum (Mo), vanadium (V), or iron (Fe) only. The Mo-dependent nitrogenase is the most efficient and extensively studied variant, although recent work has shed light on the

biochemical capabilities and ecological relevance of the alternative V- and Fe-only nitrogenases, particularly under metal-limiting conditions (Pérez-González et al., 2022) .

Beyond its fundamental biological role, nitrogenase is of considerable interest from a bioinorganic and biotechnological perspective. The enzyme's unparalleled capacity to reduce N_2, along with its ability to reduce a broad range of small molecules—including acetylene, azides, and even carbon dioxide—offers exciting opportunities for sustainable chemistry and synthetic biology (Cai & Minteer, 2018). However, many aspects of its catalytic mechanism, including the precise sequence of electron and proton transfers, the binding mode of N_2, and the dynamics of cofactor activation, remain subjects of active research.

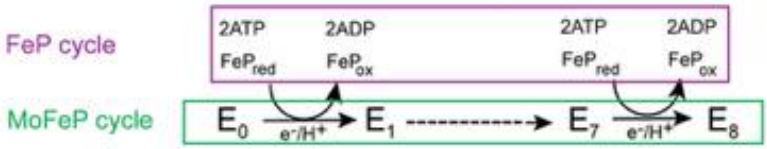
Advancing our understanding of nitrogenase structure, dynamics, and function is essential not only for unraveling the molecular basis of biological nitrogen fixation, but also for informing the development of bioinspired catalysts and engineering nitrogen fixation capabilities in non-diazotrophic organisms—a long-standing goal with implications for agriculture, energy, and environmental sustainability (Shang et al., 2025) .

This section (section F) summarizes the work that was published in https://www.science.org/doi/10.1126/science.abq7641

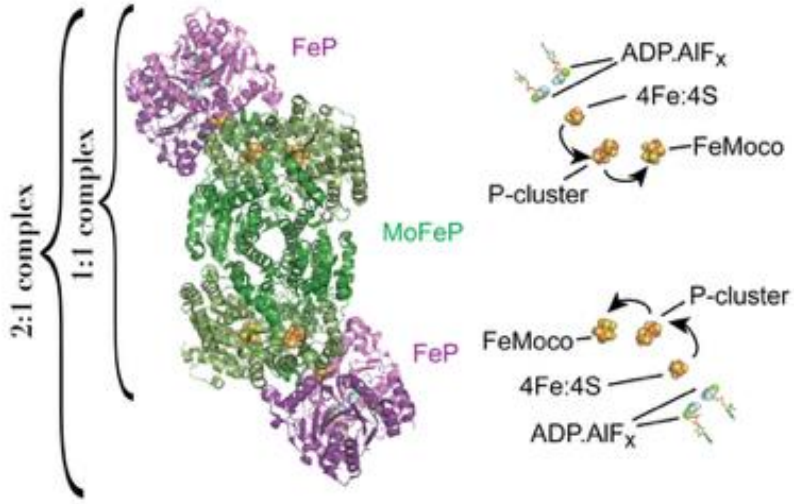
Figure 1. 9: From the Nitrogen Cycle to the Structural Features of Nitrogenase and Its Catalytic Cycle. (A) Nitrogenase catalyzes the conversion of atmospheric nitrogen gas (N_2) to ammonia (NH_3). Each MoFeP catalytic cycle involves eight FeP cycles. **(B)** The crystal structure of the 2:1 FeP:MoFeP complex (PDB: 1M34) reveals key structural components, including the homodimeric FeP subunits (shown in light and dark purple) and the heterotetrameric MoFeP subunit (shown in light and dark green). The structure highlights the positions of nucleotides ($ADP{\cdot}AlF_x$), metalloclusters (4Fe–4S, P-cluster, and FeMoco), and indicates the direction of electron flow with an arrow. **(C)** The nitrogen cycle illustrates the essential role of nitrogenase, which is the only known enzyme capable of converting atmospheric nitrogen into bioavailable ammonia, a critical process for sustaining life in the environment. Figure adapted from ("Understanding Global Change," 2025).

A.

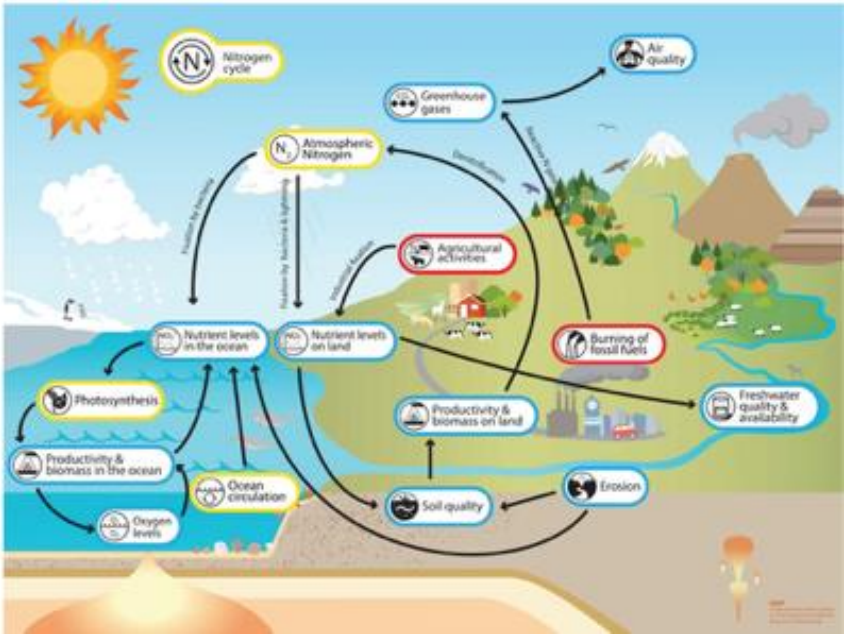
$N_2 + 8\ H^+ + 8\ e^- + 16\ ATP \rightarrow 2\ NH_3 + H_2 + 16\ ADP$



B.



C.



Chapter II

Manual Blot-and-Plunge Freezing of Biological Specimens for Single-Particle Cryogenic Electron Microscopy

A. Introduction

Single-particle cryogenic electron microscopy (cryoEM) is a powerful structural technique that can be used to solve structures of dynamic biological specimens to near- atomic resolution[1,2,3,4]. Indeed, recent advances in direct electron detector technologies[4,5,6,7,8,9,10], improvements in electron sources[4,11,12,13,14], and electromagnetic lens stability[15], coupled with the continued development of data acquisition[16,17] and analysis software packages[18,19], have enabled researchers to now routinely determine structures of well-behaved specimens to 3 Å resolution or better[4,11,13,14,20,21,22,23]. Despite these improved imaging and data processing capabilities, cryoEM grid preparation remains the largest impediment for successful high-resolution structure determination and often serves as a considerable bottleneck in the EM workflow[24,25,26,27].

CryoEM relies on the imaging of biological samples in aqueous solutions that are frozen to form a thin film of "glass- like" ice - a process known as vitrification - that preserves the native biochemical state. Vitrification of biological samples for cryoEM dates back over 40 years[28,29,30] and many techniques and equipment that have been developed for this process rely on the originally detailed blot-and-plunge method[31,32,33,34,35], whereby a small volume of sample (e.g., 1-5 μL) is applied to a specialized EM grid before the excess solution is removed using physical interaction of the grid with blotting paper. The timing of this process is usually empirically determined for each specimen as a critical component of freezing samples is the thickness of the vitreous ice film - if the ice is too thick then imaging quality deteriorates dramatically due to increased scattering of the electron beam while ice that is too thin can restrict

protein orientations and/or exclude particles from the center of the grid foil holes[36]. This reliance on the perfect ice thickness for single-particle cryoEM has led to a wide array of techniques and equipment that can freeze samples, including robotics[37,38], microfluidics[42], and ultrasonic or spraying devices[27,39,40,41,42,43,44]. In recent years, some of the most popular sample preparation devices rely on the use of robotics for automated freezing of samples using the blot-and-plunge technique[45]. While these devices are designed to reproducibly create proper ice thickness for imaging, they often remain too expensive for individual labs to purchase and operate and are generally found within cryoEM facilities at hourly rates for usage. In recent years, the original manual blot-and-plunge technique has come back into increased use[3,47,48,49,50,51,52]. Indeed, a manually operated blot- and-plunge device can achieve high-quality cryoEM grids at a fraction of the cost of robotic counterparts. Furthermore, manual blotting also offers more users control over blotting as researchers can adjust the type of blotting (i.e., back-blotting of the grid, front-blotting of the grid, etc.), and blotting time based on each individual sample and research questions.

In this article, we provide details on how to effectively freeze biological samples using a traditional manual blot-and-plunge vitrification device coupled with a custom-designed dewar platform[53]. Best practices, including preparation of the cryogen, grid handling, sample application, and blotting, as well as common pitfalls and recommendations on how to overcome these hurdles are provided. Advice on how to increase ice thickness reproducibility between grid preparations and how to modify sample blotting based on biological specimen type are discussed. Given the low cost associated with the purchase and operation of the manual plunger described in this manuscript, labs across the globe can prepare biological specimens for cryoEM in a cost-effective and reproducible manner.

B. Methods

I. Prepare the manual plunging environment

NOTE: Estimated operating time: 5-30 minutes

1. Locate the manual plunger in a 4 °C cold room where a humidifier can be co-located to maintain the room close to 100% relative humidity (RH) (**Figure 1A**). CAUTION: Please consult with the institution's Environmental Health and Safety guidelines for the safe location of the manual plunger and recommended operations.
2. Prior to grid preparation, turn on the humidifier in the cold room to ensure the RH of the cold room is ≥ 95 %.
   NOTE: Grid preparation in low humidity can result in dehydration of thin films, alteration of buffer components due to evaporation, and a decrease in grid-to-grid reproducibility[46]. It is not recommended to freeze grids at <80 % RH.
3. Ensure the temperature of the cold room is at 4 °C.
4. Locate the manual plunger away from strong air currents (i.e., away from air conditioning unit vents) as they can lead to turbulence near grids and/or prominent ice accumulation on cold surfaces.

II. Prepare plunging materials and accessories

NOTE: Estimated operating time: 1-5 minutes

1. Use clean scissors to cut blotting paper circles into 1-1.5 cm wide and ~9 cm long strips. Avoid touching the center of the blotting paper and discard the smaller end pieces. It is important to ensure that the blotting paper strips are dry, clean, and free of contaminants. Separate the strips and place them in a 100 mm Petri dish.
2. Place a 22x22 mm square glass coverslip into a separate 60 mm glass Petri dish. This coverslip-containing glass Petri dish will be used to store, transfer, and glow-discharge

grids.

NOTE: It is recommended to use an air-duster can to remove any visible debris from the slide prior to adding grids. An anti-static gun can also be used to remove any static electricity that accumulates.

3. Assemble and label grid storage boxes.
4. Acquire 4 to 6 clean and dry clamping tweezers and locate them to the manual plunger. Visually inspect each tweezer prior to plunging to ensure they are not damaged and are free of contaminants.

III. Prepare the cryogen dewar and manual plunger

NOTE: Estimated operating time: 5-15 minutes

1. Install the platform base at the bottom of the plunging dewar. Place the ethane vessel dewar on top of the platform base, add the brass ethane vessel, and then install the spinning grid storage platform.
    1. Once liquid nitrogen (LN_2) is added to the plunging dewar, the height of the platform base can no longer be adjusted. Ensure that the grid base is installed properly and is level to limit grid and/or tweezer damage due to improper plunger height.
2. Prior to freezing, check the manual plunger and all ancillary equipment to ensure they are functioning properly to limit sample and/or grid loss.
3. Prior to each freezing session, replace the tape on the manual plunger arm used to hold the tweezers. The high humidity of the room can deteriorate the tape adhesive and decrease the ability of the tape to hold the tweezers, increasing the likelihood of tweezer damage and/or grid loss.

4. Adjust the lamp(s) near the manual plunger to ensure there is sufficient light to monitor sample wicking and ensure grid transfer is easily visualized to prevent grid damage and/or loss (see step 3.7). Use a ring lamp directly behind the plunger to visualize liquid movement and a flexible arm task light near the dewar to illuminate the frozen grids.
5. Adjust the foot pedal tension to ensure the dewar plunging arm is securely retained in place while in the raised position and is fully released when the pedal is depressed. Perform several "dry" runs prior to sample application to ensure the plunger is working properly.

   NOTE: Improper adjustment of the foot pedal tension will result in premature release of the plunging arm (i.e., tension is set too low) and grid loss or incomplete plunging of the grid into the ethane vessel (i.e., the tension is set too high).
6. Place the plunging dewar at the base of the manual plunger directly below the plunging arm and secure it in place. Attach a pair of tweezers to the plunging arm using the attached tape. While holding the manual plunging arm, depress the foot pedal to *carefully* lower the plunging arm and adjust the travel of the plunging arm to ensure the grid will locate within the middle of the ethane vessel.
7. Use the bump stop at the top of the plunging arm to determine the final position of the plunging arm when the foot pedal is fully depressed (**Figure 1B**). Adjust the bump stop height on the plunging arm to adjust the location of the grid in the ethane vessel (**Figure 1C**).

   NOTE: Improperly setting the plunging arm height can lead to the grid and/or tweezer damage (e.g., plunging arm height is set too low) or inadequate vitrification (e.g., plunging arm height is set too high).
8. Locate the dewar outside the cold room and proceed to preparing liquid ethane (step 4).

IV. Prepare the cryogen

NOTE: Estimated operating time: 10-30 minutes

1. Assess the ethane tank, regulator, tubing, and ethane dispensing tip for any signs of damage. Immediately report and rectify any signs of damage before proceeding. CAUTION: Compressed ethane and ethane:propane gas mixes are flammable and can pose a serious threat to life and/or result in injury if improperly handled. Please consult an expert if unsure how to operate or handle compressed gas tanks. Please refer to the institution's Environmental Health and Safety guidelines when handling flammable compressed gases. In addition, liquified ethane is a powerful cryogen that can pose a serious threat to life and/or injury if not handled properly. Please refer to the institution's Environmental Health and Safety guidelines when handling cryogens.
2. Acquire sufficient LN_2 in an appropriate LN_2 handling dewar (i.e., 3-4 L is typical for grid preparation and storage). CAUTION: LN_2 is a cryogen that can pose a serious threat to life and/or injury if not handled properly.
    1. Ensure all personal protective equipment are utilized to minimize the risk of injury. The vapor of LN_2 is an asphyxiant and should be handled in well-ventilated areas. Please consult an expert if unsure how to operate or handle cryogenic vessels and cryogens. Please refer to the institution's Environmental Health and Safety guidelines when handling cryogens. For situations in which liquid nitrogen cannot be used in a cold room, we recommend plunge freezing in a cool and well-ventilated space.

3. Outside of the cold room, cool down the plunging dewar by pouring LN_2 directly into the brass ethane vessel until the liquid nitrogen level reaches the top of the ethane vessel (i.e., just above the platform). Top off the LN_2 outside the ethane vessel as needed. Proceed to the next step when the LN_2 stops bubbling violently (approximately 5 minutes).
    1. Add LN_2 directly to the brass ethane vessel to sufficiently cool the vessel prior to condensing ethane gas. Failure to properly cool the brass ethane vessel will dramatically increase the time it takes to condense ethane.
    2. Once the dewar has reached LN_2 temperature, avoid overfilling the dewar such that LN_2 spills into the ethane vessel.
4. Ethane comes as a compressed gas and needs to be liquefied for use. The ethane tank utilizes a high-purity dual-stage regulator to control the gas flow. Connect tubing to the regulator outlet valve and use a 14-gauge flat metal dispensing tip connected at the end for dispensing ethane.
5. Prior to opening the ethane main tank valve, make sure the pressure adjusting knob and outlet valve are closed all the way. Fully open the main tank valve and then open the outlet valve to ~50%. Slowly open the pressure adjusting knob until a slow gas flow is observed. Use the outlet valve to fine-tune the gas flow. CAUTION: Always point the metal dispensing tip away from self when opening valves or making gas flow adjustments.
6. Slowly start the gas flow and assess the flow rate by inserting the tip of the ethane gas line into a small beaker of deionized water. Adjust the gas flow until the flow rate *moderately* disturbs the water.

    1. Adjust the gas flow rate to ensure proper ethane condensing occurs - too slow of a flow rate will cause the ethane gas to solidify in the dispensing tip and too fast of a flow rate will result in intense bubbling and prevent freezing.
7. Prior to inserting the tip of the ethane gas line into the brass ethane vessel, clean and wipe the dispensing tip with delicate task wipes to remove any water.
8. In a smooth and quick motion, locate the gas dispensing tip at the bottom of the brass ethane vessel and begin moving the dispensing tip in a slow circle around the bottom of the ethane vessel. Solid ethane will form immediately but will quickly liquefy as more ethane gas is added/condensed.
    1. Continue to move the metal ethane dispensing tip around at the bottom of the ethane vessel to liquefy the solid ethane. Fill up the ethane vessel to ¾ full of liquid ethane (2-3 threads from the top). Stop ethane gas flow by carefully removing the metal ethane dispensing tip from the brass ethane vessel and closing the outlet valve.
9. Top off the plunging dewar with LN_2 pouring gently on the side of the dewar to avoid LN_2 addition to the brass ethane vessel, until the liquid level just touches the brass ethane vessel. Place the foam lid on the plunging dewar to facilitate ethane solidification.
    1. LN_2 must directly contact the brass ethane vessel to aid in the solidification of ethane. After approximately 5 minutes, the ethane within the brass vessel will become completely frozen solid. Add more LN_2 until it just touches the ethane vessel and proceed to the next step.
10. If the ethane has not frozen solid, then the brass ethane vessel is not cold enough for the remaining steps. Add more LN_2 until it just touches the ethane vessel and wait an additional 5 minutes. Ensure that the ethane within the brass vessel is completely frozen solid.

11. Open the gas outlet valve to produce an ethane gas flow at a similar rate as determined in step 4.6. Vertically place the metal ethane dispensing tip into the solid ethane and continue to move the ethane dispensing tip in a circular motion to melt the solid ethane.
    1. Continue to add ethane until it is level with the top of the brass ethane vessel. Slowly remove the tip from the ethane vessel and close the ethane tank outlet valve. Cover the dewar with the lid for ~1-4 minute(s) to let the ethane solidify around the edges of the brass ethane vessel.
    NOTE: An ideal ethane vessel will have a 2-3 mm symmetric ring of solid ethane at the perimeter of the brass ethane vessel with liquid ethane in the center (**Figure 1D** and **Figure 2**).
    2. Ensure that the ethane be as cold as possible without solidifying to ensure proper vitrification of the biological specimen. Failure to properly prepare the liquid ethane can result in inadequate vitrification of the specimen, ice accumulation, and/or loss of specimen, each contributing to the deterioration of specimen quality for imaging.
    3. If a solid ring of ethane does not form after 2-3 minutes, add more LN_2 to the dewar and cover for 2-5 more minutes.
    4. If the ethane is solidifying too quickly, then use a large pair of clean tweezers to gently warm the ethane vessel and/or solid ethane to prevent complete ethane solidification. Once the ethane and LN_2 are stable, close all the ethane tank valves and locate the plunging dewar to the manual plunger. Secure the plunging dewar to the manual plunger.
    CAUTION: Be extra careful when transferring the dewar as LN_2 can spill into the

ethane vessel and solidify the liquid ethane. If need be, a clean set of tweezers can be used to melt any solid ethane in the middle of the vessel.

12. Test the location of the ethane dewar with a pair of empty tweezers to ensure the tweezer tip locates at the center of the ethane vessel and there is sufficient space for the grid and tweezer tip inside the liquid ethane (**Figure 1D**).
    1. If the solid ethane ring is too thick for easy grid handling, then use a pair of room temperature, clean tweezers to melt the solid ethane and create more freezing area at the center of the ethane vessel.

V. Prepare EM grids

NOTE: Estimated operating time: 1-5 minutes

1. Add the grid storage box(es) to the dewar, unscrew the grid storage box lid(s), and make sure each lid can freely rotate to a new grid slot.
2. Carefully transfer grids from the grid storage box to the edge of the square glass coverslip with ~30-40% of the grid off the slide edge. Ensure that the grid foil is facing up. Ensure grids are covered when not in use. Placing the grids over the edge of the square glass coverslip provides ease of grid handling and decreases the chance of bending or damaging the grid during transfer.
   NOTE: 4-6 grids are typically prepared at a time.
3. Render grids hydrophilic using a glow discharger or plasma cleaner.
   NOTE: Please refer to the recommended guidelines for grid cleaning provided by the glow discharger/plasma cleaner manufacturer.
    1. Use the grids within 10 minutes of plasma cleaning as the grids lose hydrophilicity and grid-to-grid reproducibility decreases after this time.

VI. Prepare cryoEM specimen by plunge freezing

NOTE: Estimated operating time: >10 minutes (~1-3 min per grid)

1. Use a clean and dry clamping tweezer to pick up a cleaned grid, slide the plastic clamp down to fix the grid in place, and gently tap the tweezers to ensure the grid is properly secured.
    1. Handle grids by the outer ring to prevent damage to the grid foil.
2. Apply 1 to 5 µL of sample to the prepared side (e.g., front or foil side) of the grid. NOTE: The optimal volume and blotting time depends on the sample and needs to be optimized for each sample; larger volumes and more viscous samples require longer blotting times.
3. Secure the tweezer-grid-sample assembly to the manual plunging arm by wrapping tape around the tweezer handle.
    1. Face the sample towards the user for traditional front blotting. If the sample requires back blotting, then locate the sample away from the user.
4. Hold a clean, dry, cut piece of blotting paper between the thumb and index finger of each hand.
    1. Only handle the blotting papers from the edges and never touch the center as oils and other contaminants from hands/gloves can alter grid quality.
5. Rest hands on the edge of the plunging dewar to establish a stable position. Locate the blotting paper parallel to the grid surface approximately 1 cm away from the grid surface.
    1. Use the middle section of the blotting paper to allow for complete fluid mobility and even wicking across the grid surface.

6. Gently slide and rotate the thumb and ring fingers towards each other to bend blotting paper toward the grid to initiate blotting. Maintain contact between the blotting paper and the grid surface during the entire blotting process.
    1. Directly contact the blotting paper to the grid surface and maintain consistent contact across the grid surface.
    2. Gently bending the blotting paper decreases bending of the grid and/or damage to the grid surface, and results in more consistent ice across the grid (**Figure 3A**).
7. Observe the mobile liquid front and once it stops progressing into the blotting paper begin counting for 4 to 6 seconds.
   NOTE: Counting can occur once the blotting paper contacts the grid surface but lower grid-to-grid reproducibility can occur. The total blot time will depend on the grid type, foil type, sample concentration, and sample type (e.g., soluble versus membrane versus filamentous proteins). For more viscous samples longer blot times (e.g.., 5 to 7 seconds) will be required.
    1. Important: Develop a reliable and consistent counting scheme to greatly enhance reproducibility during the freezing process.
8. Move the left, right thumb and index fingers in opposite directions to remove the blotting paper in a "snapping motion" away from the grid surface. Immediately depress the foot pedal to release the plunging arm and plunge the grid into liquid ethane.
    1. Simultaneously remove the blotting paper and press the foot pedal to plunge the grid into the ethane as soon as possible for best freezing results. The longer the time between blotting paper removal and plunging, the more evaporation of thin films will occur and decrease grid-to-grid reproducibility.

9. Use one hand to stabilize the clamping tweezers, unwind tape carefully from around the tweezers and manual plunging arm.
    1. Always maintain contact with the tweezer to prevent movement of the tweezer-grid and limit grid damage that occur from knocking the grid against the solid ethane.
10. Once clamping tweezers are free from the manual plunging arm, maintain the tweezer in one hand resting on top of the plunging dewar, ensure the grid remains in the liquid ethane. Carefully slide the plastic clamp away from the grid so the grid can be transferred. Maintain pressure on the tweezers to retain the grid.
    1. With one swift motion, quickly transfer the grid from the ethane vessel into the LN_2 reservoir. Carefully place the grid in the grid storage box. NOTE: Some ethane may solidify on the grid surface. Opening the tweezer slightly will break the ethane and allow for the grid to be dropped into the grid box.
11. Wrap the tip of the tweezers in a delicate task wipe to prevent frost accumulation. Set aside until the tweezers have returned to room temperature.
    1. Have 4 to 6 tweezers on hand for ease of use. Each tweezer will be used for sample freezing and warmed before subsequent use.
12. Repeat steps 6.1-6.11 for each grid.
13. Once freezing has culminated, securely close the grid box and transfer to a proper storage location.
14. Carefully dispose of the liquid ethane and LN_2 and store all materials in a dry location.

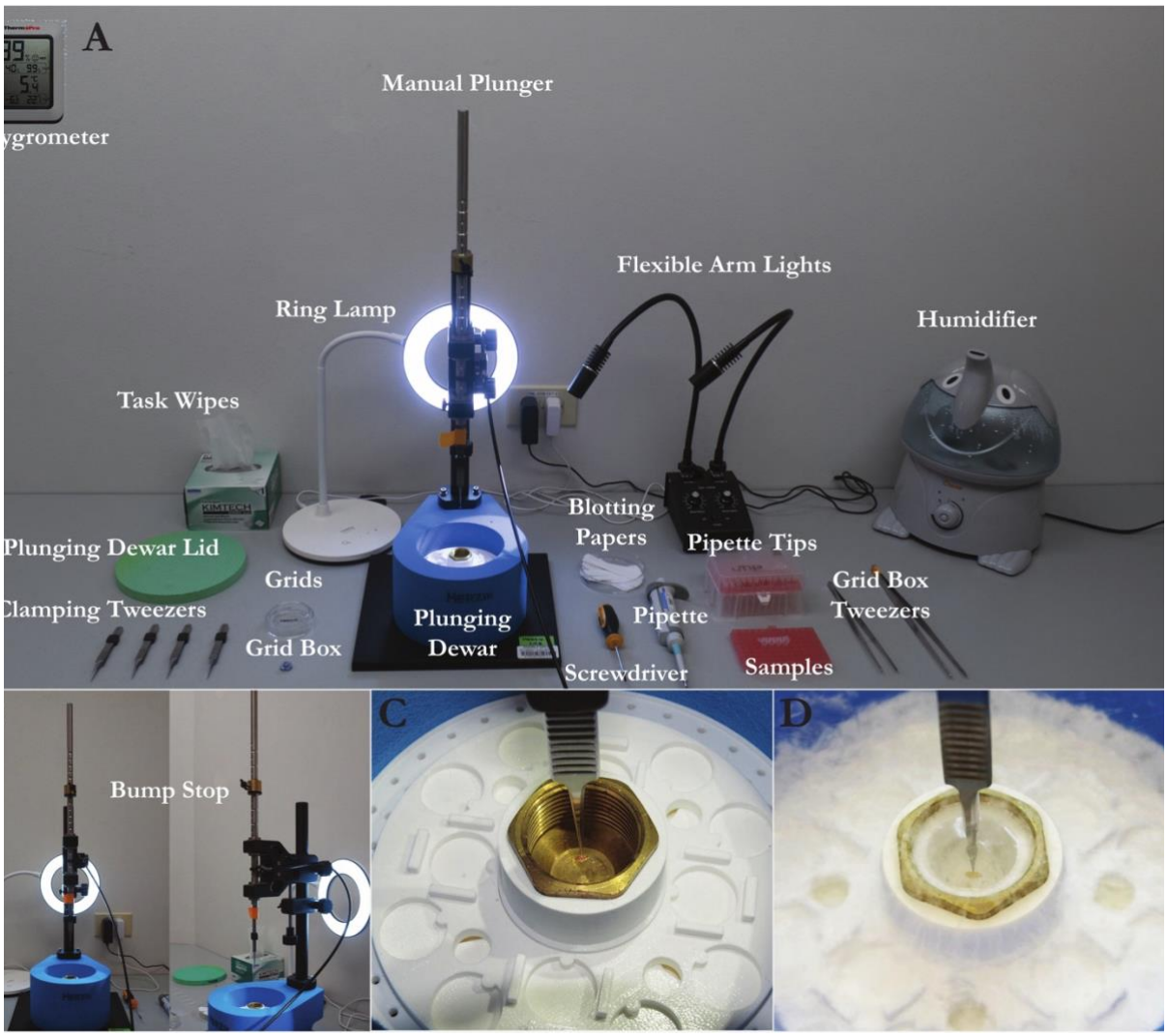


Figure 2.1: Specimen plunging room and required equipment. A) Staged cold room for the manual freezing of biological specimens using a traditional blot-and-plunge device outlined in this article. Necessary equipment is shown and labeled accordingly. **B**) To adjust the working height of the manual plunger, adjust the bump stop by sliding it up and down the manual plunging arm and securing it by tightening the screw. **C**) Zoomed-in view of the ethane vessel and spinning grid storage platform to indicate proper height and location of the clamping tweezers and grid inside the empty brass ethane vessel. The tweezers and grid should not contact the sides or bottom of the brass ethane to avoid damage. **D**) Proper height and location of the clamping tweezers and grid in liquid ethane. The tweezers and grid should enter the liquid ethane in the center, avoiding contact with the solid ethane at the perimeter.

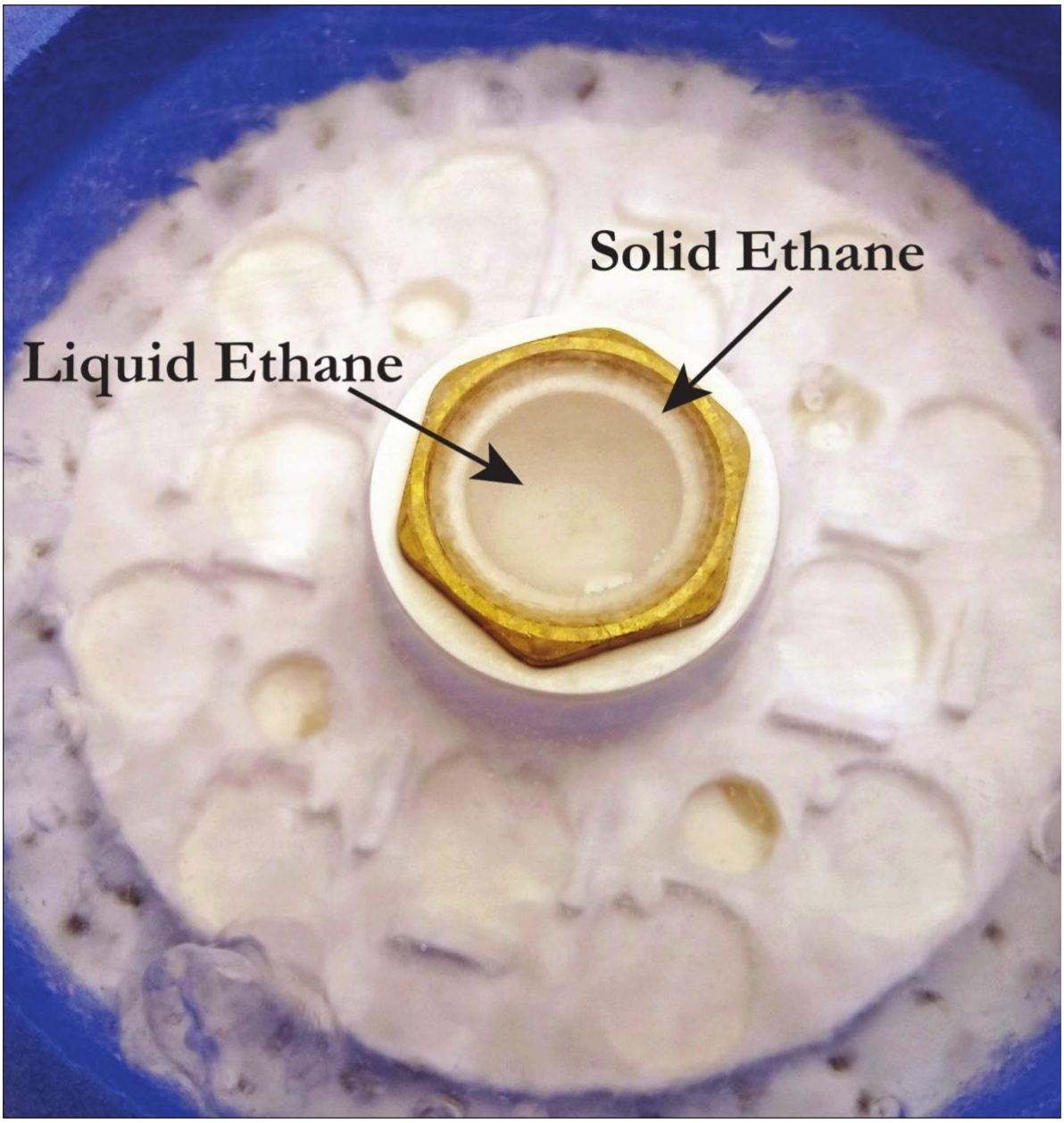


Figure 2.2: Prepared liquid ethane. Zoomed-in view of the plunging dewar showing the state of liquid ethane in the brass ethane vessel prior to specimen freezing. The 2-3 mm ring of solid ethane within the brass ethane vessel is clearly visible.

C. Results

Successful execution of the blot-and-plunge protocol described here will result in a thin, uniform layer of vitreous ice that is free of any hexagonal ice, contaminants, and large gradients of unusable ice which can be observed under the electron microscope (**Figure 3**). Inconsistent contact of the blotting paper with the grid surface, prematurely removing the blotting paper, or moving the blotting paper during grid contact can decrease the quality of the vitreous ice and lead to inconsistent ice thickness across the EM grid (**Figure 4**)

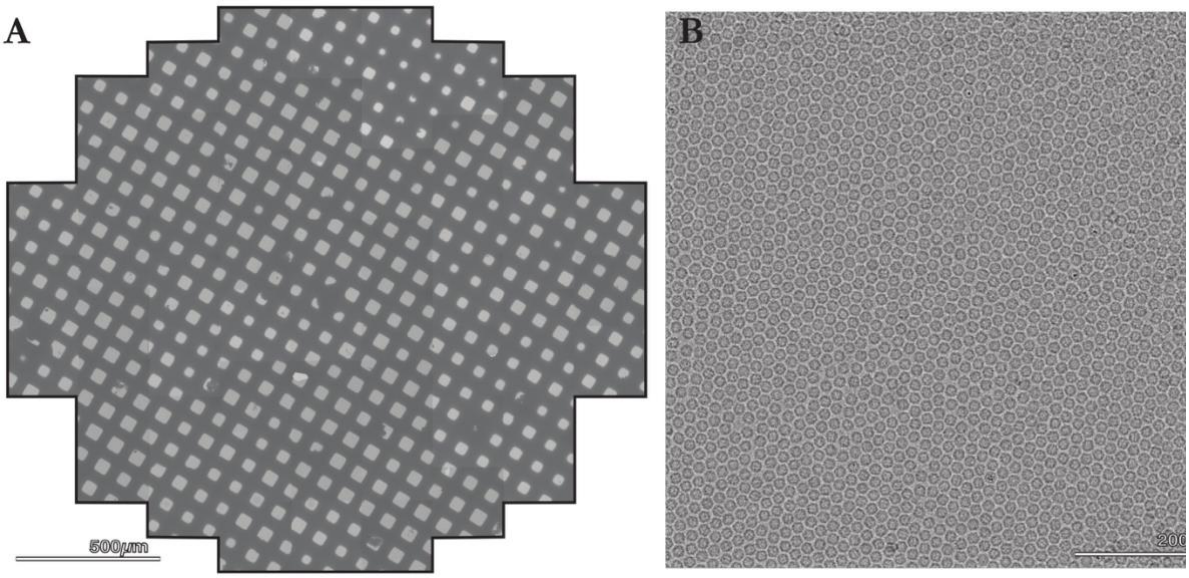


Figure 2.3: Representative apoferritin images obtained using the manual blot-and-plunge technique. (**A**) Representative atlas of a cryoEM grid showing the ice thickness and quality of grid squares that can be obtained using the manual blot-and-plunge technique. (**B**) Motion-corrected micrograph of vitrified mouse apoferritin acquired using a 200 kV transmission electron microscope equipped with a direct electron detector at the University of California, San Diego's CryoEM Facility.



Figure 2.4: Representative atlas of a sub-optimal cryoEM grid showing inconsistent ice thickness across the grid, numerous broken squares, and areas in which the ice is too thick to image the specimen.

D. Discussion

The vitrification of biological specimens for imaging by single-particle cryogenic electron microscopy (cryoEM) remains a critically important step for successful structure determination. The manual blot-and-plunge method described in this protocol represents a cost-effective, reliable, and robust method for quickly freezing biological samples in thin films of vitreous ice for cryoEM imaging. Using the methods outlined in the manuscript, researchers will be able to assemble and operate the manual plunger, prepare cryogen suitable for flash-freezing biological samples, and manually blot-and-plunge EM grids containing biological specimens. While this method is quite robust, care should be taken during critical steps in this procedure to obtain optimal ice thickness and quality for high-resolution imaging. We have outlined several of these critical steps below and provide recommendations on how to troubleshoot these steps.

It is imperative to properly position the manual plunging arm to ensure that the grid locates at the center of the liquid ethane within the brass vessel after plunging. Improper height or position of the plunging arm and/or not securing the tweezers properly will lead to damage to the clamping tweezers, the EM grid, and possibly the manual plunger. As discussed above, we always perform at least one trial run prior to preparing biological specimens to verify that the EM grid will locate to the center of the brass ethane vessel after successful plunging (**Figure 1C**). In addition, we also make minor adjustments to the location of the plunging dewar after each grid freezing to fine-tune grid placement within the ethane vessel (**Figure 1D**).

The proper preparation of the ethane cryogen is critical for obtaining thin films of biological specimens in vitreous ice. We have observed that the presence of a 2-3 mm ring of solid ethane around the inner edge of the brass ethane vessel ensures that the temperature of the liquid ethane is optimal for sample vitrification (**Figure 2**). Indeed, after each grid has been frozen, we monitor the quality of the ethane and make minor adjustments - slightly warming the vessel if too

much ethane has solidified or cooling the ethane if the system has warmed up - as needed. We have found that the edge of a room temperature tweezer is sufficient to liquefy solid ethane while covering the dewar with the foam lid for 1-5 min is enough time to allow the ethane to cool. Importantly, we make these adjustments prior to preparing the grid surface (i.e., plasma cleaning) and applying the sample to the grid as this can introduce another variable to grid preparation that is not reproducible.

Finally, we recommend developing a standardized blot-and-plunge routine - sample application, sample blotting, and blotting time - to increase grid-to-grid reproducibility. Bending the blotting paper towards the EM grid allows for uniform contact of the paper with the grid and produces more consistent ice thickness across the entire grid, resulting in even particle distribution within the grid holes (**Figure 3A** and **Figure B**, respectively). This method of blotting is in contrast to robotic blotting devices that interact with the specimen at an angle that may result in a gradient of ice thickness across the grid. In addition, this bending of the blotting paper also decreases the chance of damaging the EM grid upon contact with the blotting paper by buffering the force being applied by the user. After the desired blotting time, quickly straighten the blotting paper by performing a snapping motion to rapidly move the blotting paper away from the grid surface before plunging to prevent damage to the grid upon release of the manual plunging arm. We have found this blotting method and the snapping motion of the blotting paper, when timed with the simultaneous release of the manual plunging arm via the foot pedal, limits evaporation of the thin film before vitrification and increases grid-to-grid reproducibility.

The manual blot-and-plunge method described here is a robust and reliable method that helps lessen some of the financial burden cryoEM can place on emerging labs. While this method is reproducible, creating high-quality vitreous ice that is suitable for cryoEM relies on the

experience and skill of the individual researcher. Although robotic plungers and other emerging technologies automate several aspects of the freezing process, they are generally limited by how much control they offer to researchers and often incur a high price to purchase and operate. With the method outlined in this protocol, researchers will be able to utilize an affordable and versatile EM grid preparation platform that offers flexibility to optimize the plunging conditions (i.e., blotting paper types, blotting angle, blotting durations, blotting directions, etc.) based on sample types and characteristics.

Chapter II, in full, is a reprint of the material as it appears in Jove, 2022. **HOANG P. M. NGUYEN**, Kelly L. McGuire, Brian D. Cook, Mark A. Herzik, Jr. *Manual Blot-and-Plunge Freezing of Biological Specimens for Single-Particle Cryogenic Electron Microscopy.* The dissertation author was the primary researcher and author of this paper. https://app.jove.com/t/62765/manual-blot-plunge-freezing-biological-specimens-for-single-particle

E. References

1. Hofmann, S., Januliene, D., Mehdipour, A.R., Thomas, C., Stefan, E., Bruchert, S., Kuhn, B.T., Geertsma, E.R., Hummer, G., Tampe, R., Moeller, A. Conformation space of a heterodimeric ABC exporter under turnover conditions. Nature 571, 580–583 (2019).
2. Fica, S. M., Nagai, K. Cryo-Electron Microscopy Snapshots of the Spliceosome: Structural Insights into a Dynamic Ribonucleoprotein Machine. Nature Structural & Molecular Biology. 24 (10), 791-799 (2017).
3. Hirschi, M., Herzik Jr, M., Wie, J., Suo, Y., Borschel, W., Ren, D., Lander, G., Lee, S. Cryo-electron microscopy structure of the lysosomal calcium-permeable channel TRPML3. Nature 550, 411–414 (2017) .
4. Nakane, T., Kotecha, A., Sente, A., McMullan, G., Masiulis, S., Brown, P., Grigoras, I., Malinauskaite, L., Malinauskas, T., Miehling, J., Uchanski, T., Yu, L., Karia, D., Pechnikova, E., Jong, E., Keizer, J., Bischoff, M., McCormack, J., Tiemeeijer, P., Hardwick, S., Chirgadze, D., Murshudov, G., Aricescu, A., Scheres, S. Single-Particle Cryo-EM at Atomic Resolution. Nature. 587 (7832), 152-156 (2020).
5. Li, X., Zheng, S. Q., Egami, K., Agard, D. A., Cheng, Y. Influence of Electron Dose Rate on Electron Counting Images Recorded with the K2 Camera. Journal of Structural Biology. 184 (2), 251-260 (2013).
6. Campbell, M. G., Cheng, A., Brilot, A.F., Moeller, A., Lyumkis, D., Veesler, D., Pan, J., Harrison, S.C., Potter, C.S., Carragher, B., Griorieff, N. Movies of Ice-Embedded Particles Enhance Resolution in Electron Cryo-Microscopy. Structure. 20 (11), 1823-1828 (2012).
7. Brilot, A. F., Chen, J.Z., Cheng, A., Pan, J., Harrison, S.C., Potter, C.S., Carragher, B., Henderson, R., Grigorieff, N. Beam-Induced Motion of Vitrified Specimen on Holey Carbon Film. Journal of Structural Biology. 177 (3), 630-637 (2012).
8. McMullan, G., Faruqi, A.R., Henderson, R., Guerrini, N., Turchetta, R., Jacobs, A., van Hoften, G. Experimental Observation of the Improvement in MTF from Backthinning a CMOS Direct Electron Detector. Ultramicroscopy. 109 (9), 1144-1147 (2009).
9. Feathers, J. R., Spoth, K. A., Fromme, J. C. Experimental evaluation of super-resolution imaging and magnification choice in single-particle cryo-EM. Journal of Structural Biology: X. 5, 100047 (2021).
10. Zheng, S. Q., Palovcak, E., Armache, J., . MotionCor2: Anisotropic Correction of Beam-Induced Motion for Improved Cryo-Electron Microscopy. Nature Methods. 14 (4), 331-332 (2017).
11. Yip, K. M., Fischer, N., Paknia, E., Chari, A., Stark, H. Atomic-Resolution Protein Structure Determination by Cryo-EM. Nature. 587 (7832), 157-161 (2020).
12. Fislage, M., Shkumatov, A. V., Stroobants, A., Efremov, R. G. Assessing the JEOL CRYO ARM 300 for High-Throughput Automated Single-Particle Cryo-EM in a Multiuser Environment. IUCrJ. 7 (4), 707-718 (2020).
13. Zhang, K., Pintilie, G. D., Li, S., Schmid, M. F., Chiu, W. Resolving Individual Atoms of Protein Complex by Cryo-Electron Microscopy. Cell Research. 30 (12), 1136-1139 (2020).
14. Danev, R., Yanagisawa, H., Kikkawa, M. Cryo-Electron Microscopy Methodology: Current Aspects and Future Directions. Trends in Biochemical Sciences. 44 (10), 837-848 (2019).

15. Herzik, M. A. Cryo-Electron Microscopy Reaches Atomic Resolution. Nature. 587 (7832), 39-40 (2020).
16. Cheng, A., Negro, C., Bruhn, J.F., Rice, W.J., Dallakyan, S., Eng, E.T., Waterman, D.G., Potter, C.S., Carragher, B. Leginon: New Features and Applications. Protein Science. 30 (1), 136-150 (2021).
17. Suloway, C., Pilokas, J., Fellman, D.,.., Cheng, A., Guerra, F., Quispe, J., Stagg, S., Potter, C.S., Carragher, B. Automated Molecular Microscopy: The New Leginon System. Journal of Structural Biology. 151 (1), 41-60 (2005).
18. de la Rosa-Trevín, J. M., Quintana, A., Del Cano, L., Zaldivar, A., Foche, I., Gutierrez, J., Gomez-Blanco, J., Burgueat-Castell, J., Cuenca-Alba, J., Abrishami, V., Vargas, J., Oton, J., Sharov, G., Vilas, J.L., Navas, J., Conesa, P., Kazemi, M., Marabini, R., Sorzano, C.o.S., Carazo, J.M. Scipion: A Software Framework toward Integration, Reproducibility and Validation in 3D Electron Microscopy. Journal of Structural Biology. 195 (1), 93-99 (2016).
19. Punjani, A., Rubinstein, J. L., Fleet, D. J., Brubaker, M. A. CryoSPARC: Algorithms for Rapid Unsupervised Cryo-EM Structure Determination. Nature Methods. 14 (3), 290-296 (2017).
20. Danev, R., Tegunov, D., Baumeister, W. Using the Volta Phase Plate with Defocus for Cryo-EM Single Particle Analysis. eLife. 6, 23006 (2017).
21. Naydenova, K., Jia, P., Russo, C. J. Cryo-EM with Sub-1 Å Specimen Movement. Science. 370 (6513), 223-226 (2020).
22. Watson, Z. L., Ward, F.R., Meheust, R., Ad, O., Schepartz, A., Banfield, J.F., Cate, J.H. Structure of the Bacterial Ribosome at 2 Å Resolution. eLife. 9, 60482 (2020).
23. Josephs, T. M., Belousoff, M.J., Liang, Y., Piper, S.J., Cao, J., Garama, D.J., Leach, K., Gregory, K.J., Christopoulos, A., Hay, D.L., Danev, R., Wooten, D., Sexton, P.M. Structure and Dynamics of the CGRP Receptor in Apo and Peptide-Bound Forms. Science. 372 (6538), (2021).
24. Tan, Y. Z., Baldwin P.R., Davis, J.H., Williamson, J.R., Potter, C.S., Carragher, B., Lymkis, D. Addressing Preferred Specimen Orientation in Single-Particle Cryo-EM through Tilting. Nature Methods. 14 (8), 793-796 (2017).
25. D'Imprima, E., Floris, D., Joppe, M., Sánchez, R., Grininger, M., Kühlbrandt, W. Protein Denaturation at the Air-Water Interface and How to Prevent It. eLife. 8, 42747 (2019).
26. Han, Y., Fan, X., Wang, H., Zhao, F., Tully, C.G., Kong, J., Yao, N., Yan, N. High-Yield Monolayer Graphene Grids for near-Atomic Resolution Cryoelectron Microscopy. Proceedings of the National Academy of Sciences of the United States of America. 117 (2), 1009-1014 (2020).
27. Dandey, V. P., Budell, W.C., Wei, H., Bobe, D., Maruthi, K., Kopylov, M., Eng, E.T., Kahn, P.A., Hinshaw, J.E., Kundu, N., Nimingean, C.M., Fan, C., Sukomon, N., Darst, S.A., Saecker, R.M., Chen, J., Malone, B., Potter, C.S., Carragher, B. Time-Resolved Cryo-EM Using Spotiton. Nature Methods. 17 (9), 897-900 (2020).
28. McDowall, A. W., Chang, J.J., Freeman, R., Lepault, J., Walter, C.A., Dubochet, J. Electron Microscopy of Frozen Hydrated Sections of Vitreous Ice and Vitrified Biological Samples. Journal of Microscopy. 131 (1), 1-9 (1983).
29. Dubochet, J., McDowall, A. W. Vitrification of pure water for electron microscopy. Journal of Microscopy. 124 (3), 3-4 (1981).

30. Dubochet, J., McDowall, A. W., Menge, B., Schmid, E. N., Lickfeld, K. G. Electron Microscopy of Frozen-Hydrated Bacteria. Journal of Bacteriology. 155 (1), 381-390 (1983).
31. Depelteau, J. S., Koning, G., Yang, W., Briegel, A. An Economical, Portable Manual Cryogenic Plunge Freezer for the Preparation of Vitrified Biological Samples for Cryogenic Electron Microscopy. Microscopy and Microanalysis. 26 (3), 413-418 (2020).
32. Dobro, M. J., Melanson, L. A., Jensen, G. J., McDowall, A. W. Plunge Freezing for Electron Cryomicroscopy. Methods in Enzymology. 481, 63-82 (2010).
33. Cavalier, A., Spehner, D., Humbel, B. M. Handbook of Cryo-Preparation Methods for Electron Microscopy. Microscopy and Microanalysis. 15 (5), 469-470 (2009).
34. Grassucci, R. A., Taylor, D. J., Frank, J. Preparation of Macromolecular Complexes for Cryo-Electron Microscopy. Nat. Protoc. 2 (12), 3239-3246 (2007).
35. Carragher, B., Cheng, Y., Frost, A., Glaeser, R.M., Lander, G.C., Nogales, E., Wang, H. Current Outcomes When Optimizing 'Standard' Sample Preparation for Single-particle Cryo-EM. Journal of Microscopy. 276 (1), 39-45 (2019).
36. Noble, A. J., Dandey, V.P., Wei, H., Brasch, J., Chase, J., Acharya, P., Tan, Y.Z., Zheng, Z., Kim, L.Y., Scapin, G., Rapp, M., Eng, E.T., Rice, W.J., Cheng, A., Negro, C.J., Shapiro, L., Kwong, P.D., Jeruzalmi, D., Georges, A.d., Potter, C.S., Carragher, B. Routine Single Particle CryoEM Sample and Grid Characterization by Tomography. eLife. 7, 34257 (2018).
37. Resch, G. P., Brandstetter, M., Konigsmaier, L., Urban, E., Pickl-Herk, A. M. Immersion Freezing of Suspended Particles and Cells for Cryo-Electron Microscopy. Cold Spring Harbor Protocols. 7, 803-814 (2011).
38. Resch, G. P., Brandstetter, M., Pickl-Herk, A.M., Konigsmaier, L., Wonesch, V.I., Urban, E. Immersion Freezing of Biological Specimens: Rationale, Principles, and Instrumentation. Cold Spring Harbor Protocols. 7, 778-782 (2011).
39. Jain, T., Sheehan, P., Crum, J., Carragher, B., Potter, C. S. Spotiton: A Prototype for an Integrated Inkjet Dispense and Vitrification System for Cryo-TEM. Journal of Structural Biology. 179 (1), 68-75 (2012).
40. Razinkov, I., Dandey, V., Wei, H., Zhang, Z., Melnekoff, D., Rice, W.J., Wigge, C., Potter, C.S., Carragher, B. A New Method for Vitrifying Samples for CryoEM. Journal of Structural Biology. 195 (2), 190-198 (2016).
41. Dandey, V. P., Wei, H., Zhang, Z., Tan, Y.Z., Acharya, P., Eng, E.T., Rice, W.J., Kahn, P.A., potter, C.S., Carragher, B. Spotiton: New Features and Applications. Journal of Structural Biology. 202 (2), 161-169 (2018).
42. Lu, Z., Shaikh, T.R., Barnard, D., Meng, X., Mohamed, H., Yassin, A., Mannella, C.A., Agrawal, R.K., Lu, T., Wagenknecht, T. Monolithic Microfluidic Mixing-Spraying Devices for Time-Resolved Cryo-Electron Microscopy. Journal of Structural Biology. 168 (3), 388-395 (2009).
43. Feng, X., Fu, Z., Kaledhonkar, .S., Jia, Y., Shah, B., Jin, A., Liu, Z., Sun, M., Chen, B., Grassucci, R.A., Ren, Y., Jiang, H., Frank, J., Lin, Q. A Fast and Effective Microfluidic Spraying-Plunging Method for High-Resolution Single-Particle Cryo-EM. Structure. 25 (4), 663-670 (2017).
44. Rubinstein, J. L., Guo, H., Ripstein, Z.A., Haydaroglu, A., Au, A., Yip, C.M., Di Trani, J.M., Benlekbir, S., Kwok, T. Shake-It-off: A Simple Ultrasonic Cryo-EM Specimen-Preparation Device. Acta Crystallographica Section D. 75 (12), 1063-1070 (2019).

45. Lawson, C. L., Baker, M.L., Best, C., Bi, C. Dougherty, M., Feng, P., van Ginkel, G., Devkota, B., Lagerstedt, I., Ludtke, S.J., Newman, R.H., Oldfield, T.J., Rees, I., Sahni, G., Sala, R., Velankar, S., Warren, J., Westbrook, J.D., Henrick, K., Kleywegt, GJ., Berman, H.M., Chiu, W. EMDataBank.Org: Unified Data Resource for CryoEM. Nucleic Acids Res. 39, 456-464 (2011).
46. Frederik, P. M., Hubert, D. H. Cryoelectron Microscopy of Liposomes. Methods in Enzymology. 391, 431-448 (2005).
47. Dambacher, C. M., Worden, E. J., Herzik, M. A., Martin, A., Lander, G. C. Atomic Structure of the 26S Proteasome Lid Reveals the Mechanism of Deubiquitinase Inhibition. eLife. 5, 13027 (2016).
48. Zubcevic, L., Herzik Jr, M.A., Wu, M., Borschel, W.F., Hirschi, M., Song, A.S., Lander, G.C., Lee, S. Conformational Ensemble of the Human TRPV3 Ion Channel. Nature Communications. 9 (1), 4773 (2018).
49. Zubcevic, L., Herzik, M.A. Jr, Chung, B.C., Liu, Z., Lander, G.C., Lee, S.Y. Cryo-Electron Microscopy Structure of the TRPV2 Ion Channel. Nature Structural & Molecular Biology. 23 (2), 180-186 (2016).
50. Yoo, J., Wu, M., Yin, Y., Herzik, M. A., Lander, G. C., Lee, S. -. Y. Cryo-EM Structure of a Mitochondrial Calcium Uniporter. Science. 361 (6401), 506-511 (2018).
51. Fribourgh, J. L., Srivastava, A., Sandate, C.R., Michael, A.K., Hsu, P.L., Rakers, C., Nguyen, L.T., Torgrimson, M.R., Parico, G.C.G., Tripathi, S., Zheng, N., Lander, G.C., Hirota, T., Tama, F., Partch, C.L. Dynamics at the Serine Loop Underlie Differential Affinity of Cryptochromes for CLOCK:BMAL1 to Control Circadian Timing. eLife. 9, 55275 (2020).
52. Hirschi, M., Lu, W-T., Santiago-Frangos, A., Wilkinson, R., Golden, S.M., Davidson, A.R., Lander, G.C., Wiedenkeft, B. AcrIF9 Tethers Non-Sequence Specific DsDNA to the CRISPR RNA-Guided Surveillance Complex. Nature Communications. 11 (1), 2730 (2020).
53. Herzik, M. A. Manual-Plunging CryoEM Grids | Herzik Lab. Herzik Lab UCSD. , (2021).

Chapter III

Domain organization and conformational dynamics of a p90RSK2:ERK2 complex

A. Introduction

The Ras-mitogen-activated protein kinase (MAPK) pathway is a key regulator of cell proliferation, survival, growth, and motility (Anjum & Blenis, 2008) . Within this signaling cascade, p90 ribosomal S6 kinase (p90RSK) and extracellular signal-regulated kinase (ERK) play pivotal roles. RSK is unique in possessing two distinct kinase domains within a single polypeptide chain: the N-terminal kinase (NTK) from the AGC family and the C-terminal kinase (CTK) from the CAMK family (Anjum & Blenis, 2008; Fisher & Blenis, 1996; Jones et al., 1988) . These domains are flanked by intrinsically disordered regions (IDRs), which play a significant role in kinase regulation (Davey, Cyert, & Moses, 2015; Gógl, Kornev, et al., 2019; P. E. Wright & Dyson, 2015) . This feature is rare among the kinase family, as only a handful of kinases have a double kinase domain. One other example is the JAK kinase family, which contains both a kinase and a pseudokinase domain, where the pseudokinase plays a regulatory role for the kinase domain of JAK. (Devang, Pani, & Rajanikant, 2020; Yamaoka et al., 2004) . The stable interaction between RSK and ERK is unusual for substrate-activator kinase pairs, making it an excellent model for understanding cooperative mechanisms between kinase families. p90RSK has four isoforms that share similar sequence homology, with slightly different functional implications. ERK has five isoforms (Anjum & Blenis, 2008; Lavoie, Gagnon, & Therrien, 2020; Roskoski, 2012) . Here, we focus on p90RSK isoform 2 (RSK2) and ERK isoform 2 (ERK2) (Fig. 1A).

The activation of RSK follows a multi-step, transient process. Initially, ERK1/2 binds to the C-terminal tail of RSK, phosphorylating the CTK activation loop. This event triggers phosphorylation at a conserved hydrophobic motif (HM), creating a docking site for 3-phosphoinositide-dependent protein kinase 1 (PDK1), which subsequently phosphorylates the NTK activation loop. Once activated, NTK phosphorylates downstream substrates with an

RXRXXS/T consensus sequence. Additionally, NTK auto-phosphorylates its C-terminal tail, which may lead to ERK2 dissociation (Fig. 1B) (Anjum & Blenis, 2008) . While the key steps of RSK activation are known, the molecular details of ERK2 coordination in RSK2 activation remain unclear.

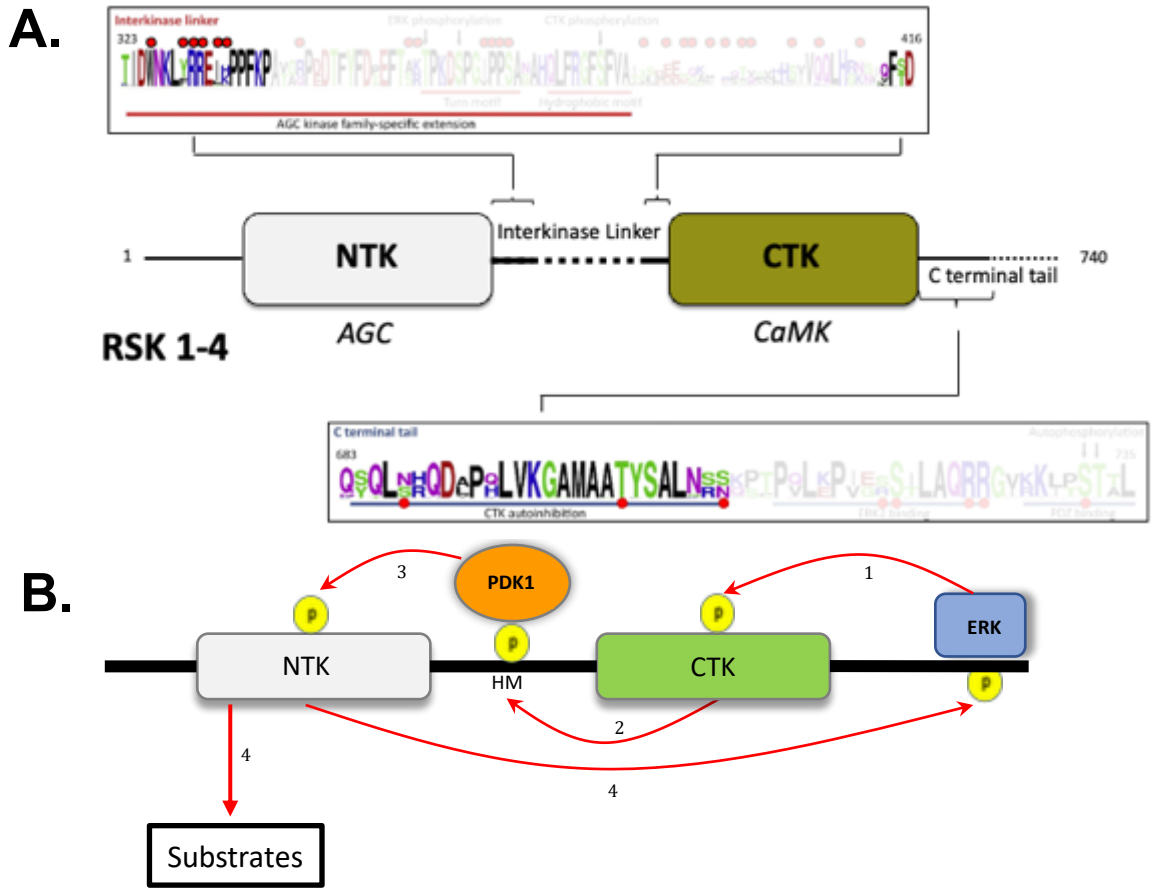


Figure 3.1. p90RSK domain organization and consensus activation mechanism of RSK2 by ERK2 and PDK1. (A) Domain organization of p90RSK2 and conserved important motifs, phosphorylation sites, and cancer mutations (red dots) located in the intrinsically disordered regions of the linker and C-terminal tail. RSK family has 4 different isoforms and two kinase domains from different family: the N-terminal kinase (NTK) from the AGC family and the C-terminal kinase (CTK) from the CAMK family. Dash line represent the missing regions in structures. **(B)** Consensus activation mechanism of p90RSK2 by ERK2 and PDK1. Phosphorylated ERK2 binds to the C-tail of RSK2 and phosphorylates CTK (1). Activated CTK then phosphorylates the hydrophobic motif of the linker between NTK and CTK, providing a docking point for PDK1 (2). Activated PDK1 phosphorylates NTK (3). Fully activated NTK activates downstream substrates or its own C-tail and releases ERK2 (4).

Although obtaining structures of substrate–activator kinase complexes is challenging due to their typically transient nature, several kinase heterodimer pairs have been successfully captured through crystallography. These structures provide valuable insights into how kinases orient themselves to facilitate substrate phosphorylation. For example, the kinase suppressor of Ras 2 (KSR2) and mitogen-activated protein kinase kinase 1 (MEK1) adopt a parallel conformation (with both N-lobes oriented in the same direction). In this configuration, the heterodimer interaction is mediated by their respective activation segments and N-lobe αC-helices (Brennan et al., 2011). Similarly, the crystal structure of the asymmetric homodimer p21-activated kinase 1 (PAK1) suggests a model of trans-autophosphorylation. This model may represent an authentic enzyme–substrate complex in which the homodimer adopts a head-to-head (parallel) conformation. In this arrangement, the activation loop of the putative "substrate" projects into the active site of the "enzyme," and the interaction is stabilized by intermolecular contacts between the αG and αEF helices (Wang, Wu, & Wang, 2011). Additionally, in human checkpoint kinase 2 (Chk2; PDB: 2CN5), Ste20-like kinase (SLK; PDB: 2J51), Ser/Thr kinase 10 (STK10; PDB: 2J7T), and Death-associated protein kinase 3 (DAPK3; PDB: 2J90), when the activation loop sequence does not resemble that of a typical substrate, the homodimer adopts a parallel conformation. In these cases, the activation segment of one protomer intrudes into the active site of the other, forming a configuration known as "activation segment exchange" (Oliver, Knapp, & Pearl, 2007) .

Notably, MAPK signaling specificity appears to be influenced by quaternary structure changes depending on the activation state of upstream kinases (Sok et al., 2020). In the heterodimeric structure of p90RSK1 C-terminal kinase domain (CTK) and ERK2 (PDB: 4NIF), the complex adopts an antiparallel orientation, where the N-lobe of one kinase faces the C-lobe of

the other. The complex is stabilized by two interfaces: Interface 1 involves an interaction between the D-motif located in the C-tail of CTK and the MAPK docking groove of ERK2. Interface 2 is formed by the APE motif—a conserved segment of the CTK activation loop—and the G-loop of ERK2. This interaction properly positions the activation loop of RSK1 within the active site of ERK2. This head-to-tail configuration is maintained in the phosphorylated ERK2–RSK1 complex, providing a mechanism for CTK activation by ERK. (Alexa et al., 2015; Sok et al., 2020)

Interestingly, in the crystal structure of the p38α–MK2 complex, the kinases form a parallel (head-to-head) conformation that creates steric hindrance, preventing MK2's activation loop (AL) from reaching the p38α active site. Upon phosphorylation, however, the complex transitions to an antiparallel (head-to-tail) conformation, enabling p38α to phosphorylate two MK2 sites in solution (Sok et al., 2020; White, Pargellis, Studts, Werneburg, & Farmer, 2007) . This highlights the importance of characterizing kinase complexes and underscores how understanding the quaternary structure of these complexes can shed light on the specificity of kinase signaling pathways.

Additionally, we also utilize a non-catalytic viral peptide, ORF45, from Kaposi's sarcoma-associated herpesvirus (KSHV), to aid in the structural investigation of the RSK2:ERK2 complex. The N-terminal region of ORF45, approximately 88 amino acids in length, has been shown to bind both NTK and ERK with high affinity. Specifically, ORF45 binds ERK with submicromolar affinity (<1 μM) and RSK2 in the nanomolar range, resulting in the persistent activation of both kinases. Crystallography, SAXS, and HDX-MS analyses demonstrate that the ORF45 peptide stabilizes the RSK:ERK complex into a compact conformation and protects key structural elements, including the αG and αH helices of NTK and the αF/APE motif of CTK, from solvent exposure. Therefore, we use this peptide to stabilize the complex in hopes of achieving the highest

possible resolution for structural characterization (Alexa et al., 2022) . Additionally, we included an NTK inhibitor, SL0101, which has been shown to stabilize NTK by increasing its melting temperature, as measured by thermal shift assay (Utepbergenov et al., 2016) . The crystal structure of NTK bound to SL0101 further supports the enhanced stability of this ligand-bound conformation (Utepbergenov et al., 2012) .

Our structural understanding of RSK is limited, with only a few structures resolved. These include NTK structures lacking AGC extension regions, which are crucial for NTK activity, and CTK structures missing the C-terminal tail, essential for CTK regulation. The only available RSK1(CTK) structure in complex with ERK2 provides insights into the early stages of RSK activation (Alexa et al., 2015; Aronchik et al., 2014; Costales et al., 2014; Ikuta et al., 2007; Malakhova et al., 2009, 2008; Utepbergenov et al., 2012) . Despite these insights, structural data on full-length RSK and its complexes remain limited, leaving fundamental questions unanswered - particularly concerning the organization of these three kinases and their precise activation mechanisms.

In this study, we employed a combination of cryo-electron microscopy (cryo-EM) and AlphaFold (AF) modeling to examine the p90RSK2:ERK2 complex. Our study reveals three configurations corresponding to the initial step of ERK2 binding to p90RSK2: configuration 1: the structure of p90RSK2:ERK2, hereafter referred as trimer, configuration 2: the structure of CTK:ERK2, hereafter referred as dimer, configuration 3: the structure of apo ERK2, referred to hereafter as monomer. Additionally, we identify that the PTPL motif located on the C-terminal tail (C-tail) of CTK and the inter-kinase linker between NTK and CTK contribute to CTK and NTK dynamics. Our findings indicate that CTK undergoes rigid-body motion, while NTK is the most mobile of the three domains. Intriguingly, NTK and CTK adopt a parallel (head-to-head)

conformation, whereas CTK and ERK2 assume an antiparallel (head-to-tail) conformation. Furthermore, we propose a structural model illustrating how ERK activates RSK, along with a model depicting how an inhibitor fits into the NTK ATP-binding pocket. Collectively, our findings highlight how domain arrangement and flexible linkers contribute to the complexity of MAPK signaling pathways. These insights suggest that in the inactive state, signaling complexes may exist in multiple conformations, making them more accessible to small-molecule activators and protein partners.

B. Method

Protein purification and complex formation: Proteins were expressed using the E. coli Rosetta pLysS strain containing a pET vector. Full-length human RSK2 and ERK2 were produced following standard expression and purification protocols (Alexa, Gógl et al., 2015; Alexa, Sok et al., 2022). RSK2 was engineered with an N-terminal MBP tag and a C-terminal His tag, with a TEV cleavage site positioned after the MBP tag. To generate an inactive form of His-tagged ERK2, coexpression with lambda phosphatase was used. Additionally, human ORF45 (residues 16-76) was expressed with an N-terminal GST tag. After transformation, cells were grown in LB media at 37°C until reaching an OD of 1, at which point the temperature was reduced to 18°C and IPTG was added (final concentration: 0.1 mM). Expression continued overnight, followed by harvesting and freezing of cell pellets.

For RSK2 purification, cells were lysed using a microfluidizer, and the clarified lysate was loaded onto Ni affinity resin. The column was washed before elution with 250 mM imidazole. The Ni-eluted fraction was further purified using amylose resin, followed by elution with 10 mM maltose. To remove the MBP tag, the sample was treated with TEV protease (1:100 w/w ratio)

and dialyzed overnight. The cleaved tag was separated from RSK2 through anion exchange chromatography using a HiTrap Q column, and the purified protein was concentrated and subjected to size exclusion chromatography (S200 column).

For ERK2 purification, cell pellets were resuspended, lysed with a microfluidizer, and centrifuged to obtain the soluble fraction. The lysate was passed through Ni affinity resin, and the bound protein was eluted and treated with TEV protease overnight to remove the N-terminal His tag. The cleaved ERK2 was further purified using anion exchange chromatography with a HiTrap Q column, allowing separation of the non-phosphorylated (first peak) and dually phosphorylated forms (second peak). The inactive ERK2 (first peak) was further purified via size exclusion chromatography using an S200 column.

For ORF45, cells were lysed and subjected to GST affinity purification. The GST tag was cleaved using TEV protease, and the sample was heated for five minutes to precipitate most contaminating proteins. The remaining soluble fraction was further purified using an S200 gel filtration column.

To assemble the RSK2:ERK2:ORF45 complex, purified RSK2, ERK2, and ORF45 were combined in a 1:1.3:3 molar ratio and subjected to size exclusion chromatography (S200 column) for final purification and analysis.

Crosslinking and inhibitor addition: RSK2:ERK2:ORF45 complexes were further stabilized through chemical crosslinking by incubation with glutaraldehyde. A 5% stock solution of glutaraldehyde was prepared by diluting it in crosslinking buffer (50 mM HEPES, pH 7.5, 150 mM NaCl, 1 mM TCEP). The SL0101 inhibitor was added to the newly formed complex at a final concentration of 100 μM and incubated for 10 minutes. Subsequently, glutaraldehyde was added

to a final concentration of 0.1%, and the crosslinking reaction was initiated. The reaction was quenched by adding 100 mM Tris (pH 8), and the sample was placed on ice. Following crosslinking, the sample was concentrated and applied to an S200 gel filtration column to separate the crosslinked RSK2:ERK2:ORF45 complex from over-crosslinked higher molecular weight artifacts. The purified complex was then concentrated to 0.18 mg/mL, as determined by a Bradford assay, before being flash-frozen on grids for further analysis (Fig. 2).

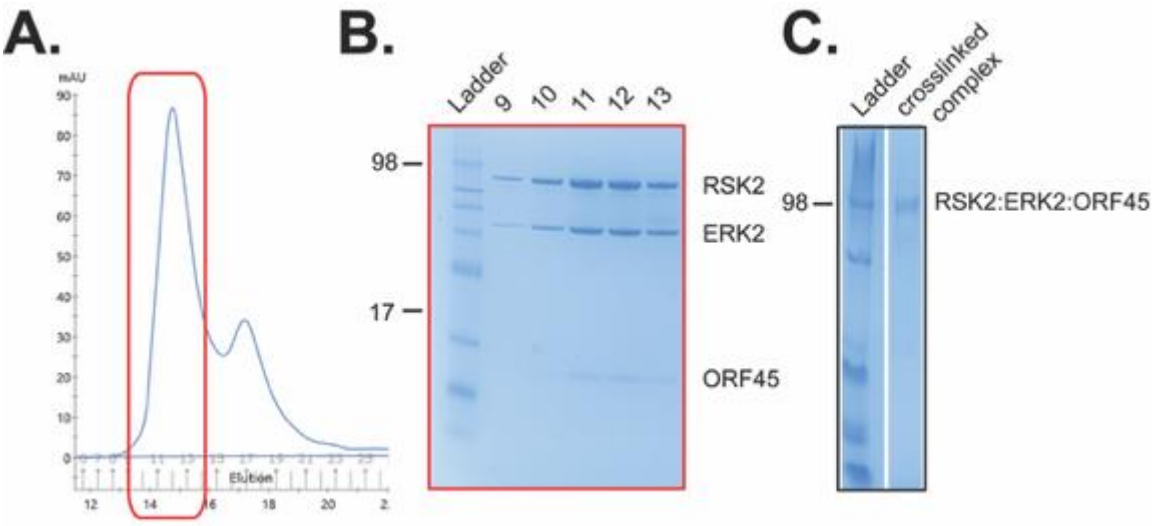


Figure 3.2: **Crosslinked RSK2:ERK2:ORF45 complex formation**. **(A)** Representative gel filtration chromatogram of the RSK2:ERK2:ORF45 complex. **(B)** SDS-PAGE of the complex fractions. **(C)** SDS-PAGE of crosslinked complex. Red box indicates the complex fractions.

CryoEM sample preparation, data collection, and data analysis: Purified inhibitor-added complexes were prepared on UltraAuFoil 1.2/1.3, 300-mesh grids, which were freshly plasma-cleaned using a Gatan Solarus II plasma cleaner (10 s, 15 Watts, 75% Ar/25% O_2 atmosphere). Grid preparation was performed using a custom manual plunge freezer, located in a humidified (>95% relative humidity) cold room (4°C) (Nguyen et al., 2022) . A 3 µL sample was applied to the grid surface, followed by manual blotting for ~6 s using Whatman No. 1 filter paper,

before vitrification in a 50% ethane/50% propane liquid mixture cooled by liquid N_2. Grids were stored under liquid N_2 until data collection.

Data acquisition for the RSK2:ERK2:ORF45 complex was conducted at UCSD's CryoEM Facility using a Titan Krios G3 (Thermo Fisher Scientific) operating at 300 keV, equipped with a Gatan BioContinuum energy filter. Images were collected at 105,000× magnification in EF-TEM mode (0.822 Å calibrated pixel size) on a Gatan K3 detector, using a 20-eV slit width and a cumulative electron exposure of ~60 electrons/Å² (50 frames). Data were automatically collected using EPU, with aberration-free image shift and a defocus range of -0.5 to -2.5 µm.

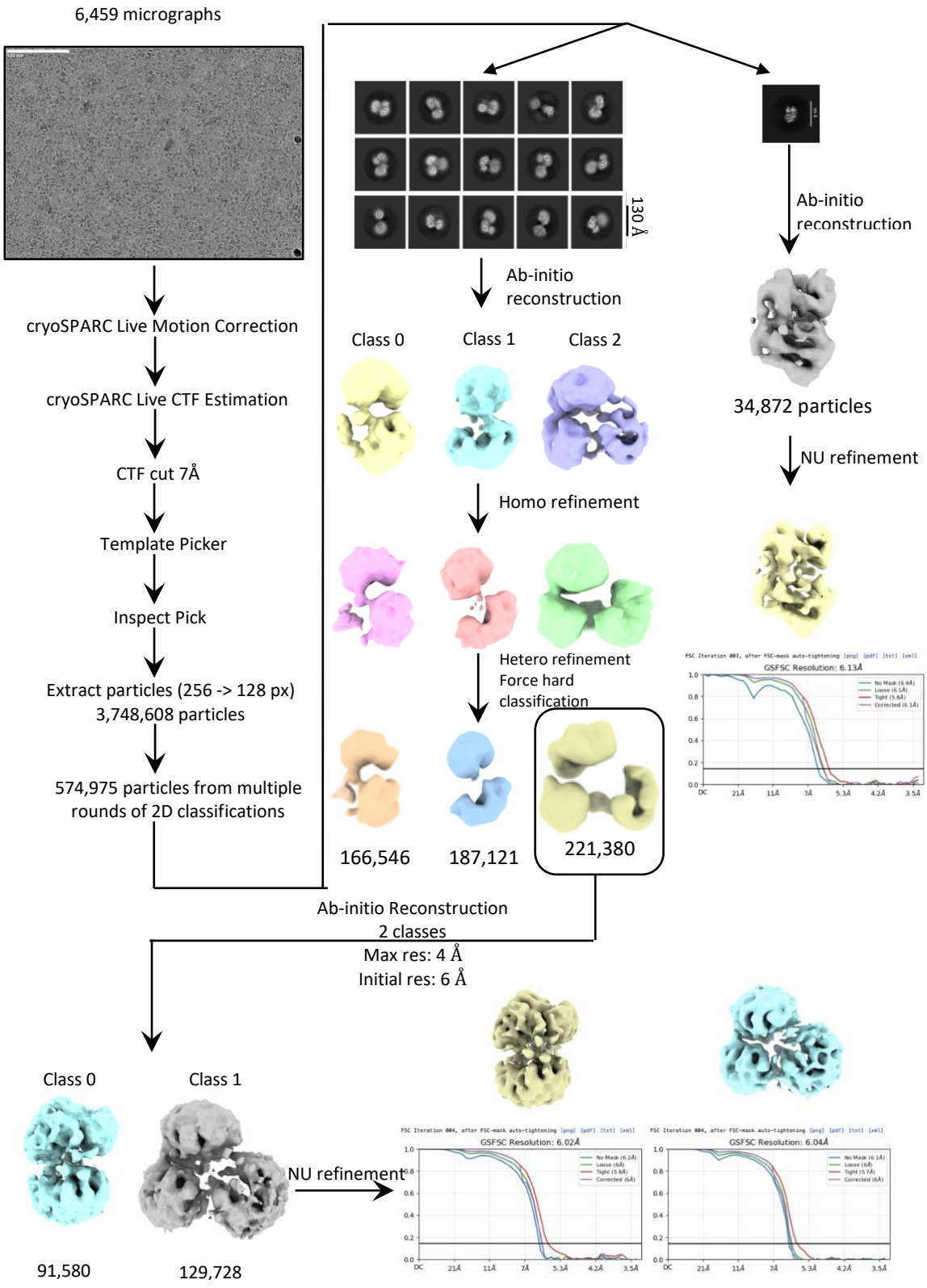
Motion correction and CTF estimation were performed using Live cryoSPARC (Punjani, Rubinstein, Fleet, & Brubaker, 2017). Aligned images with CTF-estimated resolution worse than 7 Å were excluded, and accepted micrographs were imported into cryoSPARC for manual curation. Initial particle picking was conducted using a blob picker (150–180 Å diameter, elliptical blob), and picks were inspected and filtered based on Power Score (-8159 to 566) to remove false picks caused by gold or ice contamination. The selected particles were extracted and binned 2× (256 → 128 px), and a total of 1,005,055 particles underwent ab initio reconstruction with six classes. Among these, Class 0, which displayed a clear three-kinase blob, was selected to generate a template from 50 angles. Template-based particle picking was then performed on manually curated micrographs with modified parameters, including a particle diameter of 130 Å and angular sampling of 1°, resulting in the selection of 5,140,009 particles. These were filtered through an Inspect Picks job to remove false positives, yielding 4,005,973 particles for further processing.

The particles were extracted and binned 2× (256 px → 128 px) before undergoing multiple rounds of 2D classification with optimized parameters: a circular mask diameter of 130 Å, 100 2D classes, 80 online-EM iterations, a batch size per class of 800, and forced max over poses/shifts

set to false. After several rounds of classification, 574,975 particles were selected for ab initio reconstruction into three classes. Each class underwent homogeneous refinement and heterogeneous refinement with forced hard classification. The class exhibiting three lobes was chosen for an additional round of ab initio reconstruction, where resolution constraints of 4–6 Å were applied with two classes, and the resulting outputs were subjected to non-uniform refinement. In parallel, one class displaying an ERK feature was processed through ab initio reconstruction followed by non-uniform refinement.

Ultimately, three distinct structural models were obtained: a monomer at 6.13 Å resolution, a dimer at 6.02 Å resolution, and a trimer at 6.04 Å resolution (Fig. 3).

Figure 3.3: **Single-particle cryo-EM image processing workflow for the crosslinked RSK2:ERK2:ORF45 complex**. Representative micrograph from data set. White scale bar is 100nm.


6,459 micrographs
cryoSPARC Live Motion Correction
cryoSPARC Live CTF Estimation
CTF cut 7Å
Template Picker
Inspect Pick
Extract particles (256 -> 128 px)
3,748,608 particles
574,975 particles from multiple rounds of 2D classifications
130 Å
Ab-initio reconstruction
Class 0
Class 1
Class 2
Homo refinement
Hetero refinement
Force hard classification
166,546
187,121
221,380
Ab-initio reconstruction
34,872 particles
NU refinement
GSFSC Resolution: 6.13Å
Ab-initio Reconstruction
2 classes
Max res: 4 Å
Initial res: 6 Å
Class 0
Class 1
91,580
129,728
NU refinement
GSFSC Resolution: 6.02Å
GSFSC Resolution: 6.04Å

Alpha Fold modeling: AlphaFold 2.3.0 modeling was performed with localcolabfold (Mirdita et al., 2022b) downloaded from https://github.com/YoshitakaMo/localcolabfold on a Dell Alienware desktop machine with an RTX 4090 GPU of 24 Gbytes. We produced 80 models of RSK2:ERK2 with 40 seeds and all AlphaFold v2.3 weight sets without the use of templates from the Protein Data Bank (PDB). Similarly, this was performed for RSK2:ERK2:ORF45 where we produced 40 models with 20 seeds with PDB as template.

Structures were ranked with the default function in Colabfold: 0.8*ipTM + 0.2*pTM. Structures were visualized in PyMOL (v.2.5, Schrödinger, Inc.).

Statistical analysis: For the 2D-level comparison, we used the crystal structure of CTK:ERK2 (PDB: 4NIF), AlphaFold (AF) models of full-length RSK2:ERK2:ORF45 complex (65-740) (excluding the N-terminal 1-64, ERK2 and ORF45), the crystal structures of ERK2 (PDB: 5UMO), CTK (PDB: 2QR8), and NTK (PDB: 3UBD) (Malakhova et al., 2008; Utepbergenov et al., 2012; F. Zhang, Strand, Robbins, Cobb, & Goldsmith, 1994) . All models and crystal structures were simulated into 3Å EM densities using ChimeraX and then imported into cryoSPARC with the same box size as the extracted particles. A Reference-Based Auto-Select 2D job was performed to obtain the Histogram of Ordered Gradients (HOG) and Pearson correlation scores between the 2D class averages contributing to the reported 3D dimer and monomer structures. Statistical analyses were carried out using an in-house Python script. For comparisons involving three datasets, a one-way analysis of variance (ANOVA) followed by Tukey's Honestly Significant Difference (HSD) test was conducted. For pairwise comparisons, the Mann-Whitney U test was used.

C Results

Building on the previous study [HDXMS paper ref], we identified conditions that enhance the potential for achieving higher resolution. To stabilize the p90RSK2:ERK2 complex, we utilized both the NTK inhibitor SL0101 and the small viral peptide ORF45 (Alexa et al., 2022; Utepbergenov et al., 2012, 2016) . The new dataset has produced a map of the p90RSK2:ERK2 complex in three configurations, revealing structural features such as helices and distinct N-lobe and C-lobe regions in some kinase domains (Fig. 4). In Configuration 1, where densities for all three kinases are observed, hereafter referred to as “trimer”, the improved resolution and the clear distinction between the N-lobe and C-lobe in one kinase domain allowed us to confidently assign ERK, NTK, and CTK densities. This was achieved by comparing the mean number of atoms outside the contour across three different fitting approaches. In Model 1, using the RSK2:ERK2:ORF45 model, we fit ERK into the most resolved EM density, aligning the N-lobe of the model with the corresponding EM density. Similarly, in Model 2, CTK was fitted into the most resolved density, while NTK was placed in the most resolved density in Model 3. When we moved the model around and let the software fit the model into EM density, Model 1 exhibited the best fit, with the fewest atoms falling outside the contour (Fig. 4, Fig. 5). In Configuration 2, where densities for 2 kinases domain are observed, hereafter referred to as “dimer”, we observed N-lobe and C-lobe features in one kinase domain, along with helical elements in certain regions (Fig. 6). By comparing the experimental 2D classes contributing to the dimer structure with projections of simulated EM densities from the CTK:ERK2 crystal structure (PDB: 4NIF) and the AlphaFold-predicted RSK2 model, we concluded that the observed dimer represents the CTK:ERK2 complex rather than RSK2. The absence of the NTK in this structure may be due to the flexibility of NTK or its interkinase linker (Fig. 13). Additionally, 2D classes of this dimer structure show significant

movement between the two kinase domains, which partly explains the inability to achieve higher resolution for this dimer structure. In Configuration 3, we observed a monomeric kinase (Fig. 4C). To identify this kinase, we compared local and global correlations between 2D class averages and simulated EM projections of ERK2 (PDB: 5UMO), CTK (PDB: 2QR8), and NTK (PDB: 3UBD). Both the Histogram of Ordered Gradients (HOG) and Pearson correlation scores were highest when comparing the monomer structure to ERK2, suggesting that the monomer represents ERK2 (Fig. 7)

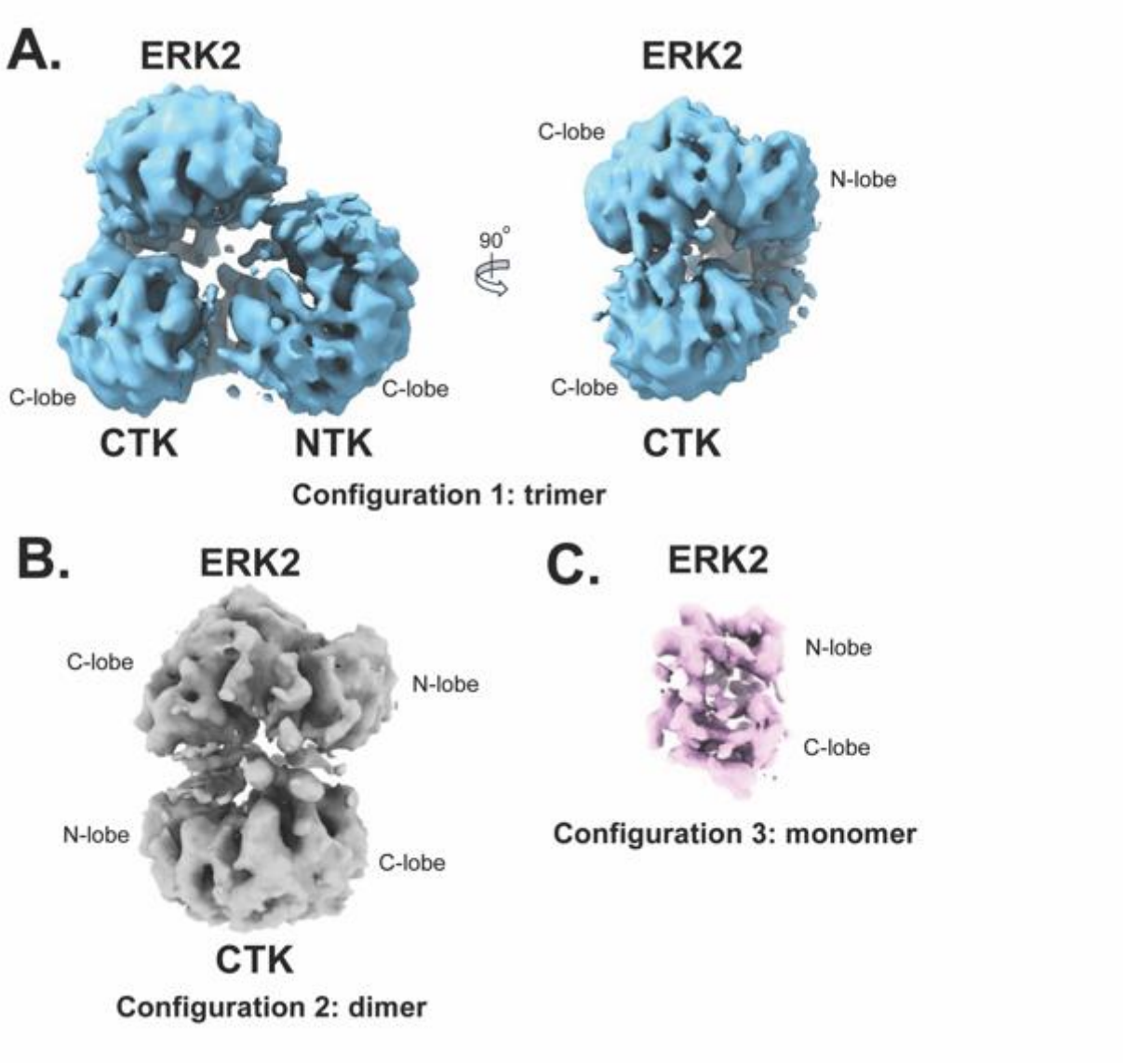


Figure 3.4: **Cryo-EM structure of the RSK2:ERK2:ORF45 complex**. **(A)** Configuration One: In the trimer structure, more detailed density is observed for the three kinase domains, with ERK being the most resolved domain, exhibiting clear N-lobe and C-lobe features. Additionally, crevices and helical features begin to emerge in other regions. The FSC curve indicates that this trimer has a resolution of 6.01 Å. **(B)** Configuration Two: In the dimer structure, NTK is disordered. The weak density on the opposite side of CTK highlights the low occupancy of NTK and the linker. The FSC curve shows that the resolution of this structure is 6.08 Å. **(C)** Configuration Three: In the monomer structure, ERK is the most resolved kinase domain with a resolution of 6.07 Å.

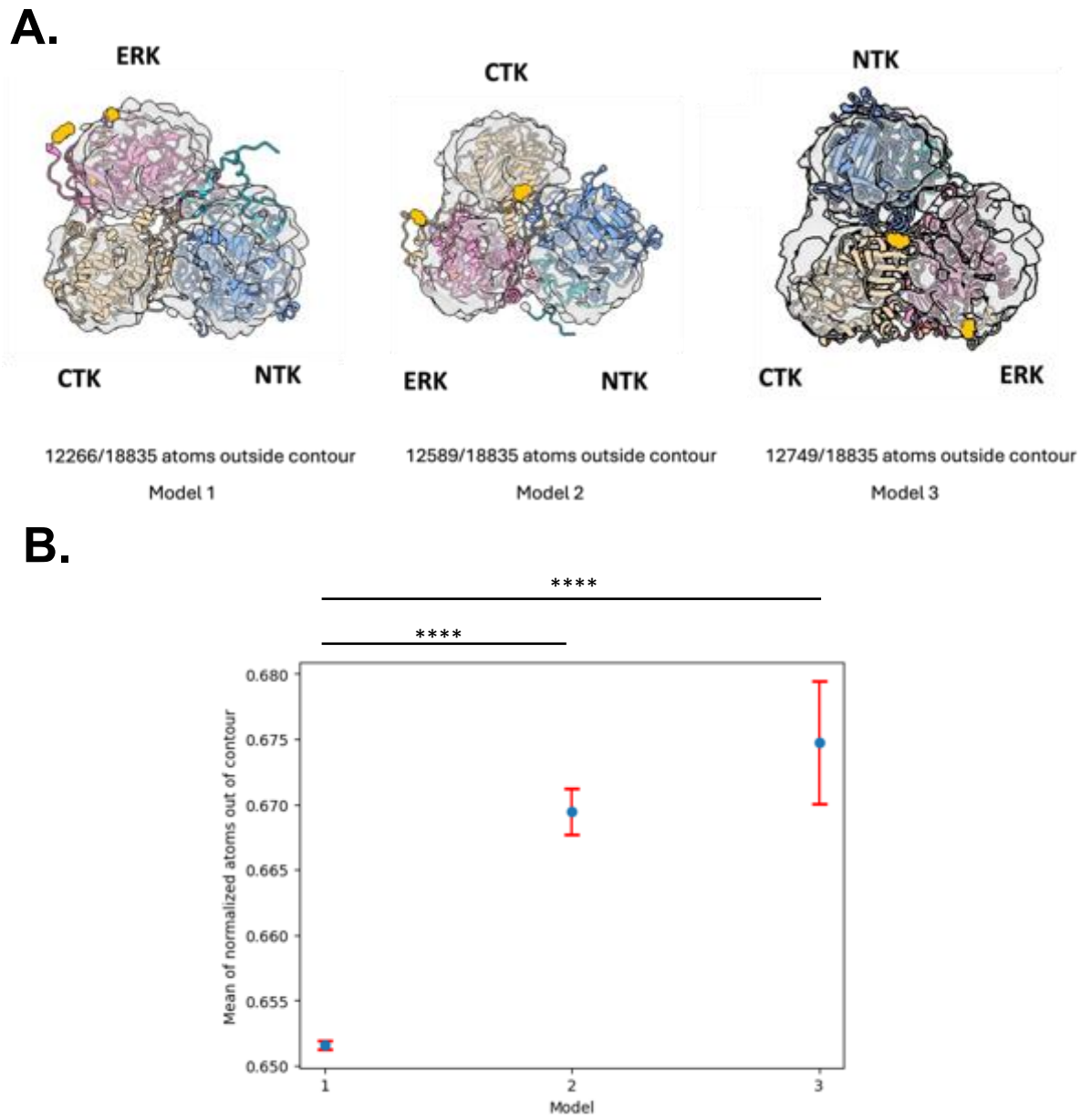


Figure 3.5: **Trimer fit and statistical analysis. (A)** The AF-predicted model was fitted into the EM density in three ways, with the N-lobe and C-lobe of each kinase domain fitting into the most resolved kinase domain density. ERK (magenta), CTK (gold), NTK (blue), and ORF45 (green). **(B)** The number of atoms outside the contours was measured, and a one-way ANOVA followed by Tukey's HSD test revealed significant differences between Model 1 vs. Model 2 and Model 1 vs. Model 3, with Model 1 having the best fit. Adjusted P-values from Tukey's HSD test are indicated as follows: *P < 0.05; **P < 0.01; ***P < 0.005; ****P < 0.001, n=3

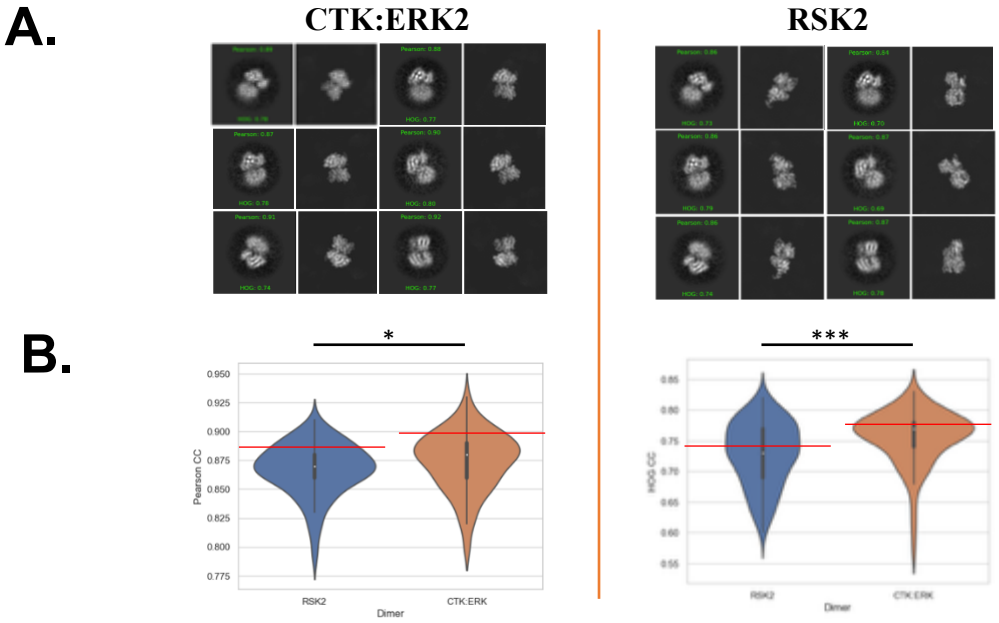


Figure 3.6: **Dimer structure is CTK:ERK2**. **(A)** Shown on the top left is a representative comparison between 2D class averages (highlighted in the column with green numbers) and projections generated from the simulated CTK:ERK2 crystal structure (PDB: 4NIF; column without numbers). The same 2D class averages are also compared with projections of the AlphaFold-predicted model of RSK2 (top right). Visually, the 2D class averages more closely resemble the CTK:ERK2 structure than the RSK2 model. **(B)** Quantitative analysis using Histogram of Ordered Gradients (HOG) and Pearson correlation coefficients confirms that the dimer structure aligns more closely with the CTK:ERK2 complex. The red line indicates the median of correlation scores, which are higher for CTK:ERK2 than for RSK2 in both metrics. Statistical significance was assessed using the Mann-Whitney U test, with p-values indicated as follows: *P < 0.05; **P < 0.01; ***P < 0.005; ****P < 0.001; n = 100.

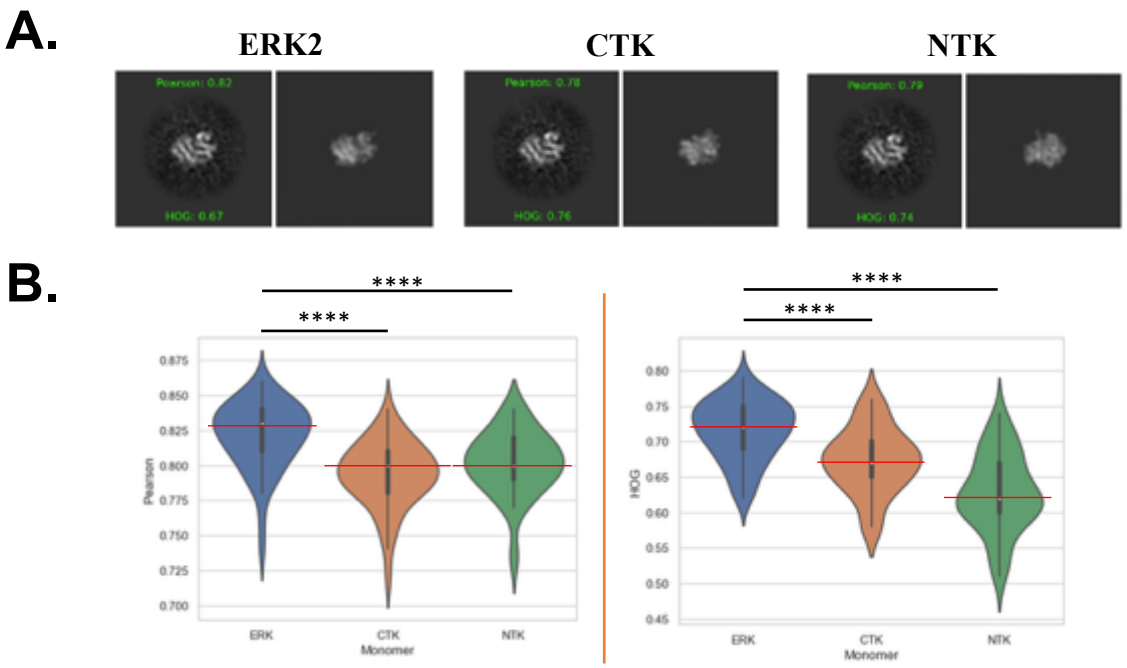


Figure 3.7: **Monomer structure of ERK2**. **(A)** A representative comparison of the 2D class averages (shown in the column with green numbers) versus the projection of the simulated ERK2 crystal structures (PDB: 5UMO), CTK crystal structure (PDB: 2QR8), NTK crystal structure (PDB: 3UBD) (shown in the column without numbers). Visually, 2D class average shares more similarities with ERK2 than with CTK or NTK. **(B)** HOG and Pearson correlation coefficients indicate the monomer structure corresponding to ERK2. A violin plot compares the HOG and Pearson correlation coefficients between ERK2, CTK, and NTK, with the mean (red line) indicating a higher correlation for the ERK2 structure. P-values from a one-way ANOVA followed by Tukey's HSD test reveal significant differences among the three groups. Adjusted P-values from Tukey's HSD test are indicated as follows: *P < 0.05; **P < 0.01; ***P < 0.005; ****P < 0.001; n=100.

To characterize the conformational dynamics of the RSK2:ERK2 complex, with a focus on the rigid body motion between the C-terminal kinase domain of RSK2 (CTK) and ERK2, we performed a comparative structural analysis using the crystal structure of the RSK1(CTK):ERK2 complex (PDB: 4NIF) and an AlphaFold-predicted model of the RSK2:ERK2 complex. Given the high sequence identity between RSK1 and RSK2 (81.28%) and their similar functional roles (Fig. 9), RSK1 serves as a reliable structural proxy for modeling RSK2 motions. Additionally, ERK2 is the most stable of the three kinase domains. It was the second protein kinase to be resolved by crystallography (Canagarajah, Khokhlatchev, Cobb, & Goldsmith, 1997) and is also clearly observed in our cryoEM data. Therefore, when analyzing the conformational dynamics of CTK and NTK, we treat ERK2 as a fixed reference. We observed a relative rigid body motion between the CTK and ERK2, where CTK pivots around a hinge point at leucine 714 in the crystal structure (PDB: 4NIF) and leucine 718 in the AF-predicted model, depending on which structure is considered fixed. (Fig. 8A). This leucine residue is highly conserved across 40 RSK orthologs, indicating its functional significance (Gógl, Kornev, et al., 2019). Additionally, the presence of a proline residue in this region likely contributes to its flexibility, as proline often induces kinks in secondary structures (Fig. 8D). To further support this hypothesis, we analyzed the B-factors of the RSK1 (CTK):ERK2 crystal structure (PDB: 4NIF). The high B-factor values in the SKPTPQL region suggest significant flexibility (Fig. 8B). When comparing the EM density of the dimer with the simulated EM density of the crystal structure, we observed a similar trend: ERK remains stable while CTK exhibits rigid body motion around it (Fig. 8C). Additionally, the missing density of the long αF helix is also consistent with our previous study showing that this helix is flexible [ref HDXMS] (Fig. 10).

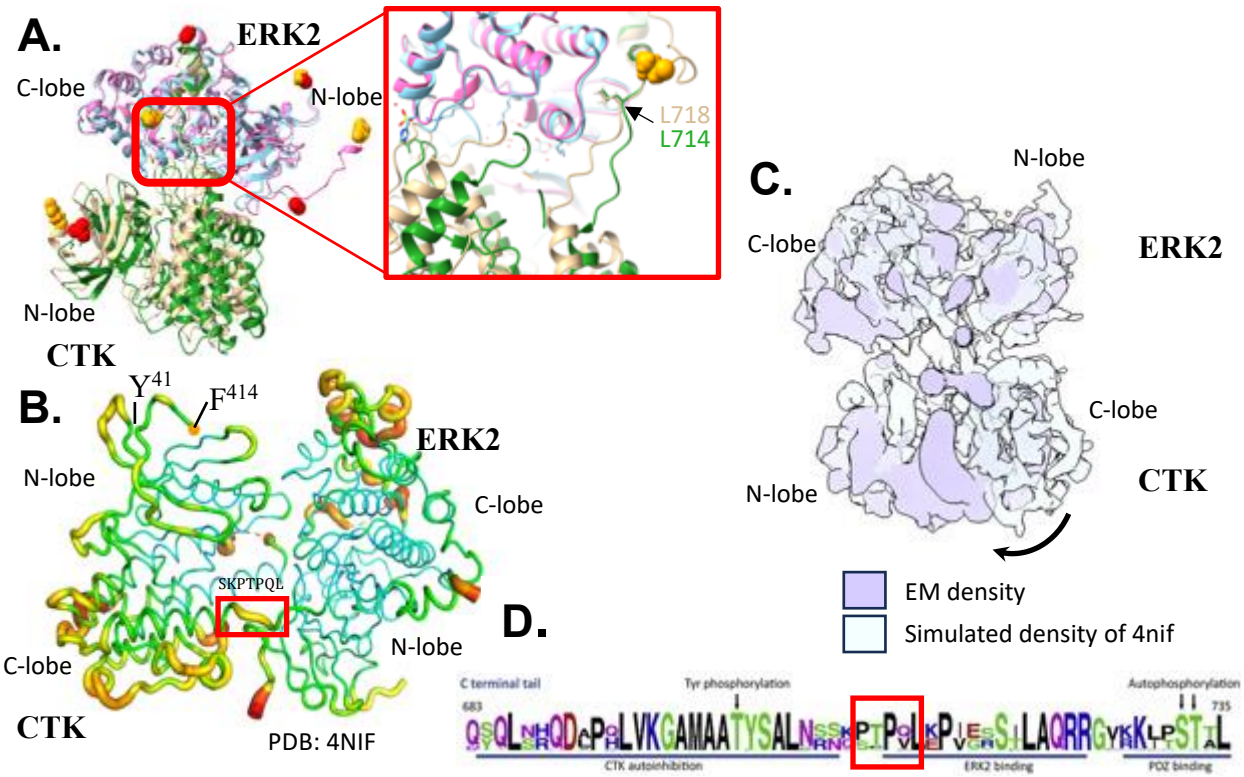


Figure 3.8: **Rigid body motion of CTK:ERK2. (A)** A comparison of the AF-predicted CTK:ERK2 complex (with ERK2 shown in pink and CTK in gold) and the CTK:ERK2 crystal structure (PDB: 4NIF) (with ERK2 in cyan and CTK in green). The red box highlights Leucine 718 in the AF-predicted model (colored in gold) and Leucine 714 in the crystal structure (colored in green) as the hinge point between CTK and ERK2. Red spheres represent the start and end points of ERK2 and CTK in the crystal structure, while orange spheres indicate the start and end points of ERK2 and CTK in the AF-predicted model. **(B)** The CTK C-tail exhibits a high B-factor value in the crystal structure (highlighted in the red box), suggesting that it is a flexible region. **(C)** A comparison of the crystal structure of CTK:ERK2 (PDB: 4NIF) and EM density suggests that CTK undergoes rigid body motion, requiring it to swing left (indicated by the black arrow) to fit the EM density. **(D)** The PTPL motif is highly conserved across 40 RSK orthologs, indicating its functional importance. The presence of a proline residue in the region where the secondary structure is disrupted supports the hypothesis of a hinge point where rigid body motion occurs.

```
HUMAN RSK1    MPLAQLKEPWP LMEL VPLD----PENGQTS-------G EEAGLQPSKDEGVLKEISITHHVKAGS      54
HUMAN RSK2    MPLAQLADPWQKMAVESPSDSAENGQQIMDEPMGEEEI  NPQTEEVS I KEIAITHHVKEGH      60
              * * * * * *  : * *     *  :     .     * * * *.              *   : : * . . : *    : ***: * * * * * *  *

HUMAN RSK1    EKADPSHFELLKVLGQGSFGKVFLVRKVTRPDSGHLYAMKVLKKATLKVRDRVRTKMERD     114
HUMAN RSK2    EKADPSQFELLKVLGQGSFGKVFLVKKI SGSDARQLYAMKVLKKATLKVRDRVRTKMERD     120
              * * * * * *: * * * * * * * * * * * * * * * * * : *: : *:  : * * * * * * * * * * * * * * * * * * * * * * * ***

HUMAN RSK1    ILADVNHPFVVKLHYAFQTEGKLYLILDFLRGGDLFTRLSKEVMFTEEDVKFYLAELALG      174
HUMAN RSK2    ILVEVNH PFI VKLHYAFQTEGKLYLILDFLRGGDLFTRLSKEVMFTEEDVKFYLAELALA      180
              * * : * * * *  * *: * * * * * * * * * * * * * * * * * * *
```

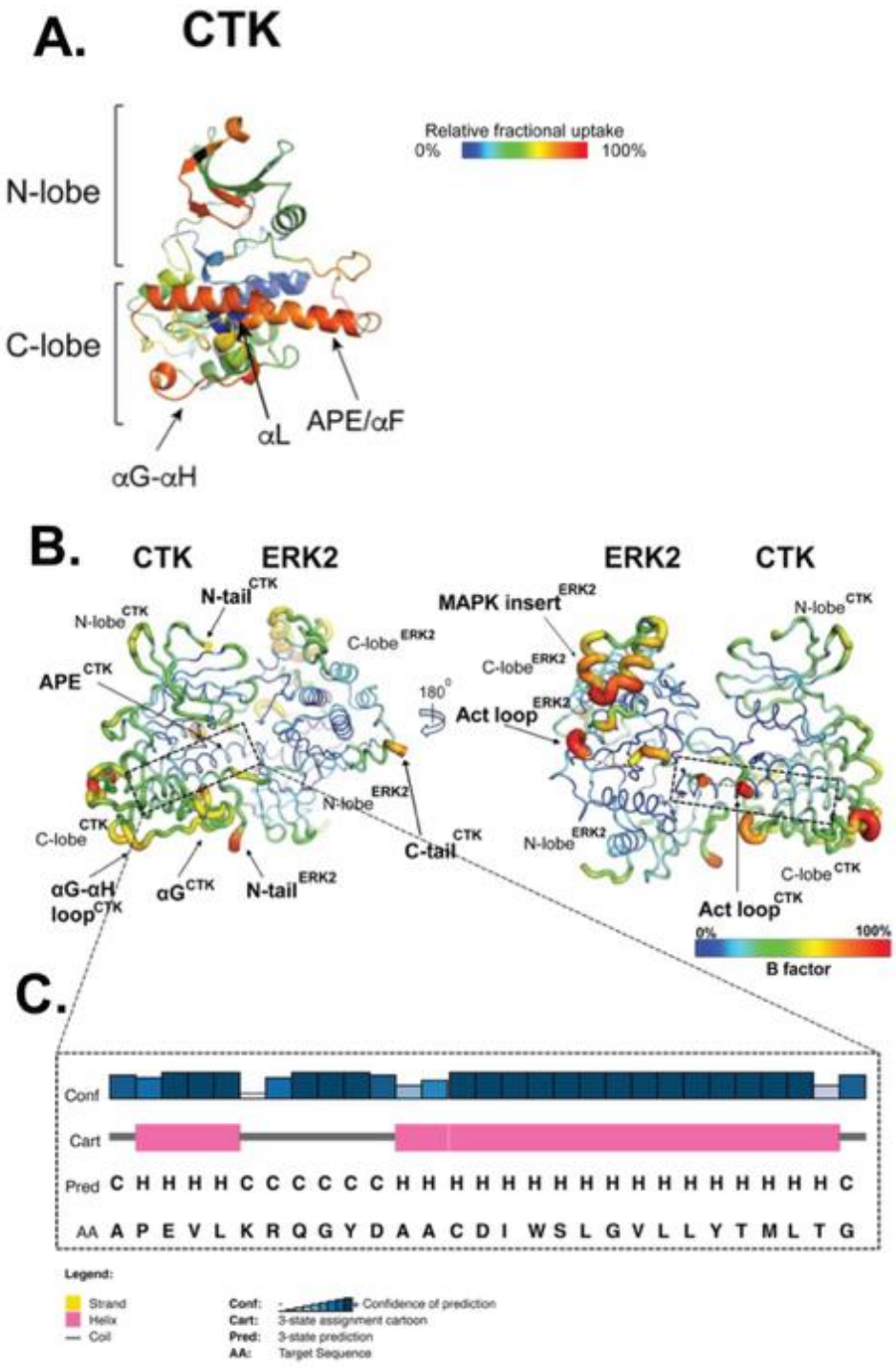


Figure 3.10. CTK C-lobe αF helix flexibility. (A) Per residue fractional uptake is displayed as b-factors colored onto the corresponding kinase domains of RSK2(CTK). B-factors are colored as a rainbow scale. **(B)** CTK:ERK crystal structure (pdb: 4nif) colored by b-factors. **(C)** Secondary structure prediction of CTK from the APE motif throughout the αF helix. [hdxms paper reference]

Furthermore, the NTK appears to be the domain undergoing the largest displacement of the three kinase domain (Fig. 11). Using sequences from UniProt and adjusting the number of output models, we generated approximately 100 AlphaFold-predicted models of the RSK2:ERK2 complex. When comparing these models, we observed consistent trends: constraining ERK2 led to rigid body motion of CTK around leucine 714, while NTK exhibited the greatest variability among the three kinase domains. The N-terminal linker displayed the lowest pLDDT score, consistent with its flexible and intrinsically disordered nature. To further quantify the variations in CTK and NTK, we performed root-mean-square deviation (RMSD) analysis to measure differences between models in the ensemble. The results support our hypothesis that CTK and NTK move relative to the fixed ERK2 domain, with NTK exhibiting the greatest mobility among the three kinase domains (Fig. 11B). Additionally, 3D variability analysis of EM density further confirms that NTK is the most dynamic domain, undergoing motion away from the CTK:ERK complex (Fig. 11C).

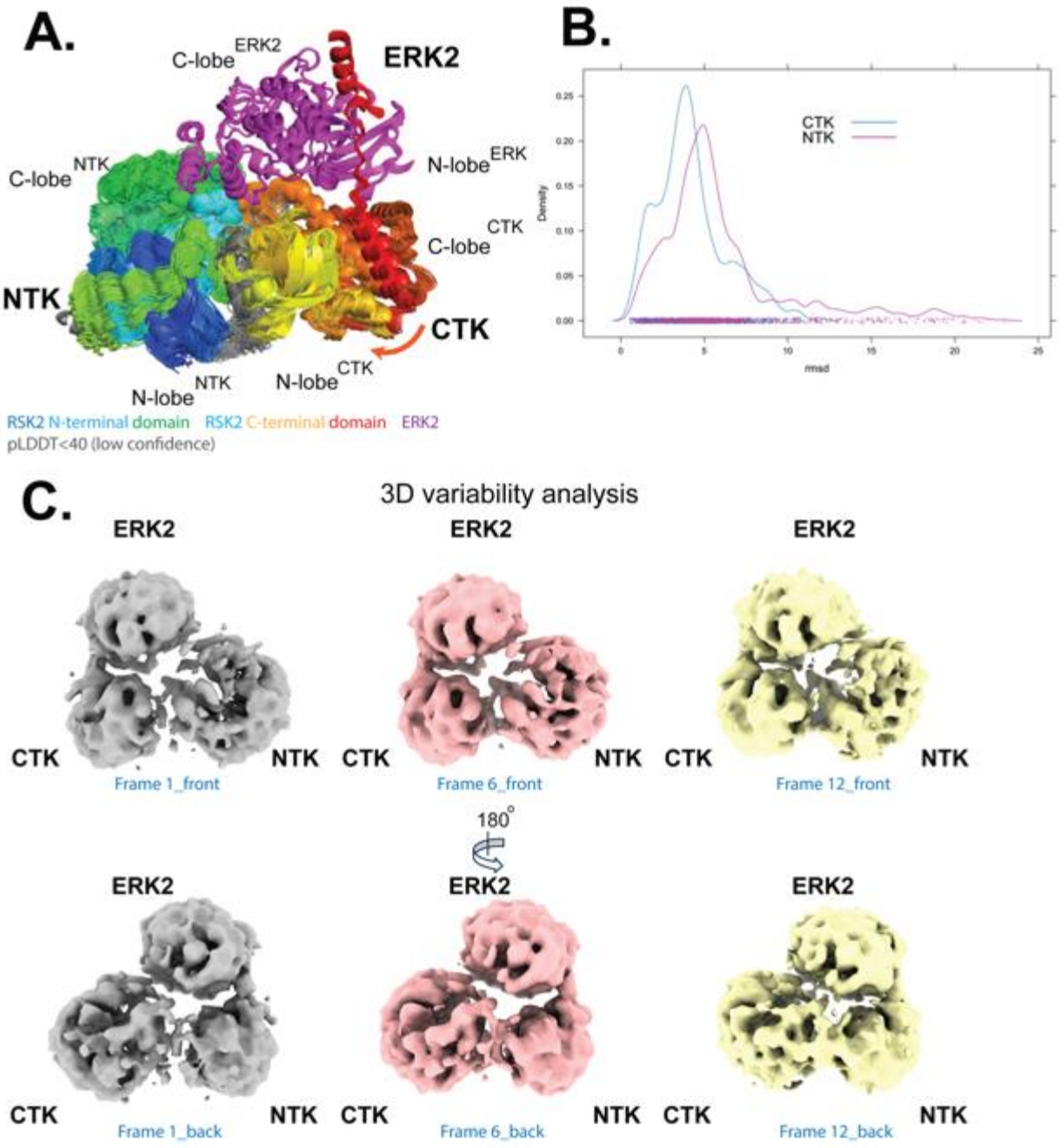


Figure 3.11: **NTK is the most mobile domain. (A)** A comparison of multiple AF-predicted models of RSK2:ERK2 complex includes ERK2 (magenta), CTK C-lobe (red), CTK N-lobe (yellow), linker regions with pLDDT < 40 (gray) and >40 (green) , NTK N-lobe (blue), NTK C-lobe (green). These models suggest a slight rigid body motion of CTK relative to ERK2 around the CTK C-tail (indicated by the orange arrow), with NTK being the most mobile domain. **(B)** The RMSD plot for CTK and NTK indicates flexibility in both domains, with NTK (magenta) exhibiting more movement than CTK (blue). **(C)** The 3D variability analysis shows that NTK demonstrates a motion of departing from CTK:ERK2 complex, as indicated by different frame view in the front and back

To better understand the factors contributing to the conformational dynamics of NTK, we examined the long, intrinsically disordered interkinase linker (Fig. 12). In the CTK:ERK2 crystal structure (PDB: 4NIF), the residues preceding the β1 sheet are truncated (ending in F414), leaving the secondary structure of this region unresolved (Fig. 8B). However, in the AlphaFold-predicted model for NTK:CTK:ERK this linker preceding β1 is present and adopts a helical fold, hereafter referred to as the C-terminal Linker (CtL) motif. The CtL motif consists of CtL-helix starting at I407 and ending at Y422. Y422 and F418 fill a conserved hydrophobic pocket on the top of the β sheet that is shared by all protein kinases (Fig. 12B). In the crystal structures of NTK, residues after P346 are disordered, but ordered in our Alpha-Fold predicted model. The ordered region connects to the C-terminus of NTK is referred as the N-terminal Linker (NtL) motif. The NtL-motif contains an NtL-helix that is part of a conserved and well-ordered ATP binding pocket (Fig. 12B). We propose that the long interkinase linker adopts an ordered conformation when the NtL-helix motif interacts with the CtL-motif as well as NTK, CTK, and ERK, and this is consistent with our EM density (Fig. 13). Additionally, we hypothesize that the linker undergoes a disordered-to-ordered transition, explaining why NTK is the most mobile domain of the three. Specifically, when the linker is disordered and density is absent, strong density for NTK is not observed (Fig. 13B). The weak density of the N-lobe of NTK, compared to the strong density of the C-lobe, is consistent with previous studies showing that the NTK N-lobe is malleable [cite HDXMS paper] (Fig. 15) (Aronchik et al., 2014; Costales et al., 2014; Ikuta et al., 2007; R. Jain et al., 2015; Malakhova et al., 2009; Utepbergenov et al., 2012) . However, when the linker adopts an ordered conformation, clear density is observed for most of the NTK (Fig. 13C).

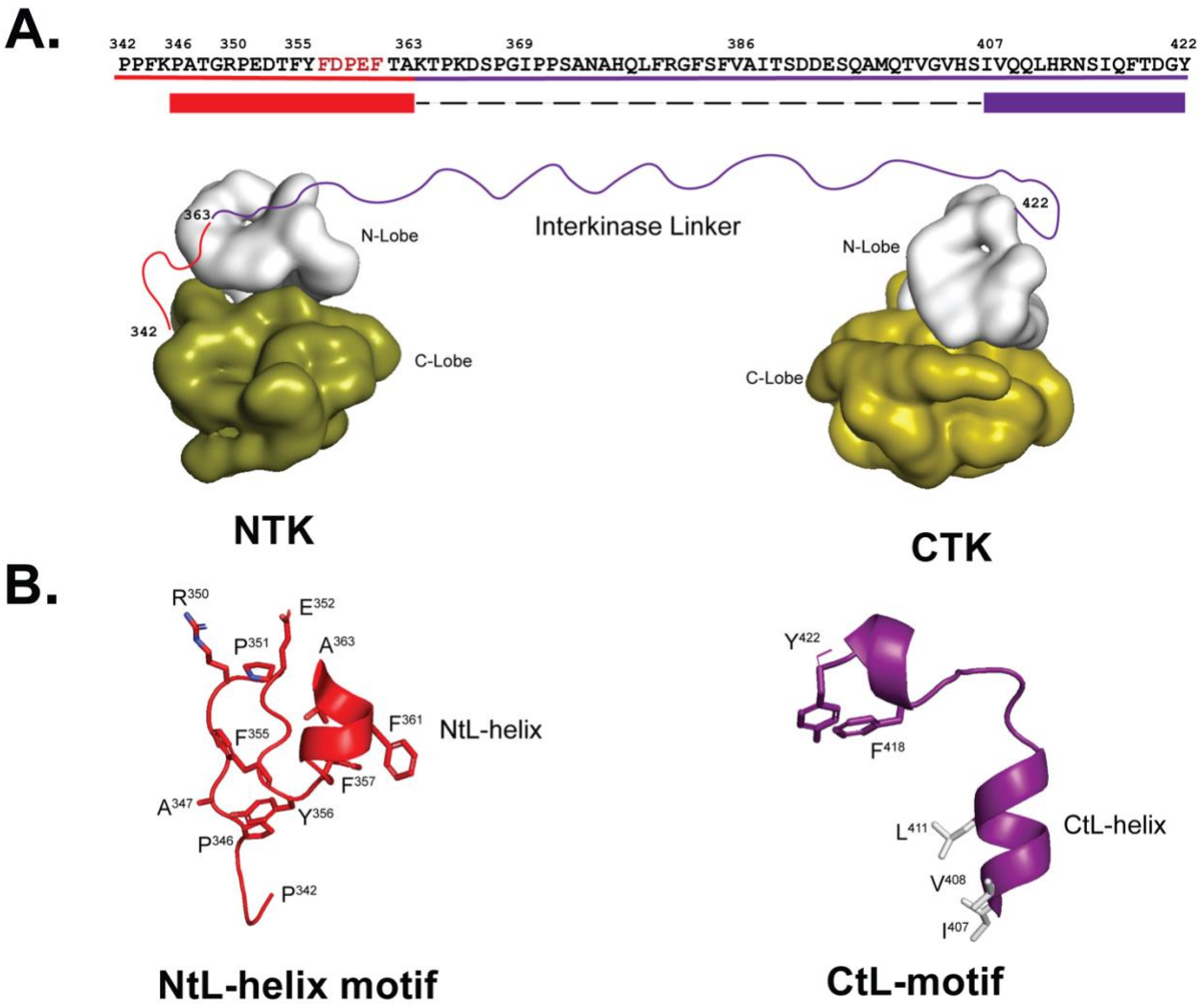
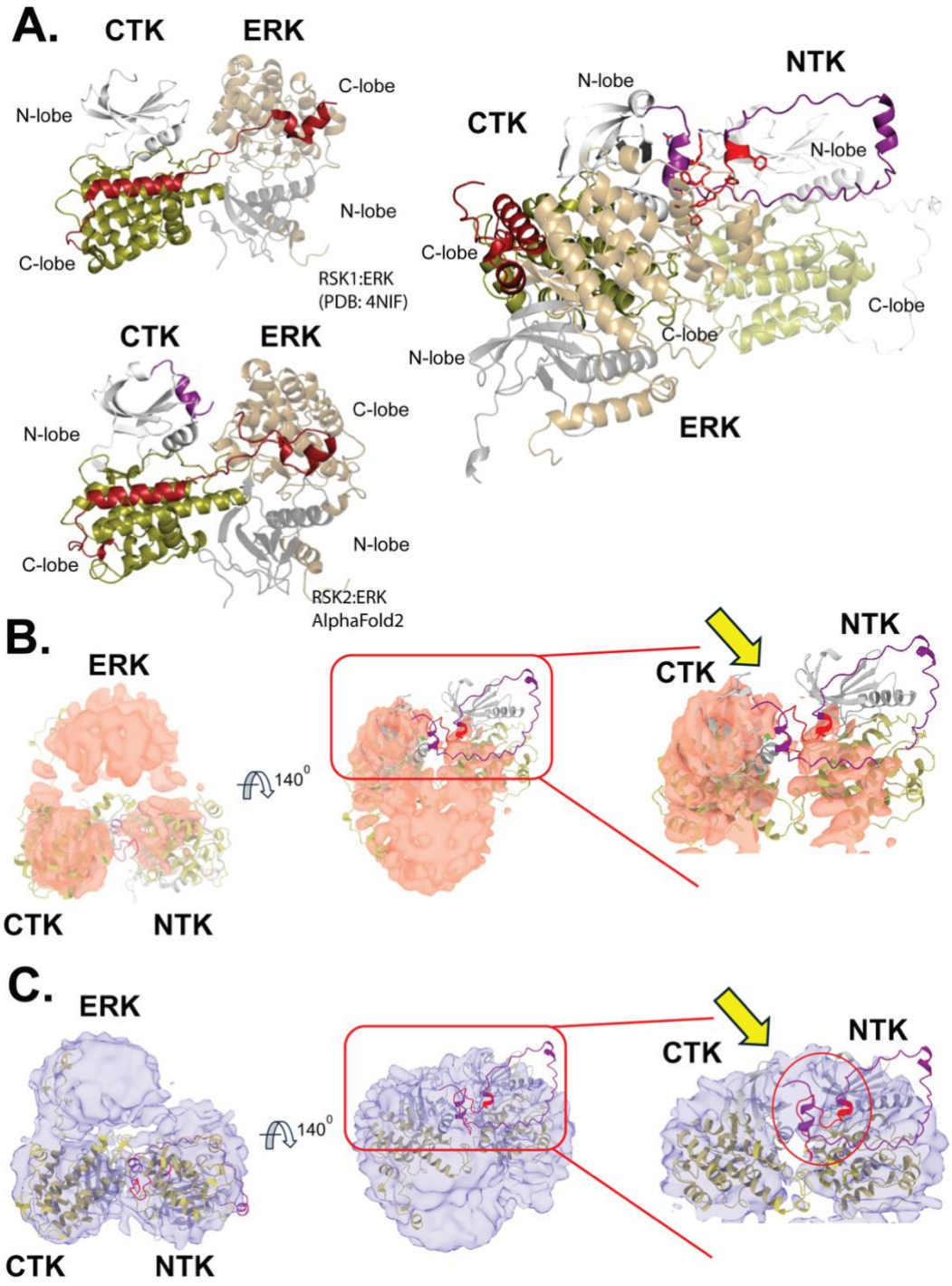


Figure 3.12: Region of the interkinase linker (purple, red) are ordered in the RSK:ERK complex. (A) Schematic representation of the interkinase linker showing the relative position between NTK and CTK; number shows the starting and ending residues of the linker (bottom); boxes show the ordered helixes in the p90RSK2:ERK2 model; dashes show disordered regions. **(B)** The linker is ordered in 2 regions: N-terminal linker (NtL) helix motif (colored in red) and C-terminal linker (CtL) motif (colored in purple). Residues that form the interactions with NTK, ERK, CTK are shown.



<u>Figure 3.13</u>: **Linker becomes partially ordered in the RSK:ERK trimer**. **(A)** Comparison of CTK:ERK2 (PDB:4NIF) and AF predicted model of CTK:ERK2. The purple helix is an extra helix that is not present in the crystal structure. And is belived to be ordered by NTK and EKR (right side). **(B)** In the dimer structure, when there is no density is observed for the purple helix, NTK is not present. **(C)** In the trimer structure, when there is density observed for the purple helix, there is strong density account for NTK which suggested when the linker is ordered (circled in red), it stabilized NTK thus more density is observed.

To further investigate how CTK, NTK, and ERK organize the linker region, we more closely examined the interactions predicted by AlphaFold. Figure 14A shows how the CtL-motif interacts with the CTK core where it packs against its own αC helix. On the left, αC helix (L467) packs against and orders the R-spine (residues F562 and L467). Additionally, E463 on the αC helix forms an electrostatic interaction with K451 on the N-lobe of CTK, which is characteristic of an active kinase. Y422 and F407 in the CtL motif pack into a conserved hydrophobic pocket on top of the β sheet. I464 and L468 on αC helix establish hydrophobic interactions with L411, V408, and I407 in the CtL-helix. E465 and E462 from the αC helix form ionic interactions with Q567 and R569 from the C-lobe of CTK. Furthermore, K231 from the C-lobe of ERK interacts with R469 on the αC helix of CTK and S406 on the linker (Fig. 14A).

The C-tail is a conserved features of all AGC kinases and plays important roles in regulation. It contains the C-lobe tether (CLT), active site tether (AST), and N-lobe tether (NLT). In previous structures of NTK, the C-tail up to P346, which corresponds to the CLT, is ordered and the rest is disordered. The structurally conserved CLT is ordered against the C-lobe in all AGC kinase structures. In addition to the disorder of the AST and NLT, the N-lobe of NTK is highly malleable, and the R-spine broken (Fig. 15). Here in our RSK:ERK model, the AST region (F361, F357) is well-ordered to form a adenosine binding pocket. Additionally, L147, V131, L150 from the N-lobe of NTK and L200 from the C-lobe of NTK together with the AST form a hydrophobic pocket to accommodate SL0101, which is an ATP mimetic (Fig. 14B).

In the model, the NtL-motif bound to the NTK core interacts directly with the CtL motif bound to its own core (Fig. 14C). Specifically, the interaction is stabilized by hydrophobic packing of the two motifs (F355, Y356, A347, P346 on NtL-helix motif packs against I407, V406 on CtL-

helix). Additionally, R350 on the NtL loop interacts with Y483 and D481 on the N-lobe of CTK. E352 in NtL loop forms hydrogen bonds to K86 on the N-lobe of NTK while P351 on the NtL loop form hydrophobic packing with L96 on the N-lobe of NTK (Fig. 14C).

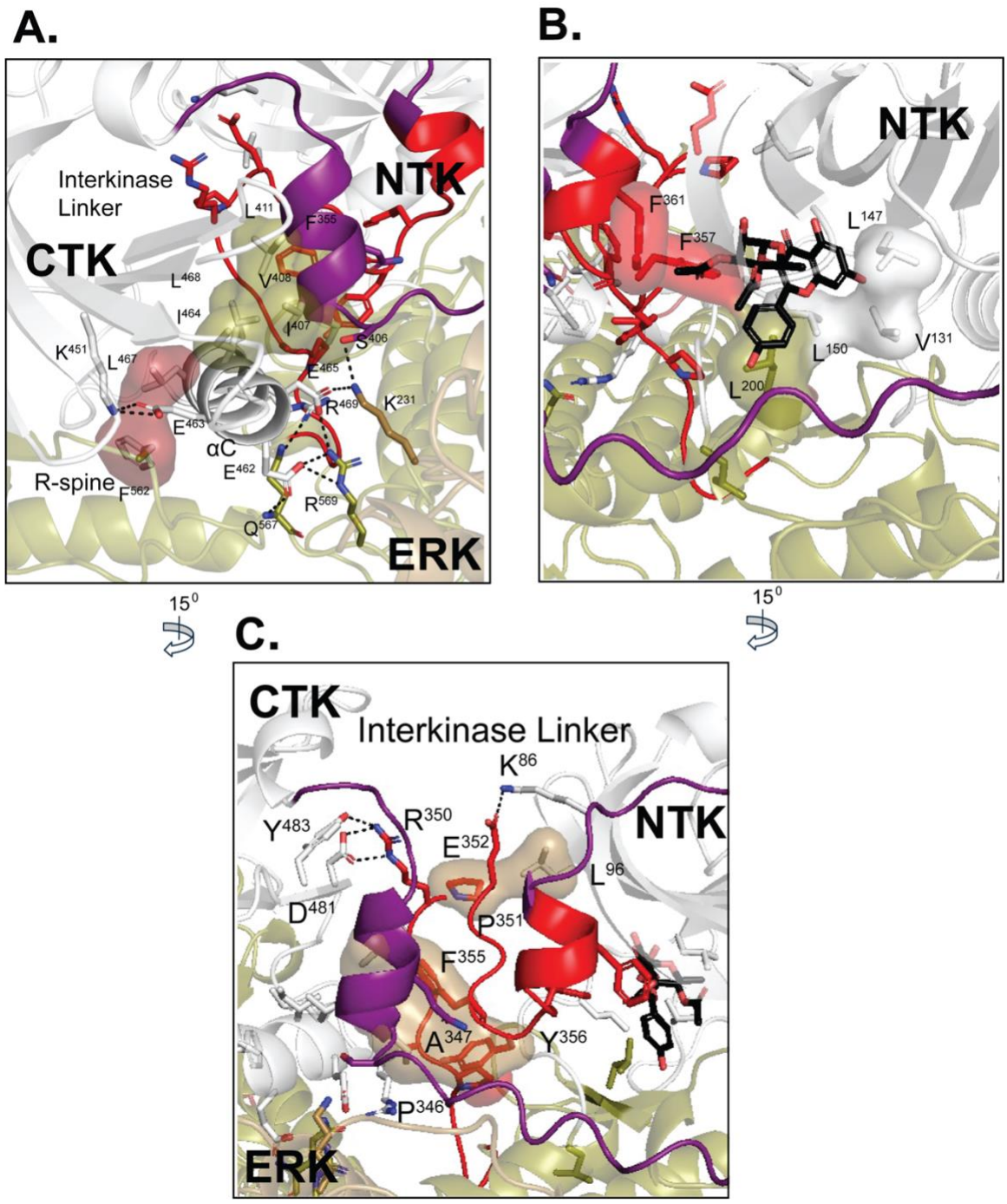


Figure 3.14: Zoom in view of interkinase linker interaction with NTK, CTK, and ERK. **(A)** The interactions of CtL motif with αC, R-spine, C-lobe of CTK and ERK. **(B)** Important residues forming hydrophobic pocket to accommodate SL0101**. (C)** The interaction of NtL helix motif, CtL hehix, N-lobe of CTK, N-lobe of NTK and ERK.

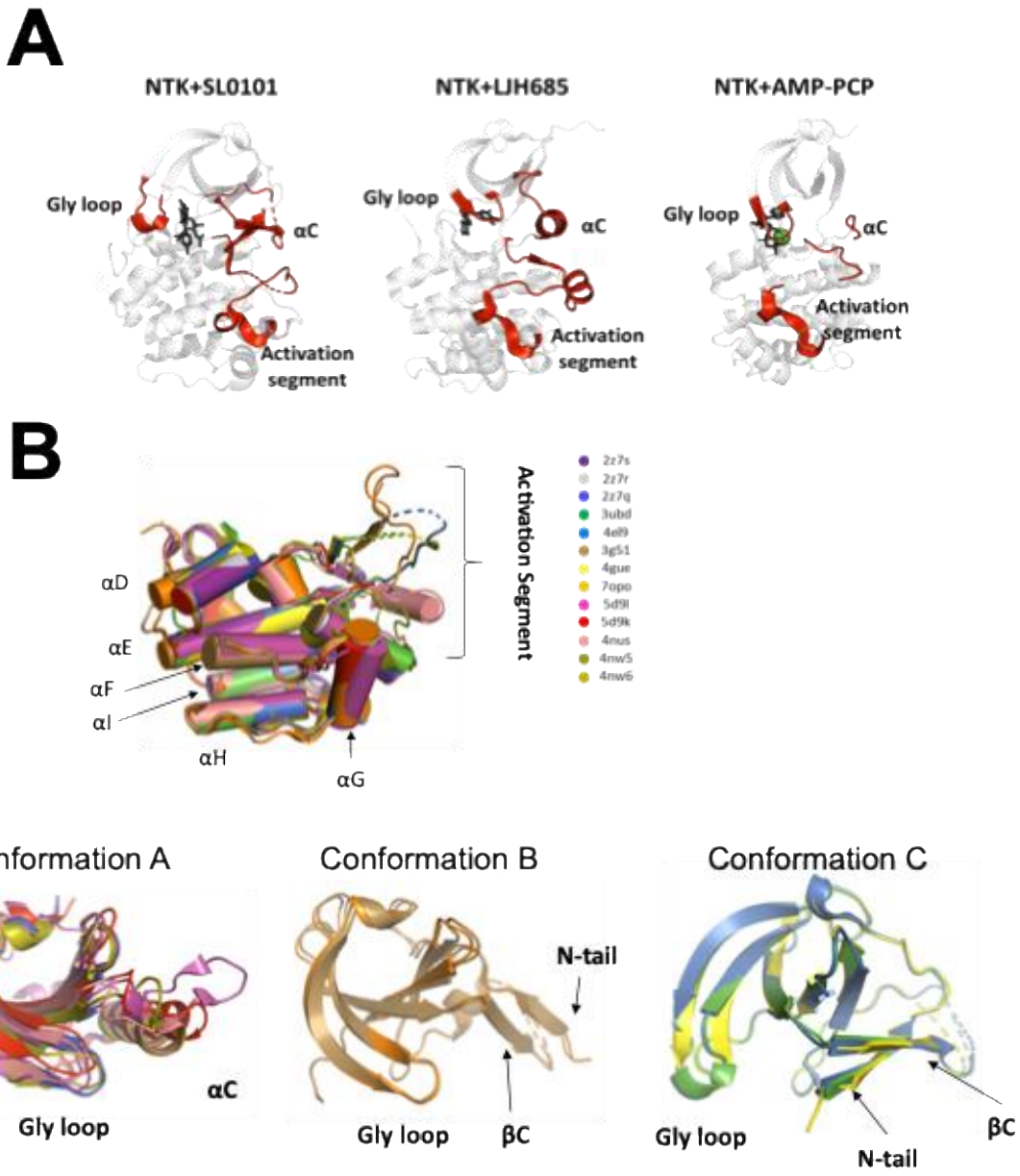


Figure 3.15: The N-lobe of NTK is malleable. (A) The crystal structure of NTK with different inhibitors shows different N-lobe conformations whereas the C-lobe, with the exception of the Activation Segment, is stable **(B).** The different conformations of the N-lobe are categorized as Conformation A, B, and C. Figure adapted from [HDXMS paper]

D. Discussion

The activation mechanism of p90RSK involves multiple kinases and sequential activation steps, making it a complex process to understand. In this study, we use cryo-EM and AlphaFold modeling to investigate the conformational dynamics of the first steps in this activation mechanism, where ERK2 binds to RSK2. While it is well-established that ERK2 must be activated to bind RSK2, our study, consistent with previous research (Sok et al., 2020), shows that ERK2 does not need to be phosphorylated to bind RSK2 *in vitro*. Our structure further confirms that the stoichiometry of this complex is 1:1.

Consistent with ERK2, which was the second kinase to have its crystal structure solved (F. Zhang et al., 1994), ERK2 in our dataset is also highly stable. In fact, it stands out as the most well-resolved kinase domain among the three, (configuration 3). This stability plays a key role in stabilizing the intrinsically disordered C-tail of CTK. There may be multiple steps involved in the binding mechanism. In solution, RSK2 in its inactive form is highly flexible, which likely explains why previous efforts to crystallize full-length (FL) RSK2 were unsuccessful. The only available structures of RSK are of the individual kinase domains, NTK and CTK, excluding the flexible N-terminal, linker, and C-tail. However, when ERK binds to the C-tail of RSK, it organizes this disordered region into an ordered structure.

Additionally, CTK undergoes rigid-body motion around a conserved leucine. In some cases, when CTK is closest to NTK, the three domains—CTK, NTK, and ERK2—organize the interkinase linker into an ATP-binding pocket, for the NTK that is now primed for ATP binding. When the interkinase linker is ordered, the NTK is observed in the density (configuration 1), while when unordered, NTK is absent (configuration 2). NTK is the most mobile domain observed in

both cryo-EM data and AlphaFold models, which aligns with its function: the NTK needs to phosphorylate its own C-tail to release ERK2 or downstream substrates.

Members of the MAPK pathway exhibit the phenomenon of adopting different conformations depending on their phosphorylation state. For example, MK2 and non-phosphorylated p38α adopt a parallel conformation, which switches to an antiparallel conformation when p38α is phosphorylated. In contrast, RSK1(CTK) and ERK2 adopt an antiparallel conformation in both non-phosphorylated and double-phosphorylated states. Given this, we are particularly interested in the conformations of the FL RSK2:ERK2 complex. According to cryo-EM and AF-predicted models, in their apo forms, CTK and ERK adopt a head-to-tail conformation, while CTK and NTK adopt a head-to-head conformation. This represents one of the rare instances of three kinase domains being present in a single complex.

In conclusion, this stable complex provides excellent opportunities to understand the interactions within the MAPK pathway and how members of three different kinase families cross-talk with each other. Such interactions are rare and difficult to trap due to their flexibility, complex mechanisms, and transient nature. Our model suggests that in the inactive state, these complexes likely exist in multiple conformations to accommodate overlapping signaling pathways, various ligands, and progressively dynamic activation mechanisms. This study also further emphasizes how important it is to characterize full length complexes to fully understand the domain organization, conformational dynamics and potentially to provide insight into the various steps in the activation mechanism.

Chapter III, in full, is currently being prepared for submission for publication of the material. **HOANG P. M. NGUYEN**, Evan Kazuo Kobori, Jian Wu, Roland Dunbrack, Mariusz Matyszewski, Rodeon Malinovski, Katherine Chen, Mark Anthony Herzik, Susan Taylor. *Domain organization and conformational dynamics of a p90RSK2:ERK2 complex.* The dissertation author was the primary researcher and author of this paper.

Chapter IV

Key Motifs in the C-terminal Tail Contribute to ATP Binding of AGC Kinases

A. Introduction

Almost all eukaryotic protein kinases are activated through phosphorylation of their activation loop (Nolen, Taylor, & Ghosh, 2004) Phosphorylation of the activation loop drives formation of the R-spine and establishes interaction networks that connect the active site to the N- and C-lobes of the kinase domain, stabilizing and promoting an active kinase conformation (Gógl, Kornev, Reményi, & Taylor, 2019; Taylor, Keshwani, Steichen, & Kornev, 2012) . In addition to the AL P-site, the AGC kinases have a conserved C-terminal tail (C-tail) that also harbors phosphorylation sites (Fig. 1).

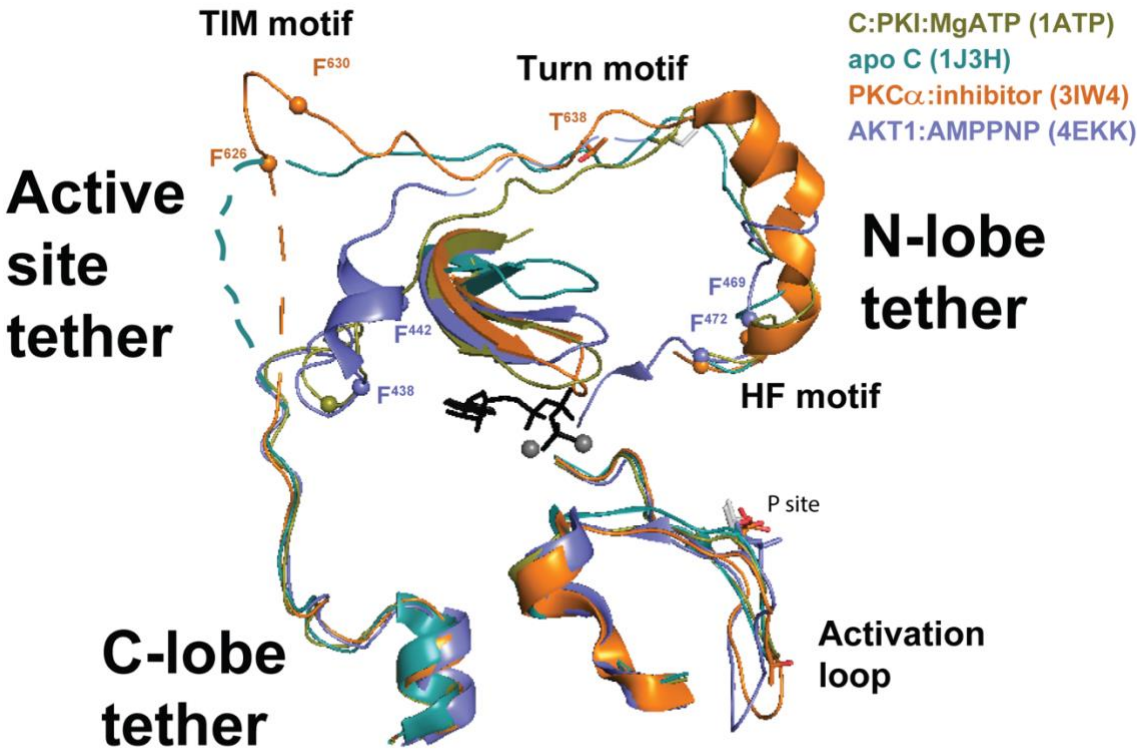


Figure 4.1: Conserved C-tail and activation loop in AGC kinases. C-tail harbors the C-lobe tether, active site tether, N-lobe tether, TIM motif, Turn motif, HF motif, and adopts multiple conformations depending on the active or inactive state. P-site on activation loop is conserved in all AGC kinases.

For PKC to achieve catalytic activity, it must be phosphorylated at three conserved sites: the activation loop, which is phosphorylated by 3-phosphoinosotide-dependent protein kinase-1 (PDK1), and two sites within the C-tail: the turn motif and the hydrophobic motif (HM) (Fig. 2). These phosphorylation sites are regulated by mTORC2, which influences the activity of all but three of the nine PKC isoforms (Dutil, Toker, & Newton, 1998; Facchinetti et al., 2008; Good et al., 1998; Ikenoue, Inoki, Yang, Zhou, & Guan, 2008; Keranen, Dutil, & Newton, 1995). While both the activation loop and HM phosphorylation are essential for cellular activity, the turn motif phosphorylation is primarily critical for organization of the AST which contains the binding site for the adenosine ring of ATP (Bornancin & Parker, 1996; Edwards & Newton, 1997; Orr & Newton, 1994) . In contrast, for Akt, phosphorylation of the HM enhances its activity but is not required for catalysis. Instead, phosphorylation of the activation loop is both necessary and sufficient for its activation (Fig. 1) (Balasuriya et al., 2018; Chu et al., 2018; Yang et al., 2002) . Most AGC kinases require a phosphorylation site that immediately follows the hydrophobic motif (HF), which is anchored to the αC-helix. The exceptions are PKA and PKG, which terminate at the HF motif.

PKA, which is synthesized as a fully active kinase with two phosphorylation sites – the AL-Site and a turn motif. The C-subunit then forms a holoenzyme complex (R_2C_2), where interaction with inhibitory regulatory (R) subunits maintains it in an inactive state. Activation is dependent on cAMP which binds to the R subunit. This unleashes an active conformation of the C-subunit that can phosphorylate downstream substrates (Zhang et al., 2012) . PKC is also synthesized and stored in its resting state as an inhibited complex that is activated by other second messengers, Ca+ and diacyl glycerol (DAG). PKC has an inhibitory pseudo-substrate site at its N-terminus that is locked into the active site cleft.

p90RSK is unique among kinases as it contains two kinase domains: the N-terminal kinase domain (NTK), which belongs to the AGC kinase family, and the C-terminal kinase domain (CTK), which belongs to the calcium/calmodulin kinase family (Fig. 2). For p90RSK to become fully active, it requires two upstream kinases, ERK2 and PDK1, with phosphorylation occurring through a sequential, multi-step process. The consensus mechanism suggests that CTK phosphorylates the hydrophobic motif, creating a docking site for PDK1 to bind and subsequently phosphorylate the activation loop of NTK (Anjum & Blenis, 2008; Jensen et al., 1999) .

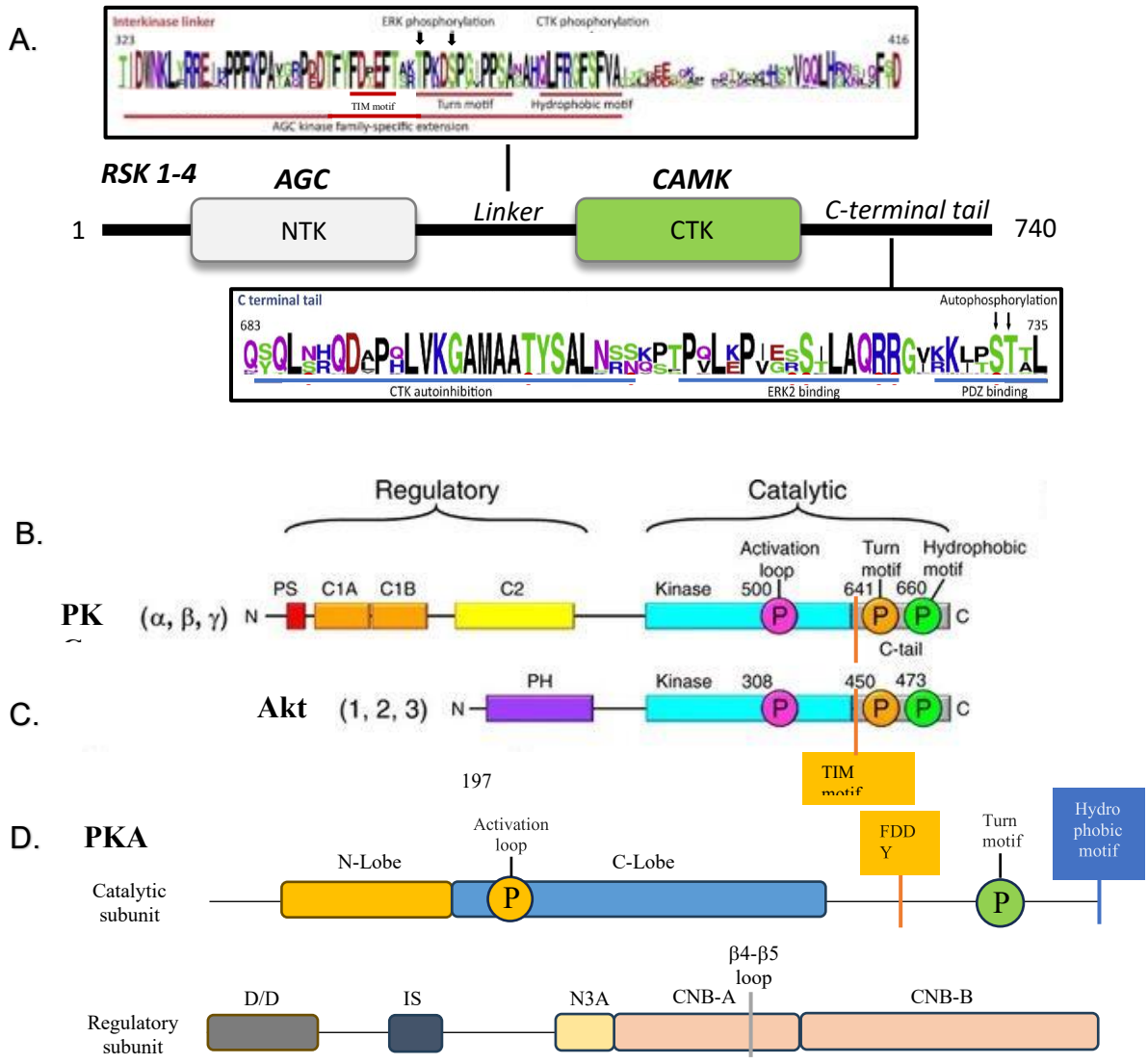


Figure 4.2: **Schematic representation of p90RSK (A), PKC (B), Akt (C), and PKA (D) domain structure** highlighting the FDDY, TIM, turn motif and hydrophobic motif, the pseudosubstrate (PS) region, the β4-β5 loop, the C-tail of p90RSK (AGC kinase family-specific extension in p90RSK). Figure B and C is adapted from with some modifications (Baffi et al., 2021)

Most of these activation elements are located in the C-tail of AGC kinases. The AGC kinase C-tail is highly conserved and contains the FD(X)$_{1–2}$Y/F motif (hereafter referred to as the FDDY motif), which is required for ATP binding, specifically for binding the adenine ring of ATP. Additionally, the turn motif is a conserved phosphorylation site positioned six residues downstream from the FDDY motif, while the hydrophobic motif (FxxF) plays a crucial role in both activation and stabilization of AGC kinases located at the end of the C-tail (Fig. 3) (Arencibia, Pastor-Flores, Bauer, Schulze, & Biondi, 2013; Kannan, Haste, Taylor, & Neuwald, 2007) .

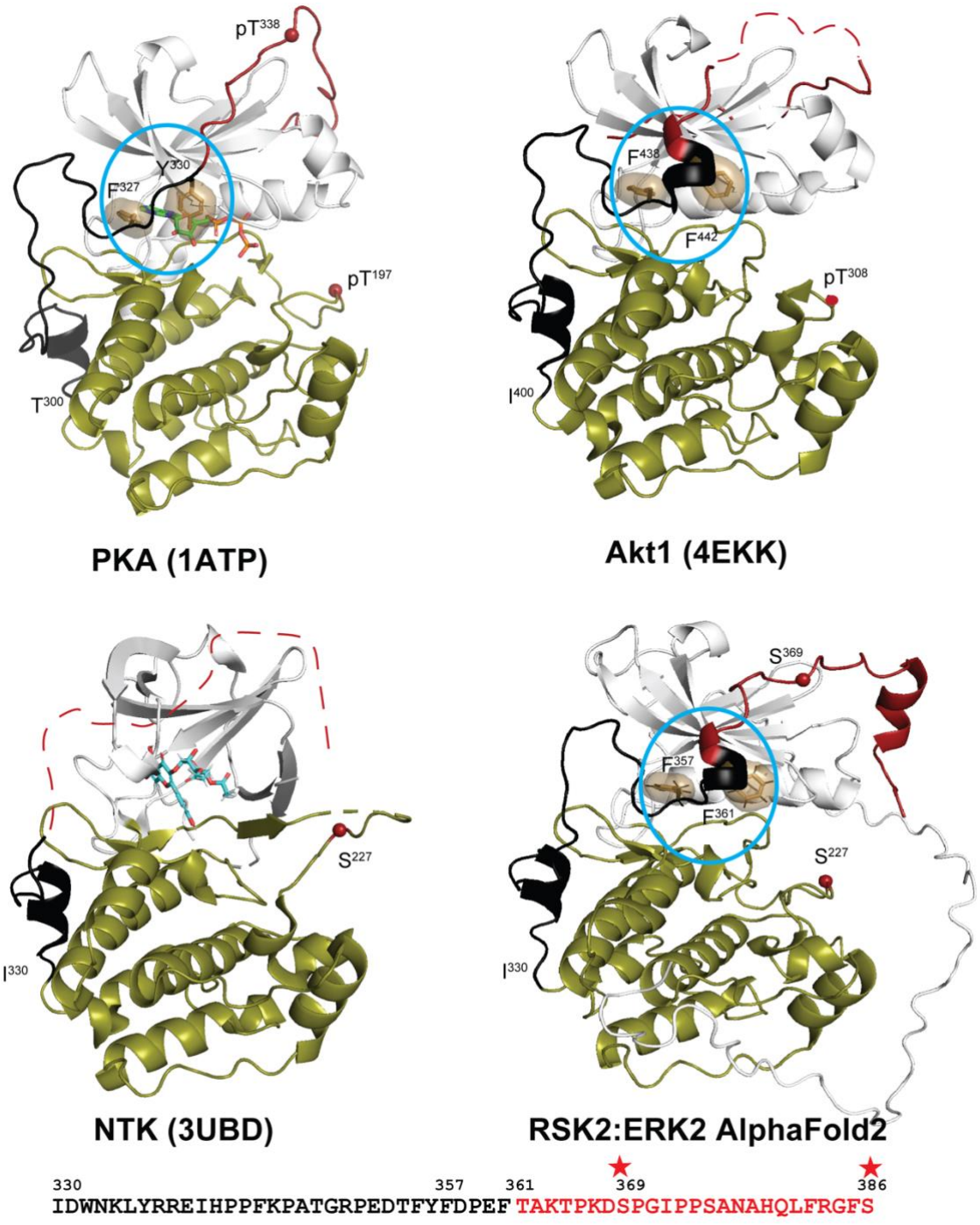


Figure 4.3: **The TIM motif adopts a sequence conserve and unique fold**. PKA does not have a TIM motif so the FDDY loop fold differently (top left) compared to a TIM motif fold in Akt1 (top right). All of the NTK structure is either truncated or disordered in this region (bottom left). Alpha fold pick up the TIM fold for RSK2 even almost all AGC kinases do not have this fold (bottom right)

The recently discovered TIM motif explains how mTORC2 regulates PKC and Akt, and based on our work it may also regulate p90RSK1 (Baffi et al., 2021) . Interestingly, the TIM motif overlaps with, but is distinct from, the FDDY motif. A novel helix in the AST is a unique feature of the TIM motif that distinguishes it from the FDDY motif seen in PKA. While the mechanisms through which mTORC2 regulates these kinases differ, for PKC, mTORC2 performs the rate-limiting step of PKC maturation by phosphorylating the TIM motif. This phosphorylation leads to the dissociation of the PKC dimer, recruiting PDK1 to the unphosphorylated hydrophobic motif to promote activation loop phosphorylation. In Akt, activation loop phosphorylation alone is sufficient to activate the kinase. For PKC, however, this site alone does not fully activate the enzyme; it facilitates a low level of catalytic activity needed to phosphorylate the hydrophobic motif. Once the hydrophobic motif is phosphorylated, the final step of PKC maturation involves pseudo-substrate autoinhibition, yielding a primed (catalytically competent and stable) and inactive PKC enzyme. While activation loop and hydrophobic motif phosphorylation are essential for PKC activity, the phosphorylation of the turn motif is not required for catalysis but instead promotes protein stability and binding of the adenosine ring. For Akt, the turn motif is phosphorylated by mTORC2 co-translationally at the ribosome. Current understanding suggests that several AGC kinases are activated by both turn motif and hydrophobic motif phosphorylation. In the case of p90RSK, the phosphorylation of the hydrophobic motif is carried out by CTK, which provides a docking site for PDK1 to phosphorylate the activation loop of NTK. Although only one cellular-level study has shown mTORC2 regulation of p90RSK1, little is known about the regulation of p90RSK2 or other p90RSK isoforms (Chou et al., 2020) . Furthermore, PKAα, PKCδ, PKCθ, and PKCη are not mTORC2-dependent.

In this study, we analyze sequence homology, published structures, and AlphaFold models to understand how phosphorylation at the TIM and turn motifs influences the phosphorylation or stability of these kinases. We observed that phosphorylation of the TIM and turn motifs helps anchor the C-tail to the G-loop or N-lobe, which in turn aids in sensing the open and closed conformations of the kinase core domain. The FDDY and TIM motifs, thus, not only form the adenosine binding pocket but also facilitate domain-domain interactions that play a crucial role in regulating these phosphorylation events.

B. Methods

Alpha Fold modeling: AlphaFold 2.3.0 modeling of the RSK2:ERK2 complex was performed with localcolabfold (Mirdita et al., 2022b) downloaded from https://github.com/YoshitakaMo/localcolabfold on a Dell Alienware desktop machine with an RTX 4090 GPU of 24 Gbytes. We produced 80 models of RSK2:ERK2 with 40 seeds and all AlphaFold v2.3 weight sets without the use of templates from the Protein Data Bank (PDB). Structures were ranked with the default function in Colabfold: 0.8*ipTM + 0.2*pTM. Structures were visualized in PyMOL (v.2.5, Schrödinger, Inc.). And the highest ranking model was chosen to study. Model of the FL RSK2 were generated using the ColabFold server. Sequences for RSK2 and ERK2 can be obtained from Uniprot with accession number: P51812, P28482 respectively. And highest ranking model was used to study.

Crystal analysis: We systematically analyze all available crystal structures of PKA, Akt, PKC, NTK, R_2C_2 holoenzyme in different apo, ATP analogs, inhibitors bound state and in complex with its own regulatory subunits to understand the role of these crucial motifs, the active, inactive state conformations. We decided to show the representative structures of each state and motifs.

Here are the PDB code for these structures: PKA (1ATP), Akt1 (4EKK), NTK (3UBD), apo PKA (1J3H), PKCι (3A8W), PKCα(3IW4), PKCβ (3PFQ), apo RIIβ holoenzyme (3TNP), and ADP bound RIIβ holoenzyme (3TNQ).

cryoEM data: We use the same data set we analyze in chapter III of this thesis for this chapter. Specifically, Figure 13 in chapter III shows data support our hypothesis about the present of TIM motif which is organized by the CtL helix.

C. Results and Discussion

Because our Alpha Fold model predicts a TIM motif (TIM helix) in the NTK of p90-RSK , I asked if the sequence data support this hypothesis. Two regions that define the TIM motif are in the C-tail surrounding the TIM helix and, in the G-loop. This prompted us to investigate the sequence alignment of the G-loop and TIM motifs in various AGC kinases and to explore in more detail the functional consequences of these sequence differences. While these alignments are part of the original TIM discovery (Baffi et al., 2021) , less attention have given to RSK2 due its lack of structural information of the Ctail of RSK2. With the AlphaFold models and cryoEM data at hands, we look at this region carefully and learn that TIM motif adopts a common fold which is rare among AGC kinases and suggest RSK2 may be regulated by mTORC2, which has not been studied extensively.

Sequence alignment of the glycine-rich loop (G-loop) reveals that, in addition to the highly conserved glycines that define this loop, lysines and/or arginines are also highly conserved across these AGC kinases. Exceptions include glutamine (Q) in p90RSK (Q70 in RSK1, Q76 in RSK2, Q67 in RSK3, Q81 in RSK4), threonine 51 (T51) in human PKAα, arginine (R) in some PKC

isozymes, PKA and PKG (R260 in PKCζ, R262 in PKCι, R56 in hPKAα, and R373 in PKGIα) and valine 368 (V368) in PKGIα (Fig. 3A). The alignment also shows a highly conserved F-x$_3$-F-pT motif at the TIM motif, where these kinases are regulated by mTOR, and the presence of a serine or threonine at the turn motif for phosphorylation. The absence of a threonine at the TIM motif in kinases like PKAα, PKCδ, PKCθ, and PKCη aligns with their lack of regulation by mTOR (Fig. 3B). Although no study has shown mTORC2 regulation of RSK2, RSK3, or RSK4, the sequence homology with RSK1, which is mTOR-dependent, suggests this could be a new avenue for investigation.

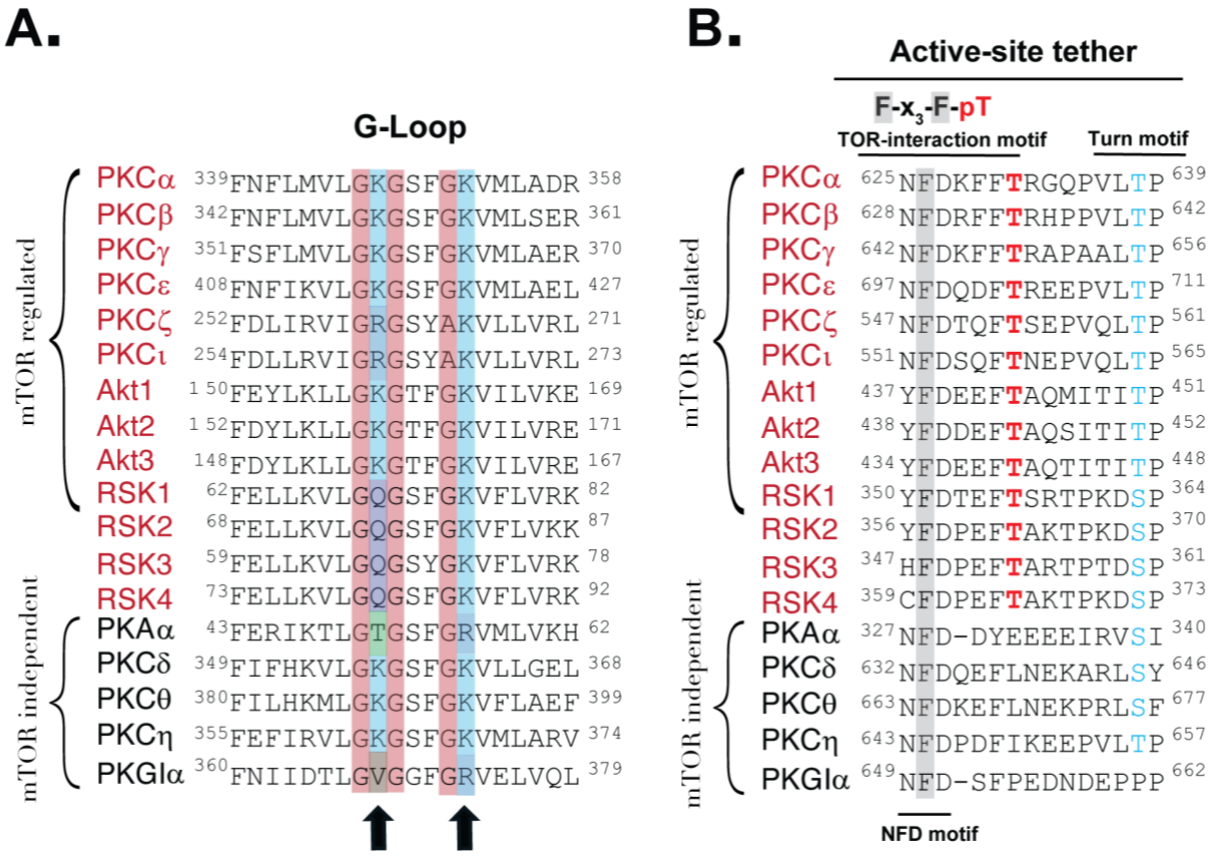
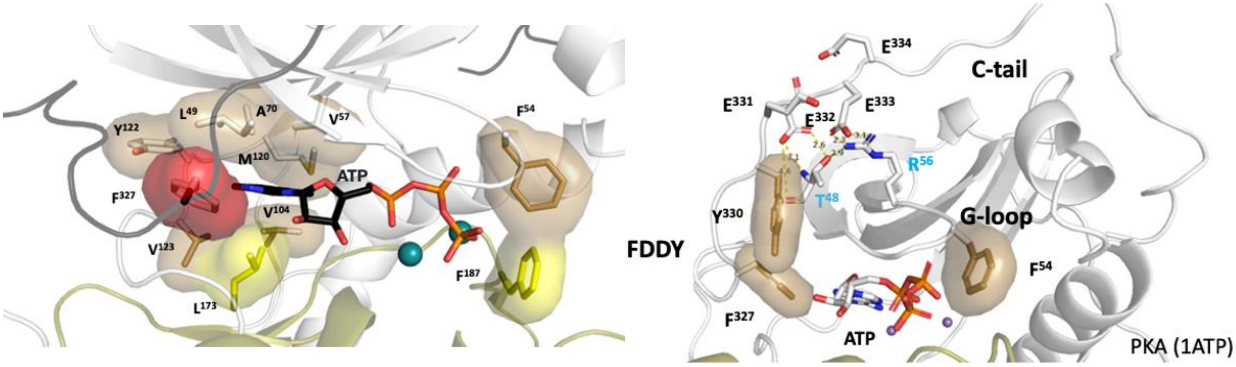


Figure 4.4: Sequence alignment of the glycine-rich loop (A) and the active site tether (B) of PKCs, AKTs, PKA*α*, and p90RSKs. **(A)** In addition to the highly conserved GxGxxG motif that defines the glycine loop, the two lysine residues or basic residues (indicated by arrows) are also conserved among these kinases. Sequence alignment of the active-site tether region in AGC kinases, highlighting.**(B)** the phosphorylation sites for the TIM are highlighted (red), turn motif (blue) and NFD motifs in various AGC kinases. Figure is adapted with some modifications from (Baffi et al., 2021)

The C-tail in AGC kinases, specifically in PKA, is highly conserved and contains many regulatory elements, such as the FDDY motif (in PKA), the turn motif, and the hydrophobic motif. The C-tail also adopts multiple conformations upon ATP binding. In the ATP-bound form, the G-loop clamps down, and the FDDY motif on the C-tail, along with other hydrophobic residues on the N- and C-lobes, forms the ATP binding pocket (Figs. 1 and 4). Additionally, R56 and T48 on

the G-loop interact with E331, E332, E333, and E334, located immediately after the TIM motif, stabilizing the closed conformation (Fig. 5). In the intermediate (committed) state (ADP-bound form), both the C-tail and G-loop adopt a partially open conformation. In the apo (uncommitted) state, the C-tail is partially disordered and swings out of place, and the G-loop is in a completely open conformation (Fig. 1, Chapter 1 Fig. 3).



^{300}TDWIAIYQRKVEAPFIPKFKGPGDTSN**FDDY**EEEEIRVSINEKCGKEFTEF^{350}

FDDY motif

<u>Figure 4.5</u>: ATP binding pocket of the PKA catalytic subunit highlighting hydrophobic residues that form the ATP binding pocket (left) and important residues on the C-tail that anchors C-tail to G-loop.

Similarly, in the apo form of p90RSK2, based on the AF2-predicted model, a TIM motif (F357 and F361) contributes to the formation of the ATP binding pocket. Residues Q76, K81, and F79 on the G-loop are primed to bind ATP and, along with K142 on the N-lobe, are positioned to interact with S369 on the turn motif upon phosphorylation (Fig. 6A). The linker adopts a different fold compared to the p90RSK:ERK complex, wrapping behind the N-lobe of the NTK. In the presence of ERK, the long linker is stabilized into a defined conformation, facilitating the interaction between ERK, CTK, and NTK (Fig. 6B). The TIM helix is present in both Alphafold

model and cryoEM structure which supports our hypothesis. This region is absent in all crystal structures and this is the first time we observe this defined fold which support our hypothesis that mTORC2 may regulate RSK2 (Chapter III, fig. 12, 13, 14).

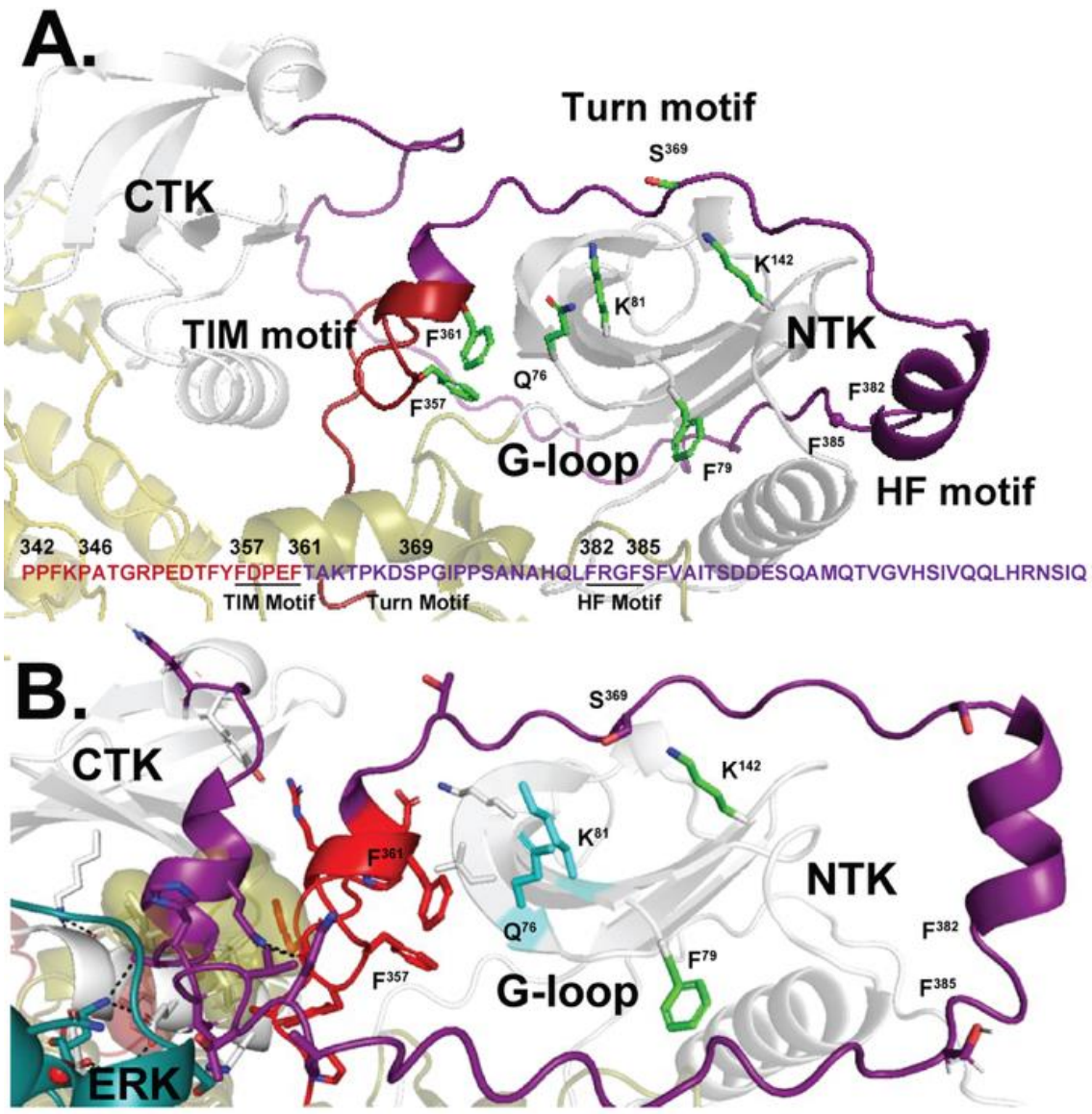


Figure 4.6: Model of p90RSK2 (A) and p90RSK2:ERK2 complex (B) in the apo state. The TIM motif is shown in red, while K81 and Q76 of the G-loop are depicted in green (top) or cyan (bottom). S369 on the turn motif is highlighted in green (top) or purple (bottom). F79 on the G-loop swings out of place, creating space for ATP binding. K142 is positioned close to S369, ready to interact once the turn motif is phosphorylated. The HF motif (F382 and F385) adopts different conformations depending on whether or not ERK is present; when ERK is not present the HF motif wrap behind the NTK (top), when ERK is around it organizes the linker and the HF motif wrap in front of NTK (bottom)

In Akt1 (PDB: 4EKK), the AMP-PNP-bound form (open state) there is a TIM helix which is predicted by the sequence analyses. The TIM motif forms the ATP binding pocket, with K158 and K163 positioned to interact with the phosphorylated C-tail. The C-tail, however, beyond the TIM motif and corresponding to the NLT, is mostly disordered (Fig. 7) and it is not disordered in PKA apo.

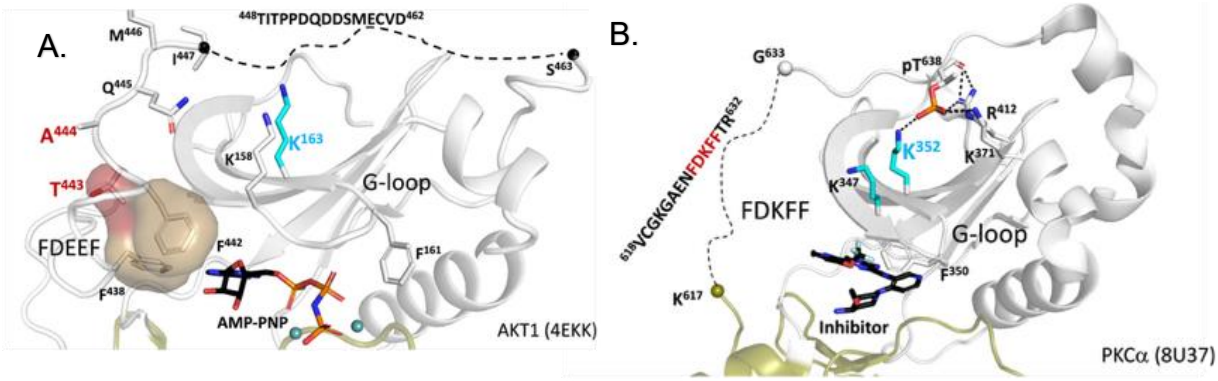


Figure 4.7: Structure of AKT1 in the AMP-PNP Bound Form (A) and Structure of the Catalytic Domain of Human PKCα in Complex with NVP-CJL037 (B). The missing density of the C-terminal tail is represented by a dashed line. The FDDY motif is shown in white, while the hydrophobic surface is depicted in tan. F438 and F442 contribute to the completion of the ATP-binding pocket. AMP-PNP is illustrated in black, orange, and blue. T443 represents the TIM phosphorylation site. (Lin et al., 2012). The structure reveals an incomplete ATP-binding pocket due to the absence of the FDDY motif on the C-tail in the crystal structure. Phosphorylated T638 is coordinated by K352 on the G-loop, as well as R412 and K371 on the N-lobe. The inhibitor is depicted in black and blue. (Visser et al., 2024)

In contrast, in the inactive conformation, when PKCα (PDB: 8U37) binds to an inhibitor, the TIM motif is disordered. Similar to apo PKA, however, the NLT is ordered. The interaction of the phosphorylated turn motif (pT638) with K352 on the G-loop and K371 and R412 on the N-lobe highlights the importance of these interactions. In another structure of inhibitor-bound PKCα (PDB: 3IW4), the TIM motif remains disordered, and the phosphorylated turn motif is coordinated by R412 on the N-lobe (Fig. 8A).

Additionally, in the ATP-bound form of PKCι (PDB: 3A8W), the TIM motif with its characteristic TIM helix forms the ATP binding pocket, with R253 and K258 on the G-loop coordinating E550 on the C-tail. It is assumed that once T548 is phosphorylated, it will flip in to form similar interactions. The phosphorylated turn motif (pT555) interacts with R318 and K277 on the N-lobe, as well as conserved basic residues on the G-loop (Fig. 8B).

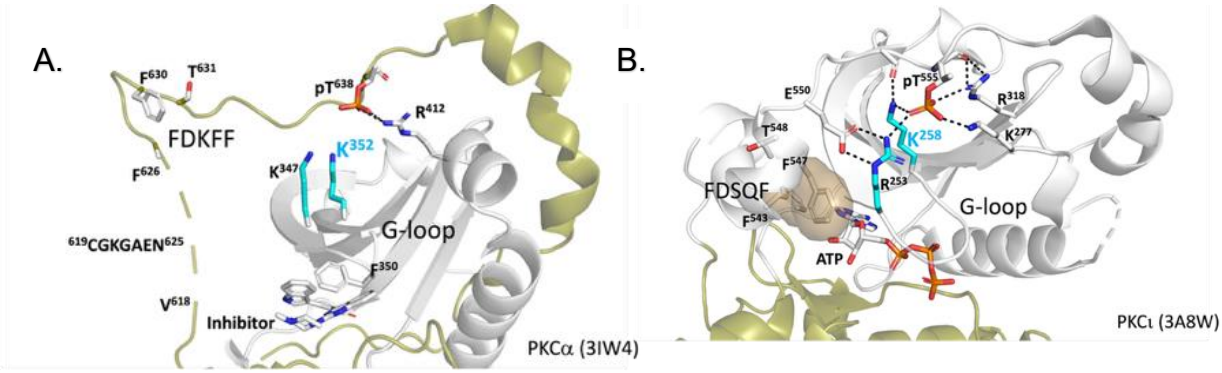


Figure 4.8: Structure of PKCα with the inhibitor (A) and structure of PKCι kinase domain in ATP bound form (B). The missing residues in the C-terminal tail are represented as CGKGAEN. The FDDY motif on the C-terminal tails is shown. F626 and F630 are positioned outside the ATP-binding pocket, and pT638 does not interact with K347 and K352 on the G-loop. As a result, the ATP-binding pocket remains incomplete, leading to an inhibited PKC kinase. (Wagner et al., 2009) . The FDDY motif is colored white, with hydrophobic residues shown in tan. F543 and F547 contribute to the ATP-binding pocket. The remaining portion of the C-terminal tail, including E550 and phosphorylated T555, is stabilized by R253 and K258 on the G-loop, as well as K277 and R318 on the N-lobe. (Takimura et al., 2010)

The TIM and FDDY motifs can also serve as an oligomeric interface. In the RIIβ tetramer structure, when ATP is absent, the β4-β5 loop of the CNB-A domain from the R subunit of another protomer packs against the FDDY motif, forming the ATP binding pocket and priming it to bind ATP and undergo phosphorylation. Upon the addition of MgATP to the crystals, phosphate

transfer occurs, capturing both ADP and the phosphorylation of the substrate (Fig. 9). For p90RSK2, the AF model predicts that ATP binding pocket is formed by the packing of CTK against the TIM or FDDY motif, positioning it to bind ATP and facilitate phosphorylation of the turn (S369) or hydrophobic motif (S386) (Fig. 6B). In the case of PKCβ, the C1B domain binds to the TIM motif (also known as the NFD motif) and rotates F629 away from the ATP binding pocket, leading to an autoinhibited state. The release of the TIM motif transitions it into the active state. The crystal structure of PKCβ (PDB: 3PFQ) also demonstrates the importance of K355 on the G-loop, as it helps coordinate pT641 at the turn motif along with K374 and R415 (Fig. 10).

These sequence alignments, structural analyses, and model assessments indicate that the interactions between phosphorylation of the TIM and turn motifs and the basic residues of the G-loop play a crucial role in sensing the open and closed conformations of AGC kinases. This, in turn, leads to either activation or inhibition of these kinases. Additionally, the TIM (or FDDY) motif serves as a critical protein-protein interaction site that regulates kinase activity. Most importantly, our analysis strongly supports the hypothesis that p90RSK has a TIM motif, which is predicted by our alpha fold and is consistent with our low resolution cryoEM structures that show density filling this space only in the RSK:ERK trimer and not in the CTK:NTK dimer (Chapter III Fig.13).

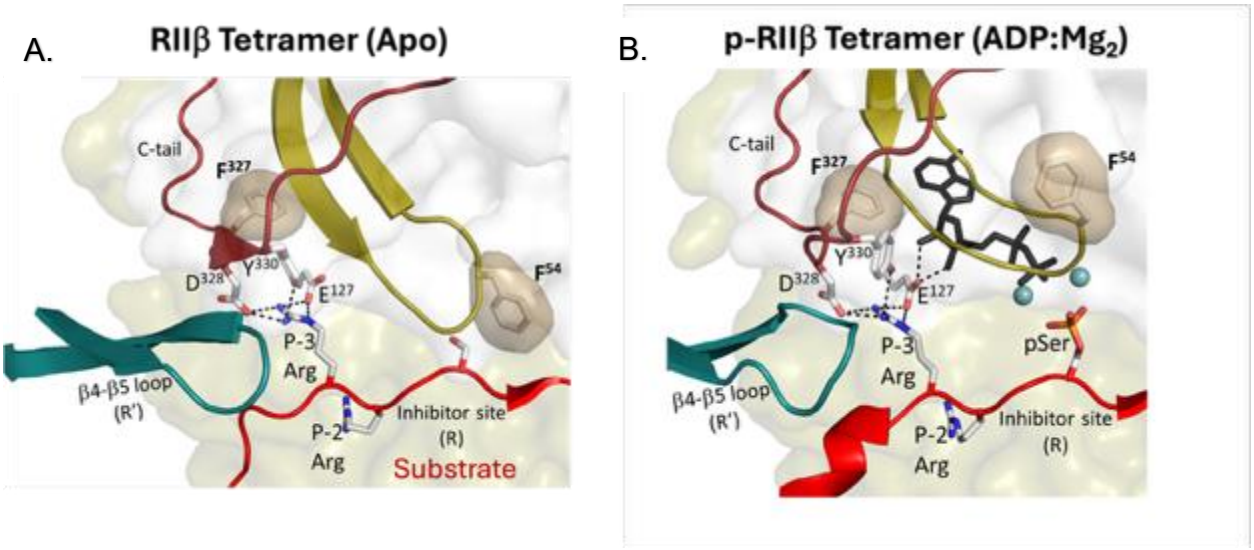


Figure 4.9. Structure of the RIIβ Holoenzyme with Both Products Captured in the Crystal Lattice (A) The tetrameric RIIβ holoenzyme consists of two R:C heterodimers. The interaction between the protomers is mediated by the β4–β5 loop within the CNB-A domain of the R-subunit and the FDDY motif located in the C-terminal tail of the C-subunit. In this tetrameric arrangement, the C-terminal tail remains in a fully closed conformation, even in the absence of a bound nucleotide. **(B)** When MgATP is introduced into the crystals, a phosphate transfer reaction takes place, leading to the stabilization of both reaction products - ADP and the phosphorylated RIIβ subunit - alongside two Mg^{2+} ions within the crystal lattice. Figure adapted from (Taylor, Zhang, Steichen, Keshwani, & Kornev, 2013)

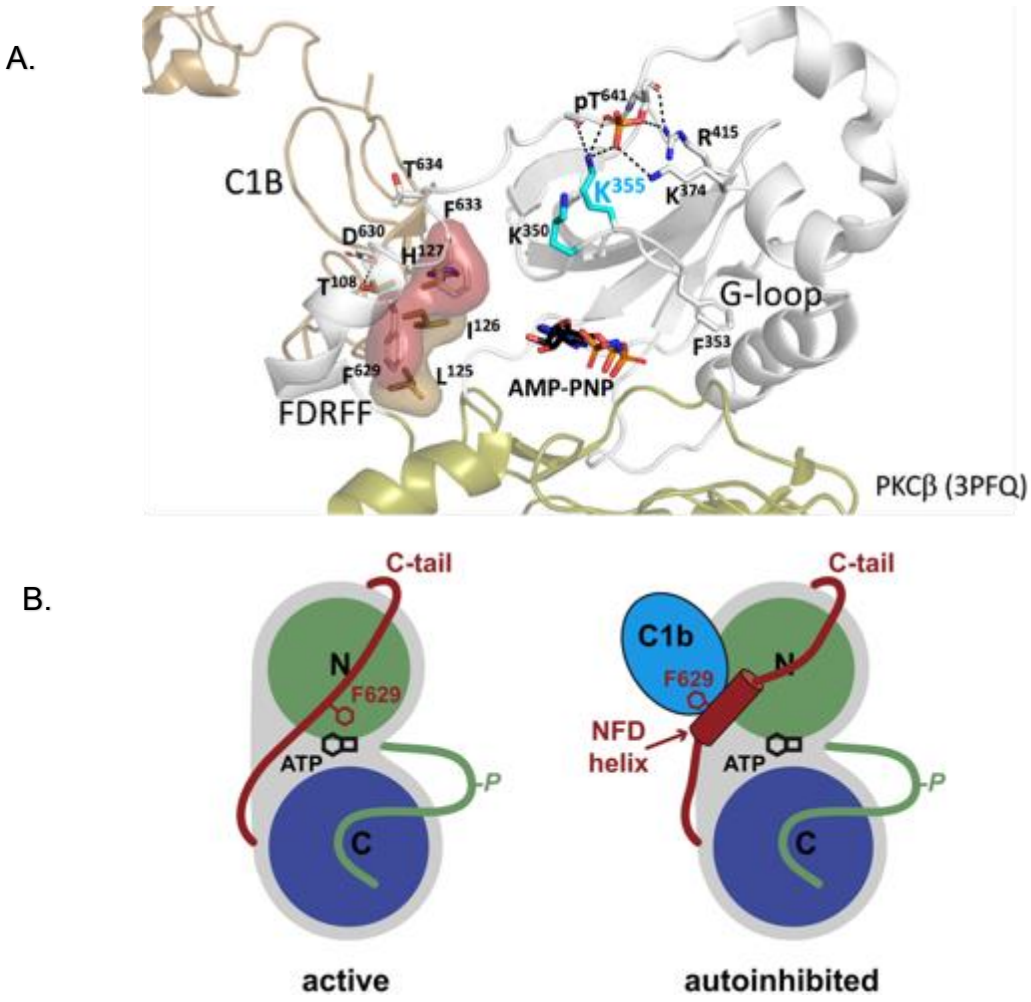


Figure 4.10. Structure of PKCβII. **(A)** The ordered portion of full-length PKCβII consists of the C1B (tan) and kinase domains. The C lobe is depicted in deep olive, while the N lobe of the kinase domain is shown in white. The FDDY motif is colored white, with hydrophobic residues highlighted in red. F629 and F633 form hydrophobic interactions with L125 and I126, while H127 on C1B and D630 in the C-terminal tail establish an ionic interaction with T108 on C1B. Phosphorylated Thr641 interacts with K355 on the glycine loop, as well as with K374 and R415. AMPPNP is represented in orange and black. F353 on the G loop adopts an open conformation. The TIM motif, which includes F629 within a helical structure, restricts its access to the ATP binding site. This helix, along with adjacent sequences, extends into the C1B diacylglycerol (DAG) binding site. **(B) Simplified Model of PKCβII Autoinhibition.** In the absence of C1B domain interaction, the NFD helix is disrupted, allowing F629 to contribute to the ATP binding site. However, when the C1B domain interacts intramolecularly, it stabilizes the NFD helix, causing F629 to rotate away from the ATP binding site, thereby inhibiting kinase activity. Figure is adapted from (Kazanietz & Lemmon, 2011)

Chapter IV, in part, is currently being prepared for submission for publication of the material. **HOANG P. M. NGUYEN**, Jian Wu, Alexandra Newton, Susan Taylor. *Key Motifs in the C-terminal Tail Contribute to ATP Binding of AGC Kinases.* The dissertation author was the primary researcher and author of this material

Chapter V

Future directions

A Introduction

Building on the structural insights and conformational models developed in this thesis, several avenues of research could further advance our understanding of the p90RSK activation mechanism. To validate key interactions and critical residues involved in this complex dynamic process, site-directed mutagenesis and biochemical assays can be employed. In parallel, computational methods could be used to test and confirm the role of specific residues - particularly in the loop or kink regions - in regulating motions of the C-terminal kinase (CTK) or N-terminal kinase (NTK) domains.

A major goal moving forward is to improve the resolution of this complex or, ideally, to solve the full-length structure of p90RSK, which has not yet been determined. Toward this end, we have initiated a collaborative effort with Dr. Anthony Kossiakoff's lab, resulting in the generation of nine Fab binders that show strong binding affinity to RSK. The workflow outlined here includes p90RSK biotinylation, followed by mass photometry and gel filtration analysis, which confirmed that three out of the nine Fabs bind effectively to RSK (Fig. 1).

Here we show data of how to make biotinylated RSK2 and preliminary data of nine binders that show high affinity and specificity with RSK2.

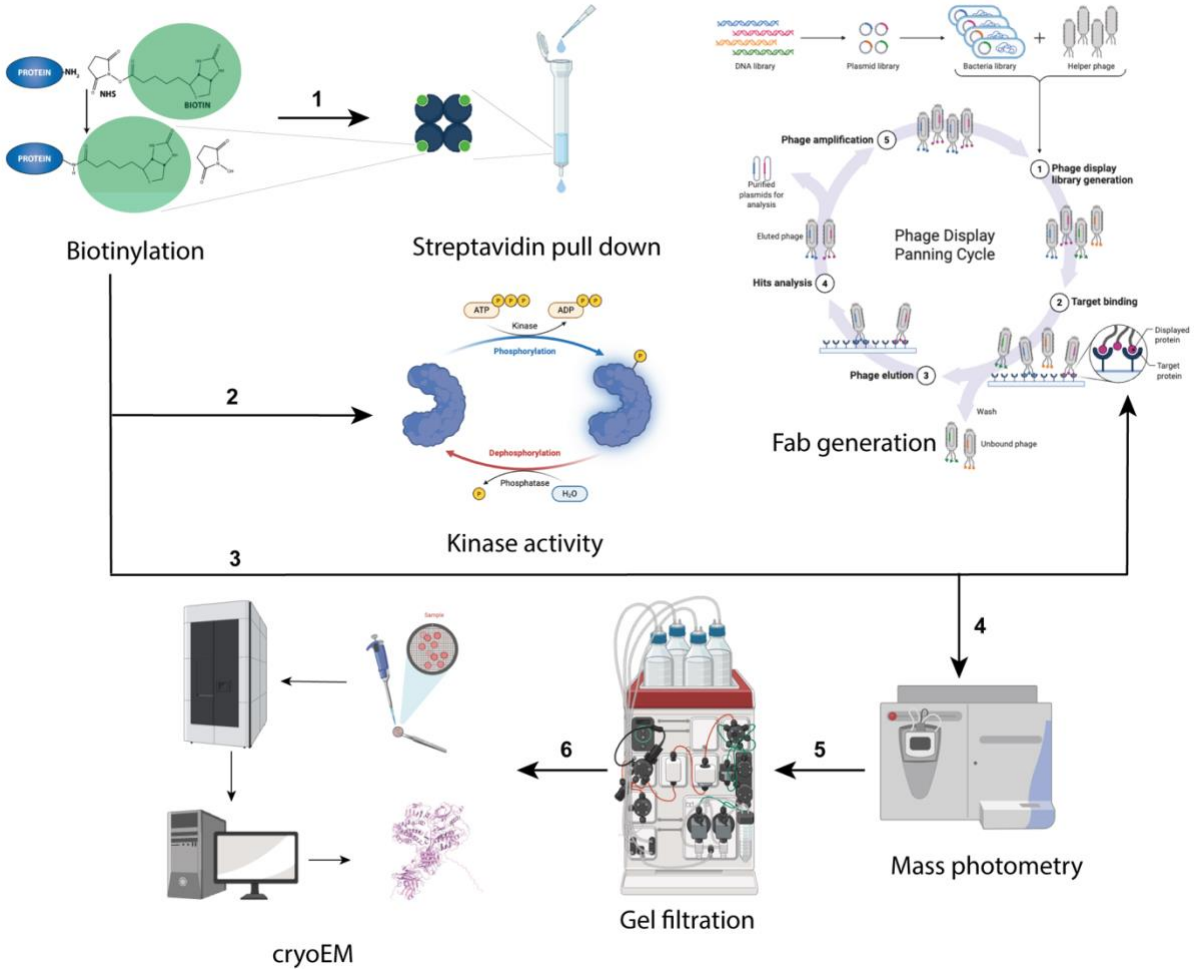


Figure 5.1: Fab generation against RSK2 and experimental workflow. (1) RSK2 is biotinylated and pulled down with Streptavidin resin to assess biotinylation efficiency. (2) Kinase activity assays are used to assess the effect of biotinylation on RSK2 function. (3) Mass photometry is used to screen complex formation conditions. (4) Gel filtration is used to form the complex. (5) Optimal conditions are used for cryo-EM sample freezing, data collection, analysis, and structure determination.

B. Preliminary results

Proteins were expressed using the *E. coli* Rosetta pLysS strain containing a pET vector. Full-length human RSK2 was produced following standard expression and purification protocols (Alexa, Gógl et al., 2015; Alexa, Sok et al., 2022). RSK2 was engineered with an N-terminal MBP tag and a C-terminal His tag, with a TEV cleavage site positioned after the MBP tag. Expression was carried out overnight, followed by harvesting and freezing of the cell pellets.

For purification, cells were lysed using a microfluidizer, and the clarified lysate was loaded onto a Ni affinity resin. The column was washed and then eluted with 250 mM imidazole. The Ni-eluted fraction was further purified using amylose resin and eluted with 10 mM maltose. To remove the MBP tag, the sample was treated with TEV protease (1:100 w/w ratio) and dialyzed overnight. The cleaved tag was separated from RSK2 through anion exchange chromatography using a HiTrap Q column. The purified protein was then concentrated and subjected to size exclusion chromatography (S200 column).

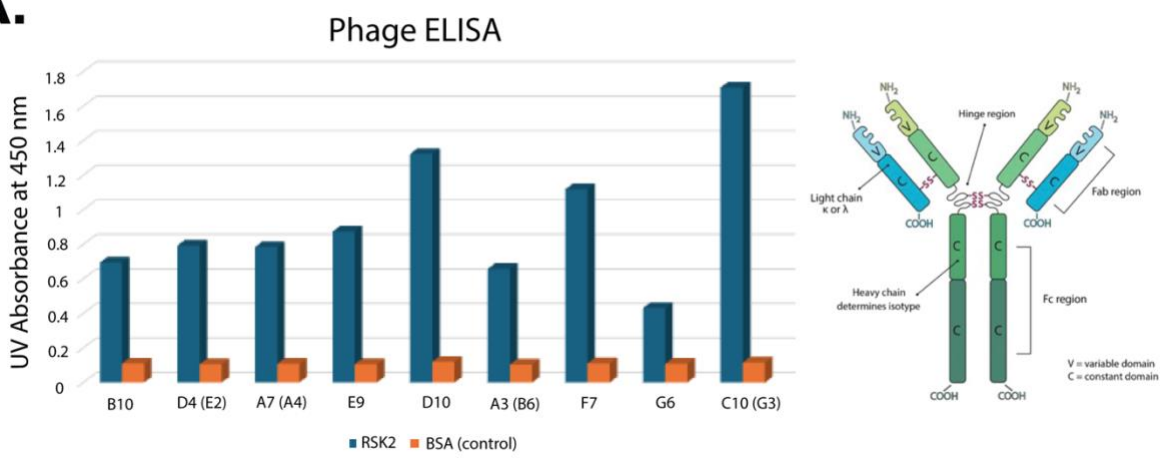
Purified RSK2 was concentrated to approximately 2 mg/mL. This protocol works best around that concentration. The biotin reagent was obtained from Tony's lab but can also be purchased from Thermo Fisher (EZ-Link™ NHS-PEG4-Biotin, Catalog # A39259). Ensure the reaction is performed in an amine-free buffer (pH 7 - 8.5), as amines may interfere with biotinylation efficiency. Prepare a 20 mM biotin reagent solution by dissolving the reagent in ultrapure water, following the manufacturer's instructions. Mix RSK2 and the biotin reagent at a 1:5 molar ratio and incubate at room temperature for 30 minutes. Quench the reaction with 1 M Tris, pH 8.0. Dialyze into HEPES buffer and freeze at - 4°C if the next step cannot be performed immediately.

To test biotinylation efficiency, a pull-down assay was performed using Streptavidin magnetic beads (Promega, Streptavidin MagneSphere Paramagnetic Particles, Catalog # Z5481). Use no more than 3 µg of beads to minimize nonspecific binding. Add biotinylated RSK2, wash three times with PBS buffer, and retain the elution fractions on the beads. Load all fractions on an SDS-PAGE gel to assess binding efficiency.

Kinase reactions were carried out in a buffer containing 50 mM Tris (pH 8), 200 mM NaCl, 5 mM DTT, 0.2% IGEPAL, 1 mM ATP, and 40 mM $MgCl_2$. RSK2 was used at a concentration of 0.5 µM in both reactions (with and without PDK1). PDK1 was used at 500 nM. ERK2 was used at 15.6 nM in the reaction with PDK1 and at 5 nM in the reaction without PDK1. Reactions were quenched with protein loading buffer supplemented with 100 mM EDTA, then boiled and subjected to SDS-PAGE. Western blots were performed to detect phosphorylation at NTK (S227), HM (S386), and CTK (T573) using corresponding antibodies. Biotinylated RSK2 that passed both tests was sent to collaborators for Fab generation.

Biotinylated RSK2 (**25 nM)** was immobilized on NeutrAvidin-coated ELISA plates. An anti-M13 HRP-conjugated antibody was used as the secondary antibody to detect binding of the clones in phage format. Figure 2 shows nine binders that exhibit specificity and high affinity for RSK2 compared to BSA (used as a control). The letter codes represent positions in the 96-well plates, and their corresponding names (Fab 1–9) are shown in **Fig. 2B.** Fabs consist of one light chain (LC, ~25 kDa) and one heavy chain (HC, ~25 kDa), and form part of an antibody that recognizes antigens **(Fig. 2A). Fig. 2B** shows the sequences of H1, H2, and H3 regions of the heavy chains (HCs).

A.



B.

Phage ID	Fab ID	CDR-H1	CDR-H2	CDR-H3
B10	Fab1	LYSSSI	SISPYSGYTY	AAPSSYYRWGLHAILPGF
D4 (E2)	Fab2	IYSYSI	SIYPSSGYTY	EYWKAYNSMYWLQYMYAM
A7 (A4)	Fab3	LYSSYI	YIYPSYGSTS	EYYRKGTHYYSYSWAF
E9	Fab4	ISSSSI	SIYSYSGSTY	EYYWWGNYFYHYGYAL
D10	Fab5	VYSSSI	YISPYSGYTS	VGYQMSGSYFYKWGGF
A3 (B6)	Fab6	IYSSSI	SIYSSSGSTY	YHYSPYVYWQSGYQAL
F7	Fab7	VYSSYI	SIYPYSGYTS	YLYTSIGSWYRYGHAL
G6	Fab8	VYSSSI	SIYSYYGSTS	YSYLYYSARYQRIGGL
C10 (G3)	Fab9	FSSSSI	SISSSSGSTS	YYYWQGKSSNFWSSRYAL

Figure 5.2: Characterization of nine Fab candidates with high affinity and specificity for RSK2. (A) Binding affinities of the nine Fabs to RSK2, measured by UV absorbance and schematic representation of an antibody and where Fabs regions are. **(B)** Sequences of the CDR-H1, CDR-H2, and CDR-H3 regions of the nine Fabs.

For mass photometry, standards were loaded with molecular weights within the expected range for RSK2 and Fabs to establish a standard curve. Mix Fabs and RSK2 at a 1:1 molar ratio, incubate at room temperature for 15 minutes, then added onto a droplet for mass photometry to determine the molecular weights present.

Mass photometry shows that Fab1, Fab5, and Fab9 bind strongly to non-biotinylated RSK2 in solution at a 1:1 ratio (Fig. 3A). The gel filtration chromatogram of Fab1, Fab5, and Fab9 also

demonstrates strong binding to non-biotinylated RSK2 (Fig. 3B), which is further confirmed by SDS_PAGE gel (Fig. 3C).

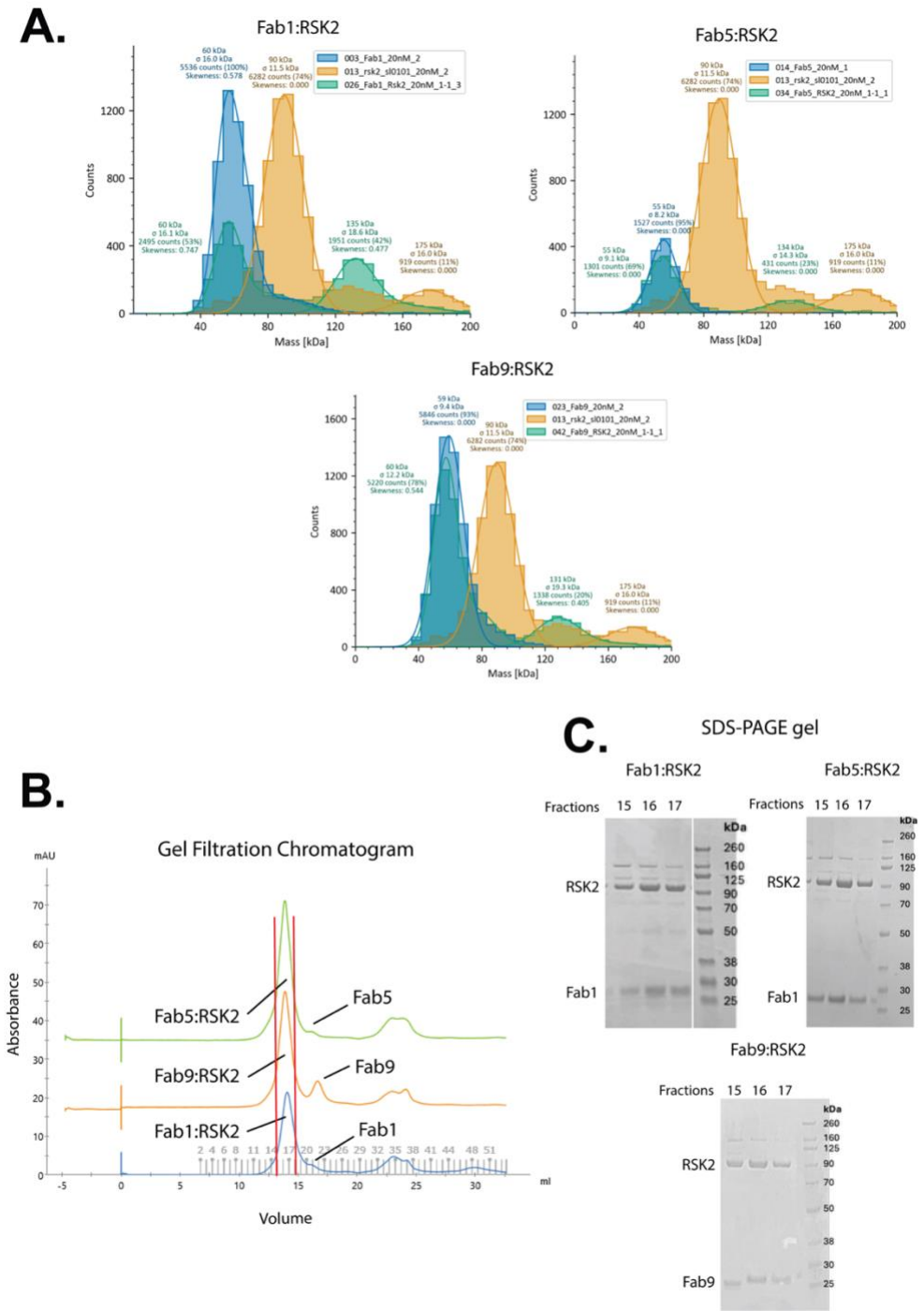


Figure 5.3: Complex formation of Fab1, Fab5, and Fab9 with RSK2. (A) Mass photometry results showing complex formation of Fab1, Fab5, and Fab9 with RSK2. **(B)** Gel filtration chromatograms of the Fab–RSK2 complexes. **(C)** SDS-PAGE of fractions 15, 16, 17 of the purified complexes of Fab1, Fab5, and Fab9 with RSK2.

The immediate next steps involve completing binding validation for all Fab candidates, followed by grid freezing, screening, and cryo-EM data collection once optimal conditions are established. Additionally, we will try the new AF version, which will allow us to explore the effects of phosphorylation on the conformation of the NTK and the organization of the C-tail in RSK2 by itself vs. the RSK2:ERK2 complex.

Chapter V contains unpublished material coauthored with Jian Wu, Susan Taylor. The dissertation author was the primary author of this chapter.

References

Akamine, P., Madhusudan, Wu, J., Xuong, N.-H., Eyck, L. F. T., & Taylor, S. S. (2003). Dynamic Features of cAMP-dependent Protein Kinase Revealed by Apoenzyme Crystal Structure. *Journal of Molecular Biology*, *327*(1), 159–171. doi: 10.1016/s0022-2836(02)01446-8

Akdel, M., Pires, D. E. V., Pardo, E. P., Jänes, J., Zalevsky, A. O., Mészáros, B., … Beltrao, P. (2022). A structural biology community assessment of AlphaFold2 applications. *Nature Structural & Molecular Biology*, *29*(11), 1056–1067. doi: 10.1038/s41594-022-00849-w

Alderson, T. R., Pritišanac, I., Moses, A. M., & Forman-Kay, J. D. (2022). Systematic identification of conditionally folded intrinsically disordered regions by AlphaFold2. *BioRxiv*, 2022.02.18.481080. doi: 10.1101/2022.02.18.481080

Alexa, A., Gógl, G., Glatz, G., Garai, Á., Zeke, A., Varga, J., … Reményi, A. (2015). Structural assembly of the signaling competent ERK2–RSK1 heterodimeric protein kinase complex. *Proceedings of the National Academy of Sciences*, *112*(9), 2711–2716. doi: 10.1073/pnas.1417571112

Alexa, A., Sok, P., Gross, F., Albert, K., Kobori, E., Póti, Á. L., … Reményi, A. (2022). A non-catalytic herpesviral protein reconfigures ERK-RSK signaling by targeting kinase docking systems in the host. *Nature Communications*, *13*(1), 472. doi: 10.1038/s41467-022-28109-x

Anjum, R., & Blenis, J. (2008). The RSK family of kinases: emerging roles in cellular signalling. *Nature Reviews Molecular Cell Biology*, *9*(10), 747–758. doi: 10.1038/nrm2509

Arencibia, J. M., Pastor-Flores, D., Bauer, A. F., Schulze, J. O., & Biondi, R. M. (2013). AGC protein kinases: From structural mechanism of regulation to allosteric drug development for the treatment of human diseases. *Biochimica et Biophysica Acta (BBA) - Proteins and Proteomics*, *1834*(7), 1302–1321. doi: 10.1016/j.bbapap.2013.03.010

Aronchik, I., Appleton, B. A., Basham, S. E., Crawford, K., Rosario, M. D., Doyle, L. V., … Jefferson, A. B. (2014). Novel Potent and Selective Inhibitors of p90 Ribosomal S6 Kinase Reveal the Heterogeneity of RSK Function in MAPK-Driven Cancers. *Molecular Cancer Research*, *12*(5), 803–812. doi: 10.1158/1541-7786.mcr-13-0595

Baffi, T. R., Lordén, G., Wozniak, J. M., Feichtner, A., Yeung, W., Kornev, A. P., … Newton, A. C. (2021). mTORC2 controls the activity of PKC and Akt by phosphorylating a conserved TOR interaction motif. *Science Signaling*, *14*(678). doi: 10.1126/scisignal.abe4509

Baffi, T. R., & Newton, A. C. (2022). mTOR Regulation of AGC Kinases: New Twist to an Old Tail. *Molecular Pharmacology*, *101*(4), 213–218. doi: 10.1124/molpharm.121.000310

Bai, X., McMullan, G., & Scheres, S. H. W. (2015). How cryo-EM is revolutionizing structural biology. *Trends in Biochemical Sciences*, *40*(1), 49–57. doi: 10.1016/j.tibs.2014.10.005

Balasuriya, N., Kunkel, M. T., Liu, X., Biggar, K. K., Li, S. S.-C., Newton, A. C., & O'Donoghue, P. (2018). Genetic code expansion and live cell imaging reveal that Thr-308 phosphorylation is irreplaceable and sufficient for Akt1 activity. *Journal of Biological Chemistry*, *293*(27), 10744–10756. doi: 10.1074/jbc.ra118.002357

Barker, W. C., & Dayhoff, M. O. (1982). Viral src gene products are related to the catalytic chain of mammalian cAMP-dependent protein kinase. *Proceedings of the National Academy of Sciences*, *79*(9), 2836–2839. doi: 10.1073/pnas.79.9.2836

Biondi, R. M., Cheung, P. C. F., Casamayor, A., Deak, M., Currie, R. A., & Alessi, D. R. (2000). Identification of a pocket in the PDK1 kinase domain that interacts with PIF and the C-terminal residues of PKA. *The EMBO Journal*, *19*(5), 979–988. doi: 10.1093/emboj/19.5.979

Bj⊘rbæk, C., Zhao, Y., & Moller, D. E. (1995). Divergent Functional Roles for p90 rsk Kinase Domains (∗). *Journal of Biological Chemistry*, *270*(32), 18848–18852. doi: 10.1074/jbc.270.32.18848

Bornancin, F., & Parker, P. J. (1996). Phosphorylation of threonine 638 critically controls the dephosphorylation and inactivation of protein kinase Cα. *Current Biology*, *6*(9), 1114–1123. doi: 10.1016/s0960-9822(02)70678-7

Bryant, P., Pozzati, G., & Elofsson, A. (2022). Improved prediction of protein-protein interactions using AlphaFold2. *Nature Communications*, *13*(1), 1265. doi: 10.1038/s41467-022-28865-w

Cai, R., & Minteer, S. D. (2018). Nitrogenase Bioelectrocatalysis: From Understanding Electron-Transfer Mechanisms to Energy Applications. *ACS Energy Letters*, *3*(11), 2736–2742. doi: 10.1021/acsenergylett.8b01637

Callaway, E. (2022). What's next for AlphaFold and the AI protein-folding revolution. *Nature*, *604*(7905), 234–238. doi: 10.1038/d41586-022-00997-5

Canagarajah, B. J., Khokhlatchev, A., Cobb, M. H., & Goldsmith, E. J. (1997). Activation Mechanism of the MAP Kinase ERK2 by Dual Phosphorylation. *Cell*, *90*(5), 859–869. doi: 10.1016/s0092-8674(00)80351-7

Cargnello, M., & Roux, P. P. (2011). Activation and Function of the MAPKs and Their Substrates, the MAPK-Activated Protein Kinases. *Microbiology and Molecular Biology Reviews*, *75*(1), 50–83. doi: 10.1128/mmbr.00031-10

Chang, C.-W. M., Wang, S.-C., Wang, C.-H., Pang, A. H., Yang, C.-H., Chang, Y.-K., … Tsai, M.-D. (2024). A unified view on enzyme catalysis by cryo-EM study of a DNA topoisomerase. *Communications Chemistry*, *7*(1), 45. doi: 10.1038/s42004-024-01129-y

Chen, J., Noble, A. J., Kang, J. Y., & Darst, S. A. (2019). Eliminating effects of particle adsorption to the air/water interface in single-particle cryo-electron microscopy: Bacterial RNA

polymerase and CHAPSO. *Journal of Structural Biology: X*, *1*, 100005. doi: 10.1016/j.yjsbx.2019.100005

Cheng, Y. (2018). Single-particle cryo-EM—How did it get here and where will it go. *Science*, *361*(6405), 876–880. doi: 10.1126/science.aat4346

Chou, P.-C., Rajput, S., Zhao, X., Patel, C., Albaciete, D., Oh, W. J., … Jacinto, E. (2020). mTORC2 Is Involved in the Induction of RSK Phosphorylation by Serum or Nutrient Starvation. *Cells*, *9*(7), 1567. doi: 10.3390/cells9071567

Chu, N., Salguero, A. L., Liu, A. Z., Chen, Z., Dempsey, D. R., Ficarro, S. B., … Cole, P. A. (2018). Akt Kinase Activation Mechanisms Revealed Using Protein Semisynthesis. *Cell*, *174*(4), 897-907.e14. doi: 10.1016/j.cell.2018.07.003

Cohen, P. (2002). The origins of protein phosphorylation. *Nature Cell Biology*, *4*(5), E127–E130. doi: 10.1038/ncb0502-e127

Costales, A., Mathur, M., Ramurthy, S., Lan, J., Subramanian, S., Jain, R., … Shafer, C. M. (2014). 2-Amino-7-substituted benzoxazole analogs as potent RSK2 inhibitors. *Bioorganic & Medicinal Chemistry Letters*, *24*(6), 1592–1596. doi: 10.1016/j.bmcl.2014.01.058

Dalby, K. N., Morrice, N., Caudwell, F. B., Avruch, J., & Cohen, P. (1998). Identification of Regulatory Phosphorylation Sites in Mitogen-activated Protein Kinase (MAPK)-activated Protein Kinase-1a/p90 rsk That Are Inducible by MAPK*. *Journal of Biological Chemistry*, *273*(3), 1496–1505. doi: 10.1074/jbc.273.3.1496

Davey, N. E., Cyert, M. S., & Moses, A. M. (2015). Short linear motifs – ex nihilo evolution of protein regulation. *Cell Communication and Signaling*, *13*(1), 43. doi: 10.1186/s12964-015-0120-z

Depelteau, J. S., Koning, G., Yang, W., & Briegel, A. (2020). An Economical, Portable Manual Cryogenic Plunge Freezer for the Preparation of Vitrified Biological Samples for Cryogenic Electron Microscopy. *Microscopy and Microanalysis*, *26*(3), 413--418. doi: 10.1017/s1431927620001385

Devang, N., Pani, A., & Rajanikant, G. K. (2020). Pseudokinases: Prospects for expanding the therapeutic targets armamentarium. *Advances in Protein Chemistry and Structural Biology*, *124*, 121–185. doi: 10.1016/bs.apcsb.2020.09.004

Dill, K. A., Ozkan, S. B., Shell, M. S., & Weikl, T. R. (2008). The Protein Folding Problem. *Annual Review of Biophysics*, *37*(1), 289–316. doi: 10.1146/annurev.biophys.37.092707.153558

Dümmler, B. A., Hauge, C., Silber, J., Yntema, H. G., Kruse, L. S., Kofoed, B., … Frödin, M. (2005). Functional Characterization of Human RSK4, a New 90-kDa Ribosomal S6 Kinase, Reveals Constitutive Activation in Most Cell Types*. *Journal of Biological Chemistry*, *280*(14), 13304–13314. doi: 10.1074/jbc.m408194200

Dutil, E. M., Toker, A., & Newton, A. C. (1998). Regulation of conventional protein kinase C isozymes by phosphoinositide-dependent kinase 1 (PDK-1). *Current Biology*, *8*(25), 1366–1375. doi: 10.1016/s0960-9822(98)00017-7

Edwards, A. S., & Newton, A. C. (1997). Phosphorylation at Conserved Carboxyl-terminal Hydrophobic Motif Regulates the Catalytic and Regulatory Domains of Protein Kinase C*. *Journal of Biological Chemistry*, *272*(29), 18382–18390. doi: 10.1074/jbc.272.29.18382

Evans, R., O'Neill, M., Pritzel, A., Antropova, N., Senior, A., Green, T., … Hassabis, D. (2022). Protein complex prediction with AlphaFold-Multimer. *BioRxiv*, 2021.10.04.463034. doi: 10.1101/2021.10.04.463034

Facchinetti, V., Ouyang, W., Wei, H., Soto, N., Lazorchak, A., Gould, C., … Jacinto, E. (2008). The mammalian target of rapamycin complex 2 controls folding and stability of Akt and protein kinase C. *The EMBO Journal*, *27*(14), 1932–1943. doi: 10.1038/emboj.2008.120

Faezov, B., & Dunbrack, R. L. (2023). AlphaFold2 models of the active form of all 437 catalytically competent human protein kinase domains. *BioRxiv*, 2023.07.21.550125. doi: 10.1101/2023.07.21.550125

Fisher, T. L., & Blenis, J. (1996). Evidence for Two Catalytically Active Kinase Domains in pp90 rsk. *Molecular and Cellular Biology*, *16*(3), 1212–1219. doi: 10.1128/mcb.16.3.1212

Frank, J. (2017). Advances in the field of single-particle cryo-electron microscopy over the last decade. *Nature Protocols*, *12*(2), 209–212. doi: 10.1038/nprot.2017.004

Garai, Á., Zeke, A., Gógl, G., Törő, I., Fördős, F., Blankenburg, H., … Reményi, A. (2012). Specificity of Linear Motifs That Bind to a Common Mitogen-Activated Protein Kinase Docking Groove. *Science Signaling*, *5*(245), ra74. doi: 10.1126/scisignal.2003004

Georgescauld, F., Wales, T. E., & Engen, J. R. (2019). Hydrogen deuterium exchange mass spectrometry applied to chaperones and chaperone-assisted protein folding. *Expert Review of Proteomics*, *16*(7), 613–625. doi: 10.1080/14789450.2019.1633920

Gibbs, C. S., & Zoller, M. J. (1991). Rational scanning mutagenesis of a protein kinase identifies functional regions involved in catalysis and substrate interactions. *Journal of Biological Chemistry*, *266*(14), 8923–8931. doi: 10.1016/s0021-9258(18)31532-1

Gógl, G., Biri-Kovács, B., Durbesson, F., Jane, P., Nomine, Y., Kostmann, C., … Nyitray, L. (2019). Rewiring of RSK–PDZ Interactome by Linear Motif Phosphorylation. *Journal of Molecular Biology*, *431*(6), 1234–1249. doi: 10.1016/j.jmb.2019.01.038

Gógl, G., Biri-Kovács, B., Póti, Á. L., Vadászi, H., Szeder, B., Bodor, A., … Reményi, A. (2018). Dynamic control of RSK complexes by phosphoswitch-based regulation. *The FEBS Journal*, *285*(1), 46–71. doi: 10.1111/febs.14311

Gógl, G., Kornev, A. P., Reményi, A., & Taylor, S. S. (2019). Disordered Protein Kinase Regions in Regulation of Kinase Domain Cores. *Trends in Biochemical Sciences*, *44*(4), 300–311. doi: 10.1016/j.tibs.2018.12.002

Good, J. A. L., Ziegler, W. H., Parekh, D. B., Alessi, D. R., Cohen, P., & Parker, P. J. (1998). Protein Kinase C Isotypes Controlled by Phosphoinositide 3-Kinase Through the Protein Kinase PDK1. *Science*, *281*(5385), 2042–2045. doi: 10.1126/science.281.5385.2042

Han, Y., Fan, X., Wang, H., Zhao, F., Tully, C. G., Kong, J., … Yan, N. (2020). High-yield monolayer graphene grids for near-atomic resolution cryoelectron microscopy. *Proceedings of the National Academy of Sciences*, *117*(2), 1009--1014. doi: 10.1073/pnas.1919114117

Hari, S. B., Merritt, E. A., & Maly, D. J. (2013). Sequence Determinants of a Specific Inactive Protein Kinase Conformation. *Chemistry & Biology*, *20*(6), 806–815. doi: 10.1016/j.chembiol.2013.05.005

Herzik, M. A., Wu, M., & Lander, G. C. (2019). High-resolution structure determination of sub-100 kDa complexes using conventional cryo-EM. *Nature Communications*, *10*(1), 1032. doi: 10.1038/s41467-019-08991-8

Ikenoue, T., Inoki, K., Yang, Q., Zhou, X., & Guan, K. (2008). Essential function of TORC2 in PKC and Akt turn motif phosphorylation, maturation and signalling. *The EMBO Journal*, *27*(14), 1919–1931. doi: 10.1038/emboj.2008.119

Ikuta, M., Kornienko, M., Byrne, N., Reid, J. C., Mizuarai, S., Kotani, H., & Munshi, S. K. (2007). Crystal structures of the N-terminal kinase domain of human RSK1 bound to three different ligands: Implications for the design of RSK1 specific inhibitors. *Protein Science*, *16*(12), 2626–2635. doi: 10.1110/ps.073123707

Jain, R., Mathur, M., Lan, J., Costales, A., Atallah, G., Ramurthy, S., … Shafer, C. M. (2015). Discovery of Potent and Selective RSK Inhibitors as Biological Probes. *Journal of Medicinal Chemistry*, *58*(17), 6766–6783. doi: 10.1021/acs.jmedchem.5b00450

Jain, T., Sheehan, P., Crum, J., Carragher, B., & Potter, C. S. (2012). Spotiton: A prototype for an integrated inkjet dispense and vitrification system for cryo-TEM. *Journal of Structural Biology*, *179*(1), 68--75. doi: 10.1016/j.jsb.2012.04.020

Jensen, C. J., Buch, M.-B., Krag, T. O., Hemmings, B. A., Gammeltoft, S., & Frödin, M. (1999). 90-kDa Ribosomal S6 Kinase Is Phosphorylated and Activated by 3-Phosphoinositide-dependent Protein Kinase-1*. *Journal of Biological Chemistry*, *274*(38), 27168–27176. doi: 10.1074/jbc.274.38.27168

Jones, S. W., Erikson, E., Blenis, J., Maller, J. L., & Erikson, R. L. (1988). A Xenopus ribosomal protein S6 kinase has two apparent kinase domains that are each similar to distinct protein kinases. *Proceedings of the National Academy of Sciences*, *85*(10), 3377–3381. doi: 10.1073/pnas.85.10.3377

Josephs, T. M., Belousoff, M. J., Liang, Y.-L., Piper, S. J., Cao, J., Garama, D. J., … Sexton, P. M. (2021). Structure and dynamics of the CGRP receptor in apo and peptide-bound forms. *Science*, eabf7258. doi: 10.1126/science.abf7258

Jumper, J., Evans, R., Pritzel, A., Green, T., Figurnov, M., Ronneberger, O., … Hassabis, D. (2021). Highly accurate protein structure prediction with AlphaFold. *Nature*, *596*(7873), 583–589. doi: 10.1038/s41586-021-03819-2

Kannan, N., Haste, N., Taylor, S. S., & Neuwald, A. F. (2007). The hallmark of AGC kinase functional divergence is its C-terminal tail, a cis-acting regulatory module. *Proceedings of the National Academy of Sciences*, *104*(4), 1272–1277. doi: 10.1073/pnas.0610251104

Kazanietz, M. G., & Lemmon, M. A. (2011). Protein Kinase C Regulation: C1 Meets C-tail. *Structure*, *19*(2), 144–146. doi: 10.1016/j.str.2011.01.004

Keranen, L. M., Dutil, E. M., & Newton, A. C. (1995). Protein kinase C is regulated in vivo by three functionally distinct phosphorylations. *Current Biology*, *5*(12), 1394–1403. doi: 10.1016/s0960-9822(95)00277-6

Knighton, D. R., Zheng, J., Eyck, L. F. T., Ashford, V. A., Xuong, N.-H., Taylor, S. S., & Sowadski, J. M. (1991). Crystal Structure of the Catalytic Subunit of Cyclic Adenosine Monophosphate-Dependent Protein Kinase. *Science*, *253*(5018), 407–414. doi: 10.1126/science.1862342

Kopcho, N., Chang, G., & Komives, E. A. (2019). Dynamics of ABC Transporter P-glycoprotein in Three Conformational States. *Scientific Reports*, *9*(1), 15092. doi: 10.1038/s41598-019-50578-2

Kornev, A. P., Haste, N. M., Taylor, S. S., & Eyck, L. F. T. (2006). Surface comparison of active and inactive protein kinases identifies a conserved activation mechanism. *Proceedings of the National Academy of Sciences*, *103*(47), 17783–17788. doi: 10.1073/pnas.0607656103

Kornev, A. P., & Taylor, S. S. (2015). Dynamics-Driven Allostery in Protein Kinases. *Trends in Biochemical Sciences*, *40*(11), 628–647. doi: 10.1016/j.tibs.2015.09.002

Kornev, A. P., Taylor, S. S., & Eyck, L. F. T. (2008). A helix scaffold for the assembly of active protein kinases. *Proceedings of the National Academy of Sciences*, *105*(38), 14377–14382. doi: 10.1073/pnas.0807988105

Krebs, E. G. (1998). AN ACCIDENTAL BIOCHEMIST. *Annual Review of Biochemistry*, *67*(1), 1–21. doi: 10.1146/annurev.biochem.67.1.0

Kühlbrandt, W. (2014). The Resolution Revolution. *Science*, *343*(6178), 1443–1444. doi: 10.1126/science.1251652

Lavoie, H., Gagnon, J., & Therrien, M. (2020). ERK signalling: a master regulator of cell behaviour, life and fate. *Nature Reviews Molecular Cell Biology*, *21*(10), 607–632. doi: 10.1038/s41580-020-0255-7

Lin, K., Lin, J., Wu, W.-I., Ballard, J., Lee, B. B., Gloor, S. L., … Brandhuber, B. J. (2012). An ATP-Site On-Off Switch That Restricts Phosphatase Accessibility of Akt. *Science Signaling*, *5*(223), ra37. doi: 10.1126/scisignal.2002618

Liu, R.-Y., Zhang, Y., Smolen, P., Cleary, L. J., & Byrne, J. H. (2022). Defective synaptic plasticity in a model of Coffin–Lowry syndrome is rescued by simultaneously targeting PKA and MAPK pathways. *Learning & Memory*, *29*(12), 435–446. doi: 10.1101/lm.053625.122

Lu, T.-W., Aoto, P. C., Weng, J.-H., Nielsen, C., Cash, J. N., Hall, J., … Taylor, S. S. (2020). Structural analyses of the PKA RIIβ holoenzyme containing the oncogenic DnaJB1-PKAc fusion protein reveal protomer asymmetry and fusion-induced allosteric perturbations in fibrolamellar hepatocellular carcinoma. *PLoS Biology*, *18*(12), e3001018. doi: 10.1371/journal.pbio.3001018

Lu, T.-W., Wu, J., Aoto, P. C., Weng, J.-H., Ahuja, L. G., Sun, N., … Taylor, S. S. (2019). Two PKA RIα holoenzyme states define ATP as an isoform-specific orthosteric inhibitor that competes with the allosteric activator, cAMP. *Proceedings of the National Academy of Sciences*, *116*(33), 16347–16356. doi: 10.1073/pnas.1906036116

Lumpkin, R. J., Baker, R. W., Leschziner, A. E., & Komives, E. A. (2020). Structure and dynamics of the ASB9 CUL-RING E3 Ligase. *Nature Communications*, *11*(1), 2866. doi: 10.1038/s41467-020-16499-9

Lumpkin, R. J., & Komives, E. A. (2019). DECA, A Comprehensive, Automatic Post-processing Program for HDX-MS Data*. *Molecular & Cellular Proteomics*, *18*(12), 2516–2523. doi: 10.1074/mcp.tir119.001731

Lyumkis, D. (2019). Challenges and Opportunities in Cryo-EM Single-Particle Analysis. *Journal of Biological Chemistry*, jbc.REV118.005602. doi: 10.1074/jbc.rev118.005602

Malakhova, M., Kurinov, I., Liu, K., Zheng, D., D'Angelo, I., Shim, J.-H., … Dong, Z. (2009). Structural Diversity of the Active N-Terminal Kinase Domain of p90 Ribosomal S6 Kinase 2. *PLoS ONE*, *4*(11), e8044. doi: 10.1371/journal.pone.0008044

Malakhova, M., Tereshko, V., Lee, S.-Y., Yao, K., Cho, Y.-Y., Bode, A., & Dong, Z. (2008). Structural basis for activation of the autoinhibitory C-terminal kinase domain of p90 RSK2. *Nature Structural & Molecular Biology*, *15*(1), 112–113. doi: 10.1038/nsmb1347

Manning, G., Whyte, D. B., Martinez, R., Hunter, T., & Sudarsanam, S. (2002). The Protein Kinase Complement of the Human Genome. *Science*, *298*(5600), 1912–1934. doi: 10.1126/science.1075762

Masson, G. R., Burke, J. E., Ahn, N. G., Anand, G. S., Borchers, C., Brier, S., … Rand, K. D. (2019). Recommendations for performing, interpreting and reporting hydrogen deuterium exchange mass spectrometry (HDX-MS) experiments. *Nature Methods*, *16*(7), 595–602. doi: 10.1038/s41592-019-0459-y

Masterson, L. R., Shi, L., Metcalfe, E., Gao, J., Taylor, S. S., & Veglia, G. (2011). Dynamically committed, uncommitted, and quenched states encoded in protein kinase A revealed by NMR spectroscopy. *Proceedings of the National Academy of Sciences*, *108*(17), 6969–6974. doi: 10.1073/pnas.1102701108

Mirdita, M., Schütze, K., Moriwaki, Y., Heo, L., Ovchinnikov, S., & Steinegger, M. (2022a). ColabFold - Making protein folding accessible to all. *BioRxiv*, 2021.08.15.456425. doi: 10.1101/2021.08.15.456425

Mirdita, M., Schütze, K., Moriwaki, Y., Heo, L., Ovchinnikov, S., & Steinegger, M. (2022b). ColabFold: making protein folding accessible to all. *Nature Methods*, *19*(6), 679–682. doi: 10.1038/s41592-022-01488-1

Möbitz, H. (2015). The ABC of protein kinase conformations. *Biochimica et Biophysica Acta (BBA) - Proteins and Proteomics*, *1854*(10), 1555–1566. doi: 10.1016/j.bbapap.2015.03.009

Modi, V., & Dunbrack, R. L. (2019). Defining a new nomenclature for the structures of active and inactive kinases. *Proceedings of the National Academy of Sciences*, *116*(14), 6818–6827. doi: 10.1073/pnas.1814279116

Modi, V., & Dunbrack, R. L. (2021). Kincore: a web resource for structural classification of protein kinases and their inhibitors. *Nucleic Acids Research*, *50*(D1), D654–D664. doi: 10.1093/nar/gkab920

Mora, A., Komander, D., Aalten, D. M. F. van, & Alessi, D. R. (2004). PDK1, the master regulator of AGC kinase signal transduction. *Seminars in Cell & Developmental Biology*, *15*(2), 161–170. doi: 10.1016/j.semcdb.2003.12.022

Newton, A. C. (2018). Protein kinase C: perfectly balanced. *Critical Reviews in Biochemistry and Molecular Biology*, *53*(2), 208–230. doi: 10.1080/10409238.2018.1442408

Nguyen, H. P. M., McGuire, K. L., Cook, B. D., & Jr, M. A. H. (2022). Manual Blot-and-Plunge Freezing of Biological Specimens for Single-Particle Cryogenic Electron Microscopy. *Journal of Visualized Experiments*, (180). doi: 10.3791/62765

Nogales, E. (2016). The development of cryo-EM into a mainstream structural biology technique. *Nature Methods*, *13*(1), 24–27. doi: 10.1038/nmeth.3694

Nogales, E., & Mahamid, J. (2024). Bridging structural and cell biology with cryo-electron microscopy. *Nature*, *628*(8006), 47–56. doi: 10.1038/s41586-024-07198-2

Nolen, B., Taylor, S., & Ghosh, G. (2004). Regulation of Protein Kinases Controlling Activity through Activation Segment Conformation. *Molecular Cell*, *15*(5), 661–675. doi: 10.1016/j.molcel.2004.08.024

Oliver, A. W., Knapp, S., & Pearl, L. H. (2007). Activation segment exchange: a common mechanism of kinase autophosphorylation? *Trends in Biochemical Sciences*, *32*(8), 351–356. doi: 10.1016/j.tibs.2007.06.004

Orr, J. W., & Newton, A. C. (1994). Requirement for negative charge on "activation loop" of protein kinase C. *Journal of Biological Chemistry*, *269*(44), 27715–27718. doi: 10.1016/s0021-9258(18)47044-5

Pak, M. A., Markhieva, K. A., Novikova, M. S., Petrov, D. S., Vorobyev, I. S., Maksimova, E. S., … Ivankov, D. N. (2021). Using AlphaFold to predict the impact of single mutations on protein stability and function. *BioRxiv*, 2021.09.19.460937. doi: 10.1101/2021.09.19.460937

Peacock, R. B., & Komives, E. A. (2021). Hydrogen/Deuterium Exchange and Nuclear Magnetic Resonance Spectroscopy Reveal Dynamic Allostery on Multiple Time Scales in the Serine Protease Thrombin. *Biochemistry*, *60*(46), 3441–3448. doi: 10.1021/acs.biochem.1c00277

Pearce, L. R., Komander, D., & Alessi, D. R. (2010). The nuts and bolts of AGC protein kinases. *Nature Reviews Molecular Cell Biology*, *11*(1), 9–22. doi: 10.1038/nrm2822

Pérez-González, A., Jimenez-Vicente, E., Salinero-Lanzarote, A., Harris, D. F., Seefeldt, L. C., & Dean, D. R. (2022). AnfO controls fidelity of nitrogenase FeFe protein maturation by preventing misincorporation of FeV-cofactor. *Molecular Microbiology*, *117*(5), 1080–1088. doi: 10.1111/mmi.14890

Punjani, A., Rubinstein, J. L., Fleet, D. J., & Brubaker, M. A. (2017). cryoSPARC: algorithms for rapid unsupervised cryo-EM structure determination. *Nature Methods*, *14*(3), 290--296. doi: 10.1038/nmeth.4169

Razinkov, I., Dandey, V. P., Wei, H., Zhang, Z., Melnekoff, D., Rice, W. J., … Carragher, B. (2016). A new method for vitrifying samples for cryoEM. *Journal of Structural Biology*, *195*(2), 190--198. doi: 10.1016/j.jsb.2016.06.001

Rees, D. C., Tezcan, F. A., Haynes, C. A., Walton, M. Y., Andrade, S., Einsle, O., & Howard, J. B. (2005). Structural basis of biological nitrogen fixation. *Philosophical Transactions of the Royal Society A: Mathematical, Physical and Engineering Sciences*, *363*(1829), 971–984. doi: 10.1098/rsta.2004.1539

Rellos, P., Pike, A. C. W., Niesen, F. H., Salah, E., Lee, W. H., Delft, F. von, & Knapp, S. (2010). Structure of the CaMKIIδ/Calmodulin Complex Reveals the Molecular Mechanism of CaMKII Kinase Activation. *PLoS Biology*, *8*(7), e1000426. doi: 10.1371/journal.pbio.1000426

Richards, S. A., Dreisbach, V. C., Murphy, L. O., & Blenis, J. (2001). Characterization of Regulatory Events Associated with Membrane Targeting of p90 Ribosomal S6 Kinase 1. *Molecular and Cellular Biology*, *21*(21), 7470–7480. doi: 10.1128/mcb.21.21.7470-7480.2001

Romeo, Y., Zhang, X., & Roux, P. P. (2011). Regulation and function of the RSK family of protein kinases. *Biochemical Journal*, *441*(2), 553–569. doi: 10.1042/bj20110289

Roskoski, R. (2012). ERK1/2 MAP kinases: Structure, function, and regulation. *Pharmacological Research*, *66*(2), 105–143. doi: 10.1016/j.phrs.2012.04.005

Roskoski, R. (2024). Properties of FDA-approved small molecule protein kinase inhibitors: A 2024 update. *Pharmacological Research*, *200*, 107059. doi: 10.1016/j.phrs.2024.107059

Roux, P. P., Richards, S. A., & Blenis, J. (2003). Phosphorylation of p90 Ribosomal S6 Kinase (RSK) Regulates Extracellular Signal-Regulated Kinase Docking and RSK Activity. *Molecular and Cellular Biology*, *23*(14), 4796–4804. doi: 10.1128/mcb.23.14.4796-4804.2003

Rutledge, H. L., Cook, B. D., Nguyen, H. P. M., HerzikJr., M. A., & Tezcan, F. A. (2022). Structures of the nitrogenase complex prepared under catalytic turnover conditions. *Science*, *377*(6608), 865–869. doi: 10.1126/science.abq7641

Senior, A. W., Evans, R., Jumper, J., Kirkpatrick, J., Sifre, L., Green, T., … Hassabis, D. (2020). Improved protein structure prediction using potentials from deep learning. *Nature*, *577*(7792), 706–710. doi: 10.1038/s41586-019-1923-7

Shang, Y., Shi, H., Liu, M., Lan, P., Li, D., Liu, X., … Chen, S. (2025). Using synthetic biology to express nitrogenase biosynthesis pathway in rice and to overcome barriers of nitrogenase instability in plant cytosol. *Trends in Biotechnology*, *43*(4), 946–968. doi: 10.1016/j.tibtech.2024.12.002

Smil. (2001). Enriching the earth. *Cambridge, MA:MIT Press.*

Sok, P., Gógl, G., Kumar, G. S., Alexa, A., Singh, N., Kirsch, K., … Reményi, A. (2020). MAP Kinase-Mediated Activation of RSK1 and MK2 Substrate Kinases. *Structure*, *28*(10), 1101-1113.e5. doi: 10.1016/j.str.2020.06.007

Spirrison, A. N., & Lannigan, D. A. (2024). RSK1 and RSK2 as therapeutic targets: an up-to-date snapshot of emerging data. *Expert Opinion on Therapeutic Targets*, *28*(12), 1047–1059. doi: 10.1080/14728222.2024.2433123

Steichen, J. M., Kuchinskas, M., Keshwani, M. M., Yang, J., Adams, J. A., & Taylor, S. S. (2012). Structural Basis for the Regulation of Protein Kinase A by Activation Loop Phosphorylation*. *Journal of Biological Chemistry*, *287*(18), 14672–14680. doi: 10.1074/jbc.m111.335091

Takimura, T., Kamata, K., Fukasawa, K., Ohsawa, H., Komatani, H., Yoshizumi, T., … Iwasawa, Y. (2010). Structures of the PKC-ι kinase domain in its ATP-bound and apo forms reveal

defined structures of residues 533–551 in the C-terminal tail and their roles in ATP binding. *Acta Crystallographica Section D: Biological Crystallography*, *66*(5), 577–583. doi: 10.1107/s0907444910005639

Taylor, S. S., Ilouz, R., Zhang, P., & Kornev, A. P. (2012). Assembly of allosteric macromolecular switches: lessons from PKA. *Nature Reviews Molecular Cell Biology*, *13*(10), 646–658. doi: 10.1038/nrm3432

Taylor, S. S., Keshwani, M. M., Steichen, J. M., & Kornev, A. P. (2012). Evolution of the eukaryotic protein kinases as dynamic molecular switches. *Philosophical Transactions of the Royal Society B: Biological Sciences*, *367*(1602), 2517–2528. doi: 10.1098/rstb.2012.0054

Taylor, S. S., & Kornev, A. P. (2011). Protein kinases: evolution of dynamic regulatory proteins. *Trends in Biochemical Sciences*, *36*(2), 65–77. doi: 10.1016/j.tibs.2010.09.006

Taylor, S. S., Shaw, A. S., Kannan, N., & Kornev, A. P. (2015). Integration of signaling in the kinome: Architecture and regulation of the αC Helix. *Biochimica et Biophysica Acta (BBA) - Proteins and Proteomics*, *1854*(10), 1567–1574. doi: 10.1016/j.bbapap.2015.04.007

Taylor, S. S., Søberg, K., Kobori, E., Wu, J., Pautz, S., Herberg, F. W., & Skålhegg, B. S. (2022). The Tails of Protein Kinase A. *Molecular Pharmacology*, *101*(4), 219–225. doi: 10.1124/molpharm.121.000315

Taylor, S. S., Wu, J., Bruystens, J. G. H., Rio, J. C. D., Lu, T.-W., Kornev, A. P., & Eyck, L. F. T. (2021). From structure to the dynamic regulation of a molecular switch: A journey over 3 decades. *Journal of Biological Chemistry*, *296*, 100746. doi: 10.1016/j.jbc.2021.100746

Taylor, S. S., Zhang, P., Steichen, J. M., Keshwani, M. M., & Kornev, A. P. (2013). PKA: Lessons learned after twenty years. *Biochimica et Biophysica Acta (BBA) - Proteins and Proteomics*, *1834*(7), 1271–1278. doi: 10.1016/j.bbapap.2013.03.007

Temmerman, K., Simon, B., & Wilmanns, M. (2013). Structural and functional diversity in the activity and regulation of DAPK-related protein kinases. *The FEBS Journal*, *280*(21), 5533–5550. doi: 10.1111/febs.12384

Tokumitsu, H., & Sakagami, H. (2022). Molecular Mechanisms Underlying Ca2+/Calmodulin-Dependent Protein Kinase Kinase Signal Transduction. *International Journal of Molecular Sciences*, *23*(19), 11025. doi: 10.3390/ijms231911025

Trivier, E., Cesare, D. D., Jacquot, S., Pannetier, S., Zackai, E., Young, I., … Hanauer, A. (1996). Mutations in the kinase Rsk-2 associated with Coffin-Lowry syndrome. *Nature*, *384*(6609), 567–570. doi: 10.1038/384567a0

Tunyasuvunakool, K., Adler, J., Wu, Z., Green, T., Zielinski, M., Žídek, A., … Hassabis, D. (2021). Highly accurate protein structure prediction for the human proteome. *Nature*, *596*(7873), 590–596. doi: 10.1038/s41586-021-03828-1

Understanding Global Change. (2025). Retrieved from https://ugc.berkeley.edu/background-content/nitrogen/

Utepbergenov, D., Derewenda, U., Olekhnovich, N., Szukalska, G., Banerjee, B., Hilinski, M. K., … Derewenda, Z. S. (2012). Insights into the Inhibition of the p90 Ribosomal S6 Kinase (RSK) by the Flavonol Glycoside SL0101 from the 1.5 Å Crystal Structure of the N-Terminal Domain of RSK2 with Bound Inhibitor. *Biochemistry*, *51*(33), 6499–6510. doi: 10.1021/bi300620c

Utepbergenov, D., Hennig, P. M., Derewenda, U., Artamonov, M. V., Somlyo, A. V., & Derewenda, Z. S. (2016). Bacterial Expression, Purification and In Vitro Phosphorylation of Full-Length Ribosomal S6 Kinase 2 (RSK2). *PLoS ONE*, *11*(10), e0164343. doi: 10.1371/journal.pone.0164343

Varadi, M., Anyango, S., Deshpande, M., Nair, S., Natassia, C., Yordanova, G., … Velankar, S. (2021). AlphaFold Protein Structure Database: massively expanding the structural coverage of protein-sequence space with high-accuracy models. *Nucleic Acids Research*, *50*(D1), D439–D444. doi: 10.1093/nar/gkab1061

Vinciauskaite, V., & Masson, G. R. (2023). Fundamentals of HDX-MS. *Essays in Biochemistry*, *67*(2), 301–314. doi: 10.1042/ebc20220111

Visser, M., Papillon, J. P. N., Luzzio, M., LaMarche, M. J., Fan, J., Michael, W., … Cooke, V. G. (2024). Discovery of Darovasertib (NVP-LXS196), a Pan-PKC Inhibitor for the Treatment of Metastatic Uveal Melanoma. *Journal of Medicinal Chemistry*, *67*(2), 1447–1459. doi: 10.1021/acs.jmedchem.3c02002

Voss, J. M., Harder, O. F., Olshin, P. K., Drabbels, M., & Lorenz, U. J. (2021). Rapid melting and revitrification as an approach to microsecond time-resolved cryo-electron microscopy. *Chemical Physics Letters*, *778*, 138812. doi: 10.1016/j.cplett.2021.138812

Wagner, J., Matt, P. von, Sedrani, R., Albert, R., Cooke, N., Ehrhardt, C., … Cottens, S. (2009). Discovery of 3-(1H-Indol-3-yl)-4-[2-(4-methylpiperazin-1-yl)quinazolin-4-yl]pyrrole-2,5-dione (AEB071), a Potent and Selective Inhibitor of Protein Kinase C Isotypes. *Journal of Medicinal Chemistry*, *52*(20), 6193–6196. doi: 10.1021/jm901108b

Walsh, D. A., Perkins, J. P., & Krebs, E. G. (1968). An adenosine 3',5'-monophosphate-dependant protein kinase from rabbit skeletal muscle. *The Journal of Biological Chemistry*, *243*(13), 3763–3765.

Wang, J., Wu, J.-W., & Wang, Z.-X. (2011). Structural Insights into the Autoactivation Mechanism of p21-Activated Protein Kinase. *Structure*, *19*(12), 1752–1761. doi: 10.1016/j.str.2011.10.013

Weng, J.-H., Aoto, P. C., Lorenz, R., Wu, J., Schmidt, S. H., Manschwetus, J. T., … Taylor, S. S. (2022). LRRK2 dynamics analysis identifies allosteric control of the crosstalk between its catalytic domains. *PLoS Biology*, *20*(2), e3001427. doi: 10.1371/journal.pbio.3001427

White, A., Pargellis, C. A., Studts, J. M., Werneburg, B. G., & Farmer, B. T. (2007). Molecular basis of MAPK-activated protein kinase 2:p38 assembly. *Proceedings of the National Academy of Sciences*, *104*(15), 6353–6358. doi: 10.1073/pnas.0701679104

Wright, E. B., & Lannigan, D. A. (2023). Therapeutic targeting of p90 ribosomal S6 kinase. *Frontiers in Cell and Developmental Biology*, *11*, 1297292. doi: 10.3389/fcell.2023.1297292

Wright, P. E., & Dyson, H. J. (2015). Intrinsically disordered proteins in cellular signalling and regulation. *Nature Reviews Molecular Cell Biology*, *16*(1), 18–29. doi: 10.1038/nrm3920

Yamaoka, K., Saharinen, P., Pesu, M., Holt, V. E., Silvennoinen, O., & O'Shea, J. J. (2004). The Janus kinases (Jaks). *Genome Biology*, *5*(12), 253. doi: 10.1186/gb-2004-5-12-253

Yang, Jie, Garrod, S. M., Deal, M. S., Anand, G. S., Woods, V. L., & Taylor, S. (2005). Allosteric Network of cAMP-dependent Protein Kinase Revealed by Mutation of Tyr204 in the P+1 Loop. *Journal of Molecular Biology*, *346*(1), 191–201. doi: 10.1016/j.jmb.2004.11.030

Yang, Jing, Cron, P., Thompson, V., Good, V. M., Hess, D., Hemmings, B. A., & Barford, D. (2002). Molecular Mechanism for the Regulation of Protein Kinase B/Akt by Hydrophobic Motif Phosphorylation. *Molecular Cell*, *9*(6), 1227–1240. doi: 10.1016/s1097-2765(02)00550-6

Zeniou, M., Ding, T., Trivier, E., & Hanauer, A. (2002). Expression analysis of RSK gene family members: the RSK2 gene, mutated in Coffin–Lowry syndrome, is prominently expressed in brain structures essential for cognitive function and learning. *Human Molecular Genetics*, *11*(23), 2929–2940. doi: 10.1093/hmg/11.23.2929

Zhang, F., Strand, A., Robbins, D., Cobb, M. H., & Goldsmith, E. J. (1994). Atomic structure of the MAP kinase ERK2 at 2.3 Å resolution. *Nature*, *367*(6465), 704–711. doi: 10.1038/367704a0

Zhang, P., Smith-Nguyen, E. V., Keshwani, M. M., Deal, M. S., Kornev, A. P., & Taylor, S. S. (2012). Structure and Allostery of the PKA RIIβ Tetrameric Holoenzyme. *Science*, *335*(6069), 712–716. doi: 10.1126/science.1213979

ZHANG, W., & LIU, H. T. (2002). MAPK signal pathways in the regulation of cell proliferation in mammalian cells. *Cell Research*, *12*(1), 9–18. doi: 10.1038/sj.cr.7290105

Zhao, Y., Bjørbæk, C., Weremowicz, S., Morton, C. C., & Moller, D. E. (1995). RSK3 Encodes a Novel pp90 rsk Isoform with a Unique N-Terminal Sequence: Growth Factor-Stimulated Kinase Function and Nuclear Translocation. *Molecular and Cellular Biology*, *15*(8), 4353–4363. doi: 10.1128/mcb.15.8.4353

Zheng, J., Trafny, E. A., Knighton, D. R., Xuong, N., Taylor, S. S., Eyck, L. F. T., & Sowadski, J. M. (1993). 2.2 Å refined crystal structure of the catalytic subunit of cAMP-dependent protein

kinase complexed with MnATP and a peptide inhibitor. *Acta Crystallographica Section D*, *49*(3), 362–365. doi: 10.1107/s0907444993000423

Zhong, B., Su, X., Wen, M., Zuo, S., Hong, L., & Lin, J. (2021). ParaFold: Paralleling AlphaFold for Large-Scale Predictions. *ArXiv*.